UCLA
UCLA Electronic Theses and Dissertations

Title
Applications of Bistable Electroactive Polymers as Rewritable Photonic Paper, Smart Windows and Wearable Pressure Sensors

Permalink
https://escholarship.org/uc/item/7pk4q4kh

Author
Xie, Yu

Publication Date
2019

Peer reviewed|Thesis/dissertation

eScholarship.org Powered by the California Digital Library
University of California

UNIVERSITY OF CALIFORNIA

Los Angeles

Applications of Bistable Electroactive Polymers as Rewritable Photonic Paper, Smart Windows and Wearable Pressure Sensors

A dissertation submitted in partial satisfaction of the

requirements for the degree Doctor of Philosophy in

Materials Science and Engineering

by

Yu Xie

2019

© Copyright by

Yu Xie

2019

ABSTRACT OF THE DISSERTATION

Applications of Bistable Electroactive Polymers as

Rewritable Photonic Paper, Smart Windows and Wearable Pressure Sensors

by

Yu Xie

Doctor of Philosophy in Materials Science and Engineering

University of California, Los Angeles, 2019

Professor Qibing Pei, Chair

The flexibility and insulating nature of polymeric dielectric materials are widely used in robotic and wearable electronic devices like electrical insulation, capacitive sensors, and electromechanical actuators. When combined with a phase transition-induced shape memory property, the resultant bistable electroactive polymer (BSEP) opens up new applications due to the rigid-to-rigid actuation of BSEP tremendously reducing the energy consumption for device operation while providing desirable strength for external loads. This dissertation focuses on investigating insulating, electroactive, and phase transition properties of BSEP, and adapting

each aspect of the properties in the pursuit of innovative devices, such as rewritable photonic paper, smart windows with whole solar spectrum modulation, and wearable pressure sensors.

An ink-free rewritable photonic paper has been invented through the interdisciplinary combination of photonic crystals, shape memory and electroactive properties of BSEP. The rewritable paper consists of a ferroferric oxide-carbon (Fe_3O_4@C) core–shell nanoparticle (NP)-based photonic crystal embedded in a BSEP. The nanocomposite can be repeatedly triggered to change into different shapes and colors due to the z-directional deformation that is induced by an electric field. The actuated shape and color can be maintained for a long term without energy input, and the stored images can then be rewritten over 500 times without noticeable degradation. Low energy consumption and simple erasing/rewriting are features that match the benefits of conventional paper as a zero-energy and long term data storage medium, but provide the additional advantage of rewritability. With pixelated electrode arrays, user-defined information can be actuated and erased at will which has been demonstrated through a seven-segment numerical display.

A smart window with wide-band light modulation is designed solely based on the phase transition property of BSEP. One component of BSEP can be switched between semicrystalline and amorphous states through cooling below or heating above its melting temperature, leading to a reversible opaque-to-transparent transition. The opacity switching property of BSEP was further improved by mixing a more hydrophilic component to induce micro-scale phase separation, which is responsible for the whole solar spectrum light modulation due to Mie scattering. The resultant smart window achieves both high solar transmittance modulation of 70.2% and high luminous transmittance modulation of 80.4% which rivals the best reported smart windows and commercial privacy glasses with the highest privacy levels. This flexible

smart window can also be mounted on curved surfaces for the need of windows with arbitrary shapes. This work is the first one to report an all-solid thermochromic smart window film without the inclusion of any metal/metal oxides or liquid crystals to enable a large light modulation over the whole solar spectrum.

A flexible fiber-based pressure sensor is realized by applying a dielectric layer on the outside of a TEMPO-oxidized bacterial cellulose (TOBC)/silver nanowire (AgNW) conducting fiber. The pressure sensor can detect pressures up to 134 MPa with sensitivity of 101×10^{-4} kPa^{-1} due to its hierarchical structure and high conductivity. The porous structure of TOBC/AgNW helps increase the thickness deformation of the sensor with applied pressure, improving the sensing ability. Small pressures of human pulse and voice vibration can be detected with this sensitive pressure sensor. A machine learning classification model was implemented to recognize human's speech where the prediction accuracy on a test dataset is > 90%. The ultrathin fibrous sensor (53 μm) is capable of high-resolution detection, and suitable as a comfortable and fashionable thread substitute for real wearable devices.

The combined properties of BSEP with the proof-of-concept developments of rewritable paper, smart windows and wearable sensors demonstrate its potential for real-world applications. And an outlook for future research and suggested improvements for commercialization are discussed in the conclusion.

The dissertation of Yu Xie is approved.

Yong Chen

Ali Mosleh

Dwight Christopher Streit

Qibing Pei, Committee Chair

University of California, Los Angeles

2019

Dedicated to

my beloved husband, parents and parents-in-law

for their eternal love and support

Contents

List of Figures……x

List of Tables……....xix

Acknowledgements……..xx

Vita……..xxii

1. Introduction……1

1.1. Introduction to Polymeric Dielectric Materials……...1

1.2. Applications of Polymeric Dielectric Materials……..6

1.2.1 Dielectric Elastomers……..6

1.2.1.1 Materials Selection……7

1.2.1.2 Applications for Dielectric Elastomers……..….9

1.2.1.2.1 Soft Robotics……..….10

1.2.1.2.2 Energy Harvesting Generators……12

1.2.2 Capacitive Sensors……14

1.3 Bistable Electroactive Polymer……..17

1.4 Scope and Layout of the Dissertation……19

1.5 Reference……22

2. Bistable and Reconfigurable Photonic Crystals – Electroactive Shape Memory Polymer Nanocomposite for Ink-free Rewritable Paper……..30

2.1 Introduction……30

2.2 Experimental……..34

2.2.1 Materials……34

2.2.2 Synthesis of Fe_3O_4@C Core-Shell Nanoparticles……..34

2.2.3 Fabrication of Fe_3O_4@C-BSEP Photonic Precursors……35

2.2.4 Preparation of Patterned AgNWs Electrodes……35
2.2.5 Fabrication of Fe_3O_4@C-BSEP Rewritable Photonic Films with Patterned Electrodes……...36
2.2.6 Characterization……36
2.2.7 Calculation of Effective Refractive Index of Fe_3O_4@C-BSEP Nanocomposites….37
2.2.8 Calculation of Stopbands of Fe_3O_4@C-BSEP with Different NPs Concentrations..39
2.3 Results and Discussion……...40
2.3.1 Preparation of Fe_3O_4@C Core-Shell Nanoparticle BSEP Nanocomposite……40
2.3.2 Nanoparticle Concentration Effect on Film Initial Color……...43
2.3.3 Mechanical Properties Characterization……47
2.3.4 Shape Memory Property Characterization and Color Change……..51
2.3.5 Electroactive Properties Characterization……55
2.3.6 Bistable Electroactive Photonic Paper……...63
2.4 Conclusion……..65
2.5 Reference……65
3. A Phase-Changing Polymer Film for Broadband Smart Windows Applications……70
3.1 Introduction……70
3.2 Experimental……..74
3.2.1 Materials……74
3.2.2 Fabrication of Smart Window (SW) films……74
3.2.3 Fabrication of AgNW/PUA Composite Heaters……75
3.2.4 Fabrication of Smart Window Devices……..75
3.2.5 Characterization……76
3.3 Results and Discussion……...76
3.3.1 Preparation and Characterization of Smart Window Film……76
3.3.2 Fabrication and Characterization of AgNW Transparent Heater……..85
3.3.3 Smart Window Demonstration……..90
3.4 Conclusion……..93
3.5 Reference……94
4. Hierarchical Bacterial Cellulose-Silver Nanowire Composite Fiber-Based Wearable Pressure Sensors……...…98

4.1 Introduction……98
4.2 Experimental……101
4.2.1 Materials……..101
4.2.2 Preparation of TEMPO-Oxidized Bacterial Cellulose……101
4.2.3 Preparation of TOBC-AgNW Spinning Dope……101
4.2.4 Wet-Spinning of TOBC/AgNW Fibers……...102
4.2.5 Assembly of TOBC/AgNW/PDMS Sensors……...102
4.2.6 Characterization……..103
4.2.7 Machine Learning Classification Model for Phonation Recognition……..103
4.2.7.1 Data Collection……...103
4.2.7.2 Data Pre-processing……104
4.2.7.3 Baseline……..104
4.2.7.4 Classification……..106
4.3 Results and Discussion……109
4.3.1 Preparation and Characterization of TOBC/AgNW Conductive Fibers……109
4.3.2 Preparation and Evaluation of TOBC/AgNW/PDMS Fiber-Based Capacitive Pressure Sensor……114
4.3.3 Applications for Wearable TOBC/AgNW/PDMS Fiber-Based Capacitive Pressure Sensor……...122
4.4 Conclusion……127
4.5 Reference……..127
5. Conclusion and Future Work……130

List of Figures

Figure 1-1. Nonplanar electronics with wrinkle/wavy structures. (a) Fabrication scheme of stretchable ultrathin electronics. Out-of-plane wrinkles were created by laminating devices on a pre-stretched elastomer (3M VHB) and followed by relaxation. **(b)** Sequential formation of wrinkles on a transistor. Scale bar is 1 mm. **(c)** SEM images of stretchable CMOS inverters. **(d)** Optical images of the CMOS inverters under stretching tests in the x and y directions. **(e)** Finite element modelling simulation before (35% pre-strain) and after (70% applied strain) stretching. **(f)** Left: Arrays of inverters on a 0.2mm PDMS substrate. Middle: Optical image of unstretched inverters (90% pre-stretch). Right: Optical image of inverters with 140% tensile strain. **(g)** Left: transfer characteristics and gain for a stretched inverter. Right: Gain and voltage at a maximum gain as a function of stretching cycles. Adapted and reproduced with permission from Ref. 49. Copyright 2008, The National Academy of Sciences of the USA.

Figure 1-2. Illustration of stretchable TFT with rigid island structures. Upper left: whole matrix. Upper right: One TFT on a rigid island with elastic conductor wiring. Lower: One TFT on the PDMS substrate with stretchability gradient. Adapted and reproduced with permission from Ref. 52. Copyright 2015, Macmillan Publisher Limited.

Figure 1-3. **Operating mechanism of dielectric elastomer.** With the application of electric field, the elastomer expands in area and reduces in thickness.

Figure 1-4. Soft robotics enabled by dielectric elastomers. (a) Top: an inchworm robot that was actuated at 10 Hz. Bottom: A crawling robot that was actuated at 1.5 Hz. **(b)** Forwarding locomotion of a hexapod robot that was actuated at 2 Hz. **(c)** Underwater swimming robotic fish. T is the time required for one full flapping cycle. **(d)** Flapping wings that were actuated at 5 Hz. **(e)** Pseudo-eyeballs movement that was actuated to mimic ocular muscle movement. **(f)** Left:

Elastomeric gripper with vertical fibers. Middle: Elastomeric gripper with horizontal wrap action. Right: A combination of two actuators with orthogonal bending directions. Adapted and reproduced with permission from Ref. 38. Copyright 2017, IEEE; Ref. 76. Copyright 2017, Elsevier B.V.; Ref. 77. Copyright 2017, American Association for the Advancement of Science; Ref. 36. Copyright 2015, Springer; Ref. 78. Copyright 2008, SPIE; Ref. 79. Copyright 2015, WILEY-VCH.

Figure 1-5. Demonstrations of energy harvesting generators. (a) Left: Capacitance change with 100% tensile strain for 10 cycles. Right: Energy-harvesting density as a function of nominal applied electric field (strain: 50%, strain rate: 100% s^{-1}). **(b)** Structure of a multilayer triboelectric nanogenerator. **(c)** Top: Demonstration of self-powered shoes that are based on multilayer triboelectric generators with the function of pedometer and fitness track enabled. Bottom: The voltages of energy storage unit while the nanogenerators were driving the pedometer and the fitness tracker. **(d)** 20 LEDs were powered by tapping on a triboelectric nanogenerator when the generator was (left) relaxed and (middle) stretched. Right: An LCD screen was driven by a transparent nanogenerator with finger pressing. Adapted and reproduced with permission from Ref. 41. Copyright 2013, WILEY-VCH; Ref. 42. Copyright 2017, WILEY-VCH; Ref. 15. Copyright 2017, American Association for the Advancement of Science.

Figure 1-6. **Illustration of parallel-plate capacitor.** A is the area of the electrode and d is the average thickness of the dielectric film.

Figure 1-7. Structure and performance of capacitive pressure sensors. (a) Left: Cross-sectional SEM image of the sensor. Right: Enlarged SEM image showing microporous dielectric layer. **(b)** Left: Sandwiched structure of the capacitive sensor with patterned bottom electrode. Right: Real-time capacitance change of a flexible pressure sensor with three times of pronunciation of "Apple". Adapted and reproduced with permission from Ref. 87. Copyright 2017, WILEY-VCH; Ref. 34. Copyright 2017, American Chemical Society.

Figure 1-8. Schematic illustration of actuation mechanism of BSEP. The rigid nanocomposite (a) softens upon heating above its phase-changing temperature (b), applied electric field actuates the softened polymer (c), film returns to rigid state when cooled below the

phase-change temperature, locking the large applied strain (d), and the film recovers its original rigid shape (a) by heating above the phase-changing temperature and then cooling back down.

Figure 1-9. A six-dot Braille character display. (a) All six dots were at ON state. **(b)** Side view of OFF state. **(c)** Side view of ON state. **(d)** Braille character (ON state) was touched by a human finger. Adapted and reproduced with permission from Ref. 92. Copyright 2012, SPIE.

Figure 2-1. **Schematics demonstrating the electroactive and the shape memory properties of a Fe_3O_4@C-BSEP photonic nanocomposite and its writing/erasing mechanism. (a)** The rigid nanocomposite (I) softens upon heating above its phase-changing temperature (II), applied electric field actuates the softened polymer (III), film returns to rigid state when cooled below the phase-change temperature, locking the large applied strain (IV), and the film recovers its original rigid shape (I) by heating above the phase-changing temperature and then cooling back down. **(b)** Enlarged cross sections of the photonic nanocomposite showing the interparticle distance changing during electric field actuation. **(c)** Cross-sectional SEM image of nanochain structures of Fe_3O_4@C nanoparticles in a cured BSEP substrate. The scale bar is 5 μm in length.

Figure 2-2. TEM images of Fe_3O_4@C core-shell nanoparticles with diameters of **(a)** 120nm, **(b)** 140nm and **(c)** 160nm. The scale bars are 150 nm in length.

Figure 2-3. (**a**) Chemical structures of each components of BSEP. (**b**) Schematic illustration of crosslined BSEP network.

Figure 2-4. **(a)** Magnetization curve of Fe_3O_4@C nanoparticles powder at room temperature.

Figure 2-5. **BSEP-Fe_3O_4@C photonic nanocomposite films with increasing nanoparticle concentrations. (a)** Optical images of the photonic nanocomposites showing red shift in base reflected color. **(b)** Cross-sectional SEM images of the Fe_3O_4@C nanochains in the BSEP matrix. Interparticle distance increased with increasnig Fe_3O_4@C weight fraction. All the scale bars are 500 nm in length. **(c)** Reflective spectra at each concentration. **(d)** Peak wavelength of the stopbands as a function of the concentration of nanoparticles. Black circles are calculated values based on Bragg's diffraction equation using the NP-NP distances meansured by SEM. Calculation details can be found in section 2.2.6 and 2.2.7. Red square values were directly meansured by the reflective photospectrometer.

Figure 2-6. **Fe_3O_4@C-PEG nanocomposites with increasing nanoparticle concentrations.** (**a**) Optical images of the nanocomposites showing red shift in reflection color. (**b**) Cross-sectional SEM images showing Fe_3O_4@C nanochains in the PEG matrix. Interparticles distance is increased with Fe_3O_4@C weight fraction. The scale bars are 500 nm in length.

Figure 2-7. **Mechanical properties of a 7 wt% BSEP-Fe_3O_4@C photonic nanocomposite compared to pure BSEP**. **(a)** Storage modulus (E') as a function of temperature showing a glass transition temperature of ~38 ºC for both 7 wt% nanocomposite and pure BSEP. **(b)** Loss factor of both 7 wt% nanocomposite and pure BSEP as a function of temperature. **(c)** Tensile stress-strain curves. Frature strain is 125% for the 7 wt% nanocomposite and 286% for the pure BSEP. **(d)** A tensile loading-unloading cycle for the pure BSEP polymer and 7 wt% nanocomposites. **(e)** Shape memory cycle test for pure BSEP polymer. **(f)** Shape memory cycle test for 7 wt% nanocomposite.

Fig 2-8. **Shape memory property of the photonic nanocomposite containing 6 wt% Fe_3O_4@C nanoparticles. (a)** Optical images of the a red photonic nanocomposite at 0%, 50%, and 100% tensile strains. Note that all of the films are free-standing and rigid at room temperature. The rightmost image is the recovered shape of the the nanocomposite film after 100% strain. **(b)** Cross-sectional SEM images of the same photonic nanocomposite at 0%, 50% and 100% tensile strains. Interparticle distance decreases with increasing film strain. All the scale bars are 500 nm in length. Reflective spectra **(c)** and peak reflective wavelengths **(d)** of this photonic nanocomposite as a function of tensile strain. "0% recover" data points in both figures indicate the complete recovery of the photonic film after 100% strain. **(e)** Peak reflective wavelengths of a 100% strained photonic nanocomposite measured over an eight-month span.

Figure 2-9. **SEM images of Fe_3O_4@C chains within BSEPs with different tensile strain levels.** Fe_3O_4@C interparticle distances are shown in **Table 2-2**. The scale bars are 500 nm in length.

Figure 2-10. A schematic illustration for the fabrication process of Fe_3O_4@C-BSEP nanocomposite pixel sample with patterned AgNWs electrodes.

Figure 2-11. Sheet resistance of a AgNW-BSEP composite electrode (active area 5 mm x 5 mm) with increasing **(a)** uni-axial tensile strain, and **(b)** bi-axial area strain. The **inset in (b)** enlarges

the sheet resistance change from 0%-45% area strain, as indicated by the red dashed square. **(c)** Transient resistances measured during 10 cycles of sequentially stretching–relaxing for a 15 Ω sq^{-1} AgNW–BSEP composite electrode between 0% and 10%, 0% and 20%, 0% and 30%, 0% and 40%, 0% and 50% strains (sample size: 5×5 mm^2; stretch speed: 1 mm s^{-1}, sample was at 45 ºC when measured).

Figure 2-12. **(a)**, **(b)** TEM images of a AgNW-BSEP composite electrode with no strain and 50% area strain. Red arrows indicate the areas where AgNWs broke.

Fig 2-13. Electrical actuation of the photonic nanocomposite pixel above transition temperature. (a) Reflective spectra with incremental increase in applied electric field. **(b)** Peak reflective wavelengths as a function of electric field. Red open circles are stopbands calculated from thickness strains of the film, which are shown next to the circles. Calculation procedure can be found in **Table 2-3**. **(c)** Reversible writing and erasing of a red photonic nanocomposite pixel by switching the 22.5 kV m^{-1} electrical field on and off. **(d)** Peak reflective wavelength across 500 writing and erasing cycles following a square wave signal operating between 0 and 22.5 kV m^{-1}. **(e), (f)** Written and erased states of photonic nanocomposite pixels switching between **(e)** red and green colors, and **(f)** green and purple colors under electric field actuation. The color-changing area is the "active area" where the AgNW electrodes on top and bottom surfaces overlap. The scale bars are 3mm in length.

Fig 2-14. **Demonstration of rewritable photonic papers. (a)** Selected images of a photonic paper sequentially demonstrating digits 0-9. **(b)** Writing and erasing a "UCLA" pattern with font size of 10 on a photonic paper. The scale bars are all 3mm in length.

Figure 3-1. Comparison between neat SA and SW films. (a) Differential scanning calorimetry results showing a shift of melting temperature of SW film to lower degree. **(b)** X-Ray Diffraction results for both SA and SW films. **(c)** Contact angles of both neat SA film and neat ETPTA film. **(d)** SEM images of neat SA film and SW film. As-prepared (i) neat SA film and (iii) SW film, (ii) neat SA film and (iv) SW film after one cycle of heating above T_m and then cooled to below Tm. The film surface in image iv was tilted with 45° to give a better view of the patterns. All scale bars represent 10 μm. **(e)** Refractive indices of both pure ETPTA film and neat SA film as a function of temperature.

Figure 3-2. Transmittance spectrum of both neat SA and SW films. (a) Parallel transmittance spectrum for both pure SA and SW films. **(b)** Diffusive transmittance spectrum for both films. Dotted lines show transmittance of both films at transparent status. Solid lines represent transmittance of both films at opaque status. The blue shaded areas represent visible light range from 400 nm to 800 nm. **(c)** Solar, luminous and IR transmittance comparison between SW and neat SA films. **(d)** Transmittance modulation performance (Luminous Transmittance, T_{lum}, at transparent state) for some of the best reported thermochromic smart windows: hydrogel films, VO_2 based films, liquid crystals hybrid films. Adapted and reproduced with permission from Ref. 4. Copyright 2019, Elsevier Inc.; Ref. 15. Copyright 2018, WILEY-VCH; Ref. 19. Copyright 2017, American Chemical Society; Ref. 31. Copyright 2015, The Royal Society of Chemistry; Ref. 32. Copyright 2014, The Royal Society of Chemistry; Ref. 33. Copyright 2014, The Royal Society of Chemistry; Ref. 34. Copyright 2013, the Owner Societies; Ref. 35. Copyright 2017, The Royal Society of Chemistry and the Centre National de la Recherche Scientifique; Ref. 36. Copyright 2014, The Royal Society of Chemistry; Ref. 37. Copyright 2017, Elsevier B.V; Ref. 38. Copyright 2016, American Chemical Society.

Figure 3-3. Microscope images of SW films during one switching cycle. Initial opaque status **(a)** showing a rough surface patterns induced by phase separation. After being heated up, the transparent film **(b)** demonstrates a smoother surface. When being cooled down again, the surface patterns **(c)** restored.

Figure 3-4. A schematic illustration for the fabrication process of AgNW/PUA composite heater.

Figure 3-5. Storage modulus versus temperature for AgNW/PUA composite heater.

Figure 3-6. Performances of AgNW/PUA composite heaters. (a) Transmittance spectrum of AgNW/PUA composite heaters with different sheet resistance. **(b)** Resistance change with sticking cycles. **(c)** Resistance change with bending-unbending experiments. **(d)** Setup for bending-unbending experiments.

Figure 3-7. Heating performance of AgNW/PUA composite heaters. (a) Long term joule heating properties. **(b)** Cyclic joule heating tests with applied square wave voltages. **(c)** Time-dependent temperature change with increased external voltages. **(d)** IR images at different applied voltages showing temperature distributions of AgNW/PUA composite heaters. **(e)**

Saturation temperatures at various power densities. The power efficiency is indicated by the slope. **(f)** Heater saturation temperature as a function of external voltage.

Figure 3-8. Schematic illustration of the device structure for a smart window design.

Figure 3-9. Demonstration of all-solid smart windows. (a) One switching cycle of a flat smart window. Underneath "UCLA" patterns can show up or hide upon the switching on/off of this smart window. The red dotted square frame indicates the location of AgNW/PUA composite heater. **(b)** One switching cycle of a curved smart window that is mounted on a round vial. **(c)** Switching speed of smart windows. **(d)** and **(e)** are parallel and diffusive transmittance spectra of cyclic switching of a flat smart window for over 500 cycles.

Figure 3-10. Demonstration of all-solid smart windows. (a) and **(b)** opaque and transparent statuses of a flat smart window that was mounted on a real glass window.

Figure 4-1. Grid search results of baseline random forest model for dataset without feature extractions.

Figure 4-2. Grid search results of random forest model for dataset with feature extractions.

Figure 4-3. TEM images of **(a)** TOBC nanofibers and **(b)** Ag nanowires.

Figure 4-4. Cross-sectional and surficial SEM images and the corresponding EDS mapping images of TOBC/AgNW fiber. (a)(d) Cross-sectional and surficial SEM images. EDS mappings showing the spatial distribution of Ag element on the **(b)** cross-section and **(e)** surface of TOBC/AgNW fiber. Ca element mapping on the **(b)** cross-section and **(e)** surface of TOBC/AgNW fiber.

Figure 4-5. SEM images of TOBC/AgNW fiber. (a)(b) Cross-sectional SEM images of TOBC/AgNW fiber. TOBC/AgNW fiber has a loose and porous structure. **(c)(d)** Surficial SEM images of TOBC/AgNW fiber.

Figure 4-6. Optical microscope image of crosslinked TOBC/AgNW fiber.

Figure 4-7. Mechanical property of TOBC/AgNW fiber. (a) Tensile stress-strain curves for crosslinked and non-crosslinked fibers. **(b**) A thin needle is threaded by a long flexible

TOBC/AgNW fiber and impales cloth. The length of stitches is 3 mm. **(c)** Knitted flexible TOBC/AgNW fiber into a circle with a diameter of less than 2 mm.

Figure 4-8. Electrical property of TOBC/AgNW fiber. (a) Conductivity change with bending-unbending cycles. **(b)** Setup for bending-unbending experiment. Bending radius is 1.5 mm. **(c)** Two TOBC/AgNW fibers lighting a LED bulb with a voltage of 2 V.

Figure 4-9. SEM images of TOBC/AgNW/PDMS fiber. (a) Cross-sectional image. **(b)** Surficial image. PDMS covers the TOBC/AgNW fiber leading to a smooth surface.

Figure 4-10. FTIR spectrum for pure PDMS, TOBC/AgNW fiber and TOBC/AgNW/PDMS fiber.

Figure 4-11. Schematic illustration of TOBC/AgNW/PDMS fiber-based sensor and its working mechanism.

Figure 4-12. Sensing performance of TOBC/AgNW/PDMS sensors. (a) Capacitive response of the pressure sensor in five cycles for the different applied loads of 0.05 N, 0.1 N, and 0.5 N. **(b)** Relative capacitance changes with respect to progressively increasing pressures. **(c)** Relative capacitance changes at low pressure range showing a sensitivity of 101×10^{-1} kPa^{-1}. **(d)** Hysteresis characteristics of the pressure sensor in response to different levels of pressure. **(e)** Response time of the TOBC/AgNW/PDMS sensor. **(f)** Stability of the pressure sensor over 500 cycles of a repeated loading-unloading test.

Figure 4-13. Capacitive response performance comparison between TOBC/AgNW/PDMS sensor and Steel/PDMS sensor.

Figure 4-14. Sensing performance of TOBC/AgNW/PDMS sensors. (a) Capacitive response of dynamic bending signals. **(b)** Capacitive response of placing and removal of a human finger. **(c)** Pixelated pressure sensor array to detect the spatial distribution of pressures applied by two different weights. **(d)** 3D histogram of the weights placed on the sensor array.

Figure 4-15. Wrist pulse measurements with TOBC/AgNW/PDMS sensor. (a) Capacitive responses of the sensor on a human wrist. **(b)** A typical wrist pulse waveform, indicating percussion (P) wave, tidal (T) wave and diastolic (D) wave.

Figure 4-16. Human phonation measurements with TOBC/AgNW/PDMS sensor. (a) The pressure sensor setup on a fashionable choker. **(b)** Capacitance variation of the flexible pressure sensor in response to the pronunciation of "melody". **(c)** Capacitance variation in response to the pronunciation of a line of a Chinese poem.

Figure 4-17. Voice detection of digit 1-10 with the TOBC/AgNW/PDMS sensor.

List of Tables

Table 2-1. Interparticle distances (D determined from SEM images), refractive index (n), calculated peak wavelengths of stopbands (λ) and measured reflective wavelengths (λ, by reflective spectrum) for Fe_3O_4@C-BSEP nanocomposites with different nanoparticle concentrations (C).

Table 2-2. Theoretical (ε_Z^*) and actual (ε_Z) thickness strains, theoretical (D*) and measured (D) Fe_3O_4@C interparticle distances, calculated (λ*) and measured (λ) reflective wavelengths of Fe_3O_4@C-BSEP nanocomposites with different tensile strains (ε).

Table 2-3. Calculated strains along x-direction (ε_x) and thickness direction (ε_z), calculated (λ*) and measured (λ) reflective wavelength of Fe_3O_4@C-BSEP nanocomposites with different electric field E.

Acknowledgements

First and foremost, I would like to thank my advisor, Professor Qibing Pei, from the bottom of my heart for his continuous support, encouragement and mentorship. This dissertation would not be possible without his professional guidance.

I would also like to express the appreciation towards my committee members, Professor Yong Chen, Professor Dwight Streit, Professor Ali Mosleh and Professor Christopher Lynch for their supports during my five years at UCLA.

Furthermore, I am truly grateful to all current and past members of the Soft Materials Laboratory Research Group who have helped me with their selfless advices and assistance. I would like to specifically thank Dr. Wenxin Wang for flourishing the scientific ideas in Chapter 2 and helping me build confidence in the early stage of my Ph.D. study; thank Fangyi Guan for the enjoyable collaboration for the projects in Chapter 3 and 4; thank Zhou li for synthesizing and characterizing nanoparticles that were initially needed in Chapter 3; thank Dr. Yunfei Li and Dr. Xiaofeng Liu for the support not only on research, but also on everything in life; thank Dr. Yuan Meng, Dr. Rujun Ma, Hexing Yin, Zhixin Xie, Elric Zhang, Dr. Charlotte Chou, Dr. Fangchao Zhao, Dr. Huibin Sun, Dr. Dustin Chen, Yilong Huang, Yayun Liu, Dr. Hanhui Liu, Dr. Huier Gao, Ziyang Zhang and Zihang Peng for sharing their valuable experience and discussing scientific ideas with me.

From other research facilities, I would like to thank Dr. Ignacio Martini from UCLA Molecular Instrumentation Center, Dr. Adam Steig and Dr. Ivo Atanasov from CNSI, Dr. Chunni Zhu from UCLA Brain Research Institute and Noah Bodzin from Materials Science department for helping and training on various testing instruments used through the course of my Ph.D. career. I especially want to thank Andrew Siordia, Ryan DeBlock, Dr. Qiulong Wei, and Professor Bruce Dunn from Materials Science department who let me borrow autoclave bombs and ovens, which are essential for the work in Chapter 2.

Moreover, I want to articulate my deepest gratitude to my family. I would like to thank my mother and father for their unconditional love and help, it is their love that motivates me to keep fighting for my dream. I would also like to thank my parents-in-law, brothers-in-law, sisters-in-law and their kids who welcome me with whole hearts and provide me with a second home. Most importantly, I want to thank my loving husband who supports my every dream, no matter big or small, easy or hard. He fights together with me as my best friend, the most reliable ally, the most hardheaded mentor and the most thoughtful husband to make the impossible possible.

Finally, I want to thank the chopped broccoli packages provided by Trader Joe's which afford important dietary fibers and vitamins to me and serve as fuels to help me stay healthy and keep moving through my Ph.D. years.

Vita

2014	B.S. Materials Science and Engineering
	Peking University, Beijing China
2016	M.S. Materials Science and Engineering
	University of California, Los Angeles
2016-2019	Ph.D. Candidate, Materials Science and Engineering
	University of California, Los Angeles
2018	Intern, Semiconductor Products Group
	Applied Materials, Inc., Santa Clara, CA

Publications

[1] **Xie Y**, Meng Y, Wang W, et al. Bistable and Reconfigurable Photonic Crystals—Electroactive Shape Memory Polymer Nanocomposite for Ink‐Free Rewritable Paper[J]. Advanced Functional Materials, 2018, 28(34): 1802430.

[2] **Xie Y**, Guan F, Li Z, et al. A Facile Fabrication of All Solid Phase-Transition Polymer Film for Broadband Smart Windows Applications, submitted for publication (2019)

[3] Guan F, **Xie Y**, Pei Q. Hierarchical AgNW/TOBC Fiber-Based Wearable Pressure Sensors, in preparation (2019)

[4] Hou J, **Xie Y**, Ji A, et al. Carbon-Nanotube-Wrapped Spider Silks for Directed Cardiomyocyte Growth and Electrophysiological Detection[J]. ACS applied materials & interfaces, 2018, 10(8): 6793-6798.

[5] Ma R, Chou S Y, **Xie Y**, et al. Morphological/nanostructural control toward intrinsically stretchable organic electronics[J]. Chemical Society Reviews, 2019.

[6] Li Y F, Chou S Y, Huang P, **Xie Y**, et al. Stretchable Organometal‐Halide‐Perovskite Quantum‐Dot Light‐Emitting Diodes[J]. Advanced Materials, 2019: 1807516.

Fellowship

Dissertation Year Fellowship for 2018-2019, UCLA

Graduate Division University Fellowship for 2017-2018, UCLA

Chapter 1

Introduction

1.1 Introduction to Polymeric Dielectric Materials

In recent years, stretchable electronics that preserve designed electrical properties under repeated tensile strain have attracted much attention, with a wide range of prospective applications, such as stretchable optoelectronic devices,[1-6] artificial muscles,[7-8] stretchable transistors,[9-13] electronic skin,[14-16] soft and humanoid robots,[17-19] stretchable energy harvesters,[20-23] and stretchable sensors.[24-27] Many of these are related to or work with human motions, which experience tensile strains up to 55%.[28-29] To meet this requirement, all components for the electronics need to be stretchable to prevent the limitation of the device performance that is capped by the undesired breaking of brittle materials. Dielectric materials, as the building blocks of complicated electronics, are as crucial as semiconducting and conducting materials to determine the devices' performances.

Dielectric materials typically take parts in capacitors and transistors due to their insulating nature, or exhibit their electromechanical transducing properties in dielectric

elastomers (DE).[30-32] Their charge-accumulating property opens up a wide range of applications, such as sensors[33-35], soft robotics,[36-38], energy harvesting generators[15, 18, 39-42], refreshable braille displays,[43-44] and tunable lenses.[45] To gain stretchable high-performance implementations with minimum external energy consumption, high dielectric constant with good stretchability is usually required for dielectric materials. Traditional inorganic dielectrics, like SiO_2 and Al_2O_3, display high permittivity but lack stretchability. There are two common approaches used to impart mechanical compliance and robustness to inorganic dielectric materials. The first approach involves geometrically patterning the brittle inorganics into wrinkled or wavy structures,[13, 46-47] and the second combines rigid transistor islands with a stretchable substrate.[48]

For the wrinkled configurations, the dielectrics are stretched from the buckled state to a flat surface before inducing strain along the material bonds themselves. Kaltenbrunner et al. utilized potentiostatic anodization to form an ultra-dense aluminium oxide with a high dielectric constant.[13] The several nanometers thick Al_2O_3 was directly fabricated on top of a thin (1 mm) polymer foil, which was then laminated on a pre-stretched elastomeric film (**Figure 1-1(a)(b)**). Buckling structures formed in the active transistor layers after allowing the elastomeric substrate to relax. The wrinkles could accommodate up to 230% strain on the transistors. The transistor can withstand repeated bending of 5 mm radius or less. Kim et al. introduced non-planar and serpentine interconnect designs to achieve a truly "rubber band-like" stretchability with large, double curvature.[49] They used a 50 nm thick layer of SiO_2 as the gate dielectric fabricated by plasma-enhanced chemical vapor deposition. To achieve the non-planar mesh structure, a pre-made mesh with active device islands and serpentine bridges was transferred to a pre-strained PDMS substrate which could form strong bonds with islands. The bridges then lift upon

releasing the pre-strain on PDMS substrate. As shown in **Figure 1-1(c)-(g)**, both the height of the bridges and serpentine structure help to compensate for large strains. And the strain in the active silicon layer within the island was as small as 0.15%, according to their finite-element modelling.

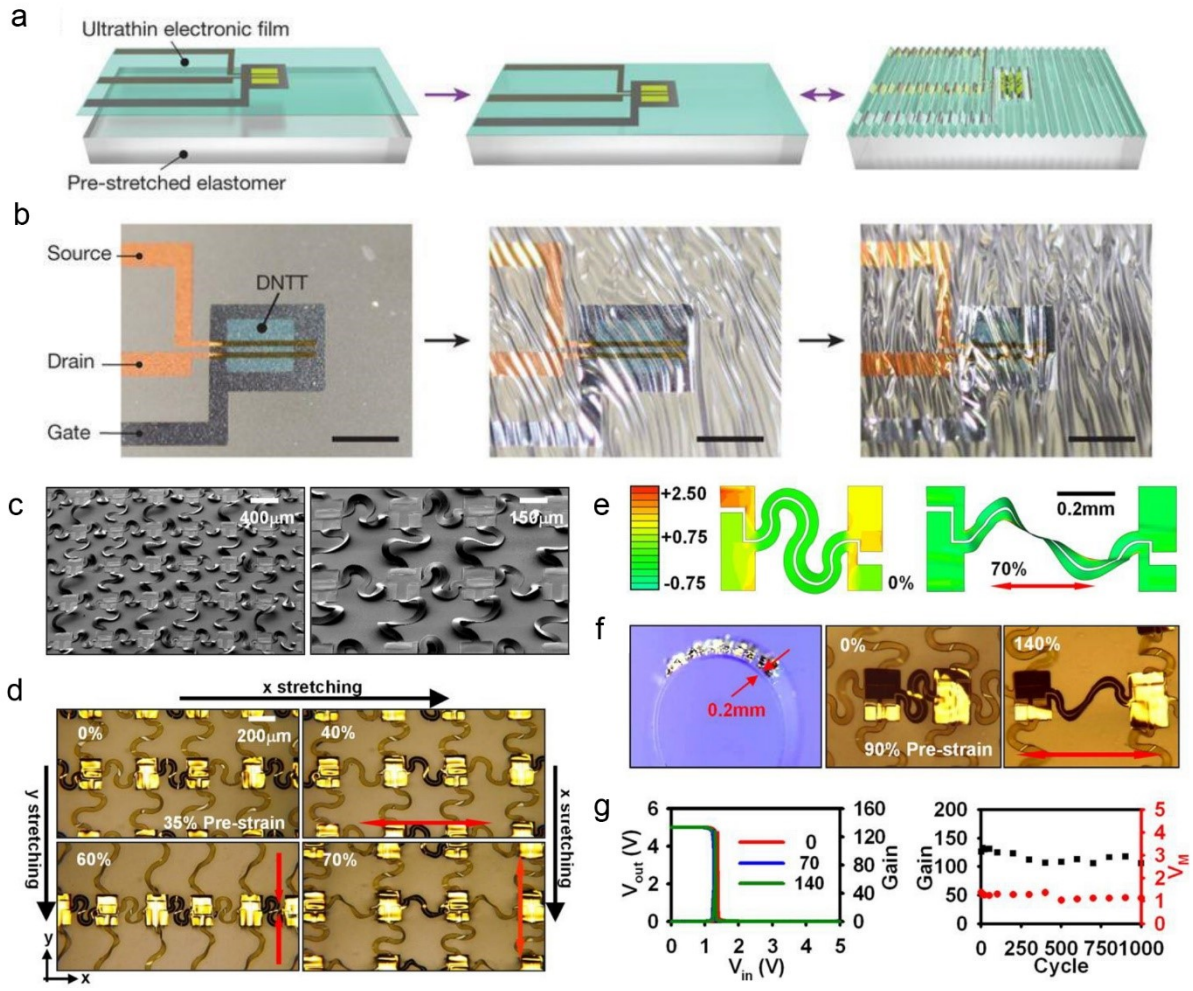

Figure 1-1. Nonplanar electronics with wrinkle/wavy structures. (a) Fabrication scheme of stretchable ultrathin electronics. Out-of-plane wrinkles were created by laminating devices on a pre-stretched elastomer (3M VHB) and followed by relaxation. **(b)** Sequential formation of wrinkles on a transistor. Scale bar is 1 mm. **(c)** SEM images of stretchable CMOS inverters. **(d)** Optical images of the CMOS inverters under stretching tests in the x and y directions. **(e)** Finite element modelling simulation before

(35% pre-strain) and after (70% applied strain) stretching. **(f)** Left: Arrays of inverters on a 0.2mm PDMS substrate. Middle: Optical image of unstretched inverters (90% pre-stretch). Right: Optical image of inverters with 140% tensile strain. **(g)** Left: transfer characteristics and gain for a stretched inverter. Right: Gain and voltage at a maximum gain as a function of stretching cycles. Adapted and reproduced with permission from Ref. 49. Copyright 2008, The National Academy of Sciences of the USA.

For the rigid island structures, the high strains are accommodated by elongation in the soft substrate rather than the rigid components themselves. In Matsuhisa et al.'s work, 12 x 12 and 2 x 2 transistor active matrices with 19 nm thick aluminum oxide as dielectric layers were fabricated using polydimethylsiloxane (PDMS) substrates with stretchability-gradient.[50-52] Devices were located on top of the rigid island regions where PDMS has a higher modulus. The Young's modulus and thickness of the PDMS layer gradually reduced in a circle fashion from the rigid island, resulting in a softer and more stretchable PDMS region that connected adjacent rigid islands as shown in **Figure 1-2**.

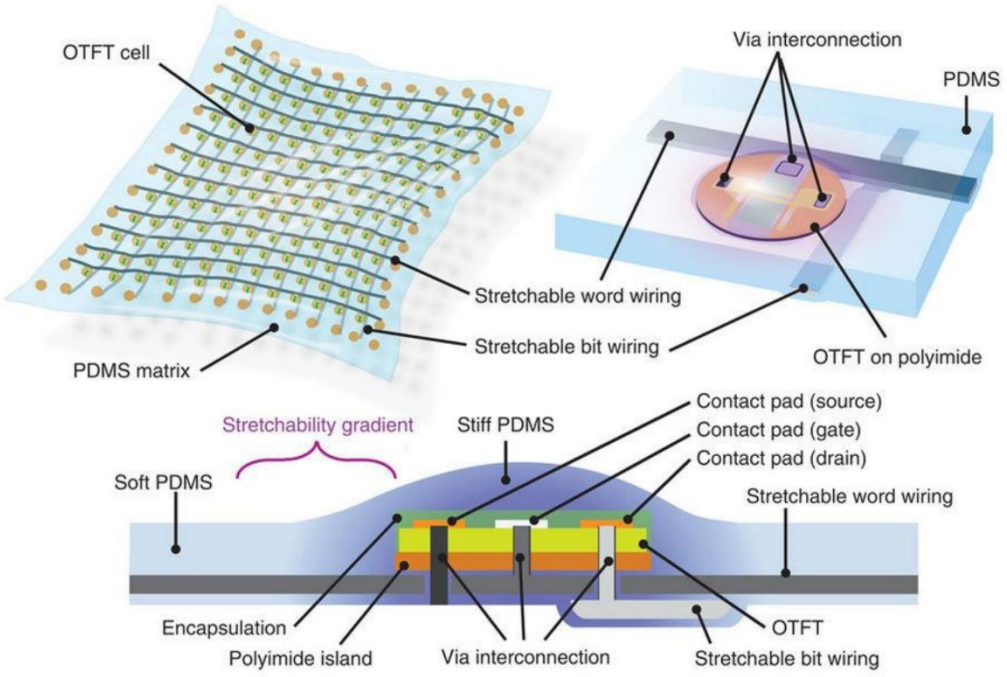

Figure 1-2. Illustration of stretchable TFT with rigid island structures. Upper left: whole matrix. Upper right: One TFT on a rigid island with elastic conductor wiring. Lower: One TFT on the PDMS substrate with stretchability gradient. Adapted and reproduced with permission from Ref. 52. Copyright 2015, Macmillan Publisher Limited.

Inorganic dielectrics with wrinkled structures possess high stretchability while maintaining excellent electrical performance as their flat configurations. However, the pre-stretching process required to obtain the wrinkle structures is cumbersome. Also, the inorganic dielectrics typically rely on costly vacuum-based deposition methods for fabrication, which is incompatible with solution printing processes. Furthermore, wavy structures can be incompatible with certain devices that require planar interfaces.[53] The electrical performance of the dielectrics with rigid island structures remain consistent with their original values because the stretchability is imparted by the stretchable regions between islands; however, a larger degree of

expansion usually requires a larger area of inactive substrate, which will cause a trade-off between the device density and stretchability.

As we introduced earlier, even though inorganic dielectrics have high dielectric constants, they are too brittle to adapt to stretchable matrices unless they incorporate wavy or island structures. The hunt for truly intrinsically stretchable dielectrics has turned to polymers.[54-55] Polymers are a natural choice given their inherent stretchability and insulating properties.

1.2 Applications of Polymeric Dielectric Materials

Due to their insulating and electromechanical transducing properties, polymeric dielectric materials are typically utilized in stretchable transistors, capacitive sensors and dielectric elastomer-based actuators. Considering the scope of this dissertation, discussions will be focused on dielectric elastomers and capacitive sensors.

1.2.1 Dielectric Elastomers

Electroactive polymer (EAP) is welled studied as "artificial muscle" due to its ability to mimic nature muscles.[56] EAP acts like a lightweight actuator that can deform under the stimulation of an electric field. Dielectric elastomer is one type of the most promising EAP that can impart large-strain actuation with an external electric field or convert mechanical energy into electricity.[31]

As shown in **Figure 1-3**, upon the application of the electric field, charges with opposite signs are induced on the electrodes that are at the opposite surfaces of the dielectric elastomer.[57]

Charges with the same sign along the same electrode surface repel each other, but attract the opposite charges from the opposite electrode surface. The film then expands in both x and y direction but shrink in the z direction due to the Maxwell forces. The Maxwell force generated during electrical actuation can be calculated by **Equation 1-1**:

$$\sigma = \varepsilon_0 \varepsilon_r (\frac{V}{d})^2 \qquad (1-1),$$

where σ denotes Maxwell pressure, ε_0 and ε_r indicate the absolute and relative dielectric constants respectively, and V d^{-1} shows the strength of electric field.[58] The electrodes deposited on both surfaces of the dielectric elastomer need to be compliant to accommodate large deformations.[59]

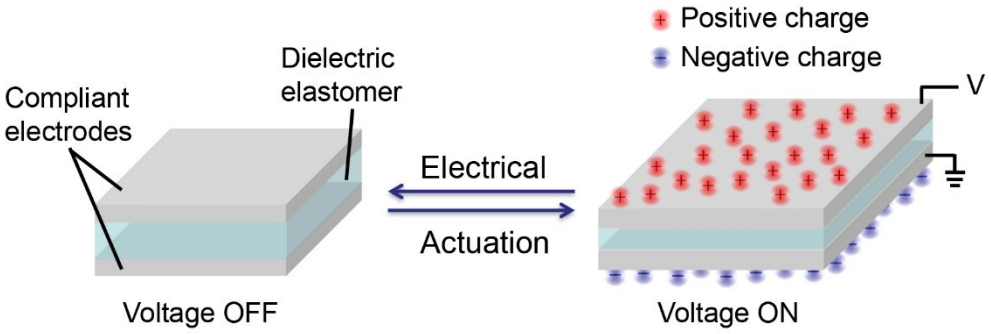

Figure 1-3. **Operating mechanism of dielectric elastomer.** With the application of electric field, the elastomer expands in area and reduces in thickness.

1.2.1.1 Materials Selection

There are several commonly used materials for dielectric elastomers. Silicones are usually selected due to their fast response time when compared to acrylic based dielectric

elastomers, though their induced strains are ~5 times smaller than that in acrylics due to the lower induced Maxwell pressures.[59-60] Commercial silicone, for example NuSil's CF19-21, has demonstrated a 63% strain with a 3.0 MPa Maxwell pressure, and its response time is less than 1 ms.[61] One way to enhance the electromechanical transducer property of silicone is to blend with highly polarizable conjugated polymers.[62] Carpt et al. mixed poly(3-hexylthiophene) (PHT) into silicone with a very low concentration (1-6 wt%). The best result with 1 wt% PHT showed an increase in dielectric constant, indicated by the transverse strain of 7.6% at only an 8 MV m^{-1} electric field with a small increase in dielectric loss and a small reduction in tensile elastic modulus. Interpenetrating polymer networks (IPN) also help to increase the dielectric constant of silicone-based elastomers.[63] Tugui et al. created a dual-phase continuous microstructure by interpenetrating PDMS with a polyurethane that contains tetramethyldisiloxane moieties and carboxyl groups. The polarity from the urethane groups and pendent carboxyl groups contribute to a high dielectric constant (12 at 1 Hz, 5.9 at 10 000 Hz) when compared to a pure PDMS film. This high dielectric constant induced a 7.1% strain actuation at an electric field of 20 MV m^{-1}. Due to the fast response time of silicone, it is suitable for dielectric elastomer generators, which was first proposed by Pelrine et al. in 2001.[64]

Polyurethane is another widely used dielectric elastomer thanks to its high dielectric constant as a comparison to silicone. The dielectric constant and modulus of PU are ~7 and 17 MPa as compared to 3 and 1 MPa of silicone.[65-66] Polyurethane is usually too stiff to result in large actuated strains.[67] Low cross-linked thermoplastic PU can generate large but permanent deformation.[68] When heated above its glass transition temperature, PU was reported to have a significant large response to electric field.[69] Hybrid method can also be used to improve the electromechanical performance of PU-based elastomers. Huang et al. blended a PU matrix with a

high dielectric constant copper phthalocyanine oligomer (PolyCuPc) and conductive PANI to achieve a 9.3% strain at a 20 MV m^{-1} electric field.[70]

The most frequently used dielectric elastomers are acrylics thanks to the relatively high dielectric constant and field strength of the neat films.[71] Another benefit of acrylics is their easy synthesis process which can be readily manipulated to enhance the electromechanical performance.[60] A commercial acrylic elastomer (3M's VHB 4910 series) demonstrates a high actuation strain, energy density and coupling efficiency.[32] Hu et al. reported a nanocomposite with a better actuation performance than pure acrylate copolymer by mixing a small amount of aluminum nanoparticles.[71] A 4 v/v% loading of Al_2O_3 nanoparticles resulted in a maximum 56% actuation area strain, 140 MV m^{-1} dielectric strength and an electric constant of 8.4. Even though higher actuation performance is observed with acrylics, their slow response time and high viscoelastic loss limit the overall efficiency. The maximum response frequency of the commercial VHB 4910 tape is 10-100 Hz.[60] This viscoelastic effect of acrylics renders them more suitable in large strain applications which don't have a requirement in respond time. One way to mitigate this viscoelasticity is to employ an interpenetrating polymer network. Matthew et al. diffused silicone chains into swollen acrylic rubber films with a following cross-linking treatment.[72] The resulting IPN films retained high strain performance with improved response time.

1.2.1.2 Applications for Dielectric Elastomers

The electromechanical transducing property of dielectric elastomers imparts a wide range of applications, such as refreshable braille display,[73-74] tunable lenses,[45] soft robotics, and energy harvesting generators.[39-40]

1.2.1.2.1 Soft Robotics

With the large actuation strains generated under electric fields, dielectric elastomers are suitable for mimicking human and animal movements. Duduta et al. reported a four-legged, multi-gait capable crawler as shown in **Figure 1-4(a)**.[38] This inchworm robot can be fabricated within few hours without the need of pre-stretch. The fast travelling speed (>1 body length / second) proves the fastest dielectric elastomer actuator-based robot reported to date. Another type of mobile robot with foldable dielectric elastomer actuators was introduced by Sun et al.[75] By taking advantage of the antagonistic configuration of two dielectric elastomers, Nyugen et al. fabricated a hexapod walking robot with two translations and one rotation movements.[76] This robot can move forward and backward with an average speed of 12 body length / minute as shown in **Figure 1-4(b)**. The maximal rolling speed was 42 mm s^{-1} with a 45 g soft robot under a 7.4 kV cyclic voltage. Li et al. demonstrated an underwater fish robot which employed the surrounding tap water (~50 mS m^{-1} of resistance) as the electric ground and can last for 3 hours with a single charge.[77] The fish robot acted like a manta ray with a speed of 0.69 body length / second by flapping fins under the actuation of a cyclic voltage (**Figure 1-4(c)**). As shown in **Figure 1-4(d)**, Zhao et al. created a rotary joint type of dielectric elastomers with minimum energy structures for flapping wings.[36] With inflated actuator designs and the antagonist configuration, Liu et al. created an actuator that can mimic the ocular muscular movement of the

human eyes (**Figure 1-4(e)**).[78] By adding stiff strips or fibers into dielectric elastomers, the elastomers only expanded in the orthogonal direction since the stripes prevented the elongation along the strips.[79] As shown in **Figure 1-4(f)**, Shian et al. illustrated a series of grippers that can bend asymmetrically.

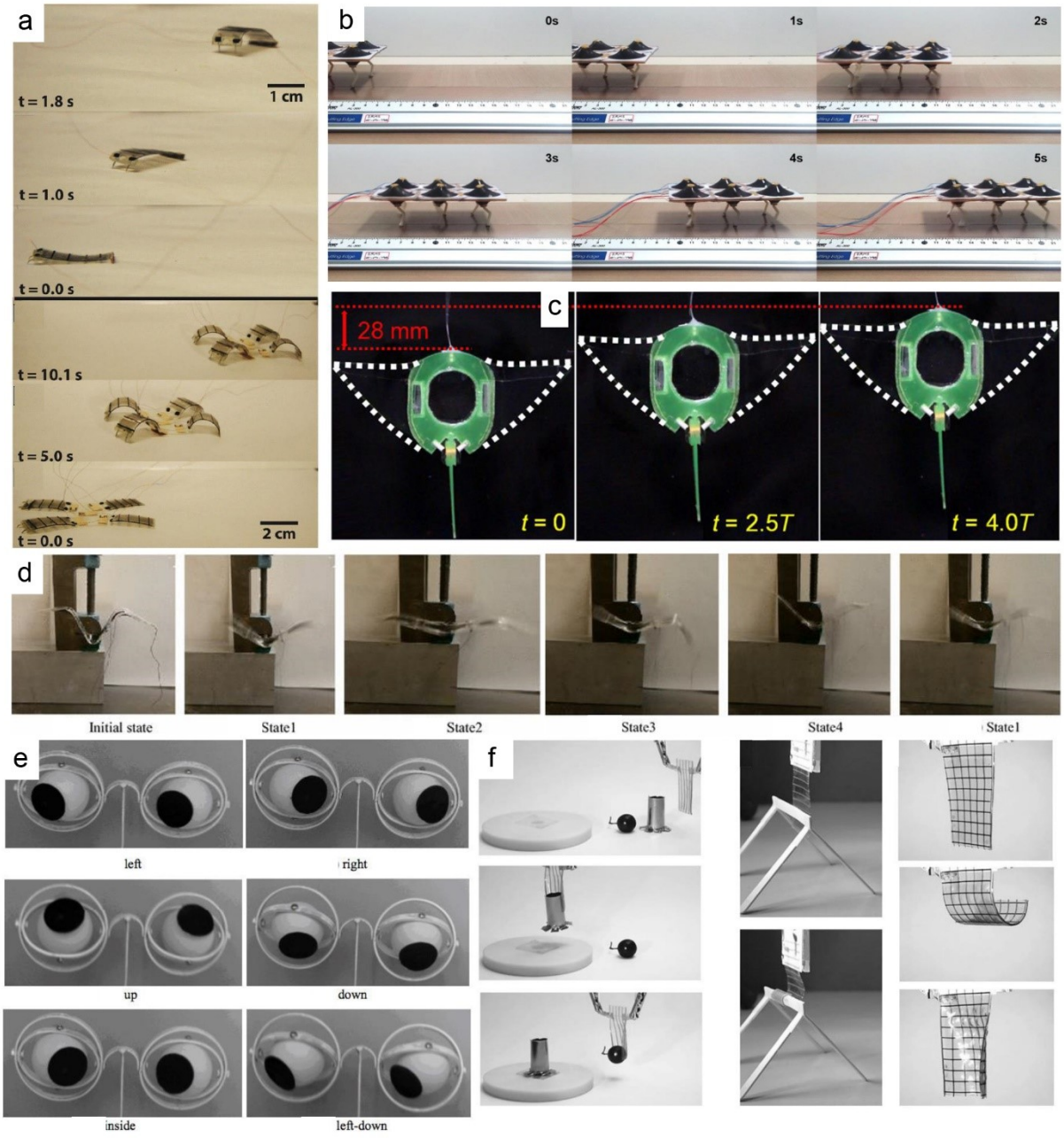

Figure 1-4. Soft robotics enabled by dielectric elastomers. (a) Top: an inchworm robot that was actuated at 10 Hz. Bottom: A crawling robot that was actuated at 1.5 Hz. **(b)** Forwarding locomotion of a hexapod robot that was actuated at 2 Hz. **(c)** Underwater swimming robotic fish. T is the time required for one full flapping cycle. **(d)** Flapping wings that were actuated at 5 Hz. **(e)** Pseudo-eyeballs movement that was actuated to mimic ocular muscle movement. **(f)** Left: Elastomeric gripper with vertical fibers. Middle: Elastomeric gripper with horizontal wrap action. Right: A combination of two actuators with orthogonal bending directions. Adapted and reproduced with permission from Ref. 38. Copyright 2017, IEEE; Ref. 76. Copyright 2017, Elsevier B.V.; Ref. 77. Copyright 2017, American Association for the Advancement of Science; Ref. 36. Copyright 2015, Springer; Ref. 78. Copyright 2008, SPIE; Ref. 79. Copyright 2015, WILEY-VCH.

1.2.1.2.2 Energy Harvesting Generators

By following the opposite energy transferring direction of actuators, dielectric elastomers provide a simple way for energy harvesting from mechanical energy sources. The concept of dielectric elastomer generators was first brought up by Pelrine et al. in 2001 followed by the creation of different generator configurations.[64, 67, 80] Basically, the capacitance change of a dielectric elastomer between an initially strained state and a relaxed state will lead to a change in the potential of charges, and thus the electrical potential energy. Brochu et al. introduced a silicone based generator whose capacitance increased by almost 3.5 times with a 100% applied strain (**Figure 1-5(a)**).[41] For a peak voltage (1800 V), the harvest energy was 7.5 mJ cm^{-3} for a 50% strained sample at a strain rate of 100% per second. By applying this energy harvesting generators on human joints, where large bending happens, energy can be generated to support wearable devices. A shown in **Figure 1-5(b)**, Li et al. presented a triboelectric nanogenerator

with the combined structure of a planar "dielectric-conductive-dielectric" part and a wavy "conductive-dielectric-conductive" part.[18, 42] The wavy structure allowed bending, stretching and pressing of the generator and created a maximized volume charge density of 0.055 C m^{-3}, which was used to continuously drive an electronic watch. When attached to the bottom of a pair of shoes, the energy generator self-powered a pedometer and a fitness tracker when the user was jogging (**Figure 1-5(c)**). In their following work, a generator with an ultrahigh stretchability of 1160% and 96.2% transparency was fabricated to output an open-circuit voltage of 145 V and an instantaneous areal power density of 35 mW m^{-2}.[15] As shown in **Figure 1-5(d)**, the generator powered up 20 LEDs at both initial state and stretched states with finger tapping. The transparent generator was also attached on top of a liquid crystal display to drive the screen with finger pressing.

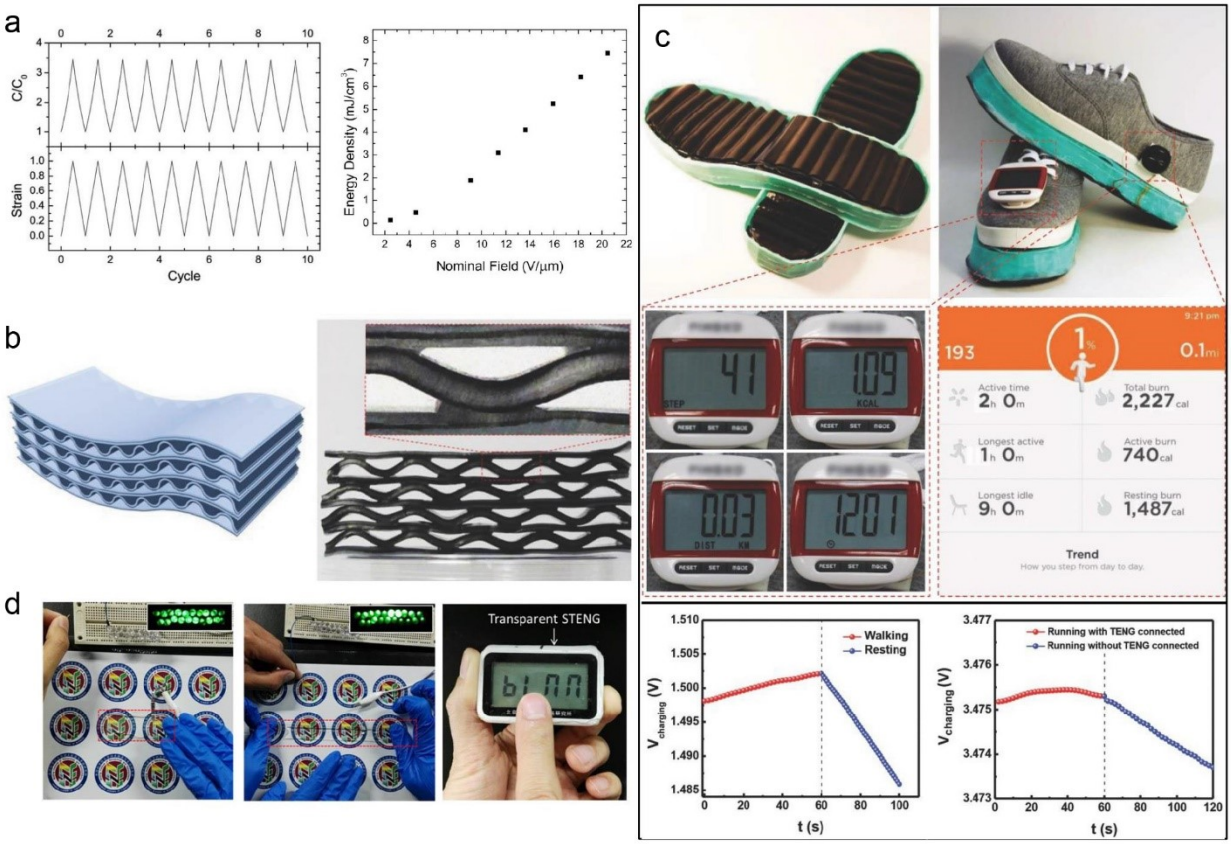

Figure 1-5. Demonstrations of energy harvesting generators. (a) Left: Capacitance change with 100% tensile strain for 10 cycles. Right: Energy-harvesting density as a function of nominal applied electric field (strain: 50%, strain rate: 100% s^{-1}). **(b)** Structure of a multilayer triboelectric nanogenerator. **(c)** Top: Demonstration of self-powered shoes that are based on multilayer triboelectric generators with the function of pedometer and fitness track enabled. Bottom: The voltages of energy storage unit while the nanogenerators were driving the pedometer and the fitness tracker. **(d)** 20 LEDs were powered by tapping on a triboelectric nanogenerator when the generator was (left) relaxed and (middle) stretched. Right: An LCD screen was driven by a transparent nanogenerator with finger pressing. Adapted and reproduced with permission from Ref. 41. Copyright 2013, WILEY-VCH; Ref. 42. Copyright 2017, WILEY-VCH; Ref. 15. Copyright 2017, American Association for the Advancement of Science.

1.2.2 Capacitive Sensors

Dielectric materials are extensively used as capacitive sensors due to the sensitive capacitance change with application of stimuli, and their adaptability to wearable devices. The most popular design of capacitive sensors is parallel-plate configuration since they are easy and straight forward to fabricate. **Figure 1-6** shows the architecture of the parallel-plate sensors. A dielectric layer is sandwiched between two conductive electrodes. Based on **Equation 1-2**,

$$\mathrm{C} = \frac{\varepsilon_0 \varepsilon_r A}{d} \qquad (1-2),$$

where ε_0 is permittivity, ε_r is dielectric constant of the dielectric film, A is the area of the electrode and d is the average thickness of the dielectric film. By tuning the thickness of the dielectric layer, the capacitance of this capacitor will change accordingly.

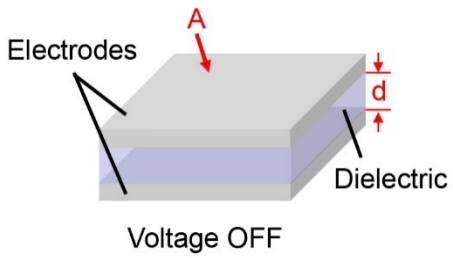

Figure 1-6. **Illustration of parallel-plate capacitor.** A is the area of the electrode and d is the average thickness of the dielectric film.

Compared to transistor-based pressure sensors, capacitive sensors are more power efficient.[81] Viry et al. developed a three-axis soft tactile capacitive sensor that can detect a wide range of pressure values from 100 Pa for heartbeat monitoring to 400 kPa for foot pressure distribution monitoring.[82] Ultra-small capacitive sensors was fabricated with sizes of 1 x 1 x 0.1 mm^3 by Chen et al. to capture human pulse waveforms in real time.[83] The 0 ~ 100 mm Hg detected pressure range was good for physiological sensing, which was further approved by the in vivo mice intracranial pressure monitoring. Other than contact sensing, Minpyo et al. realized a non-contact sensor to recognize the three-dimensional (3D) shapes and the distances of approaching objects.[84]

The sensitivity of parallel-plate sensors is usually small due to the neglect thickness change of the dielectric layer with external pressures. To improve the sensitivity of parallel-plate capacitors, the electrode or dielectric layers of the pressure sensor can be patterned with microstructures.[34, 85-86] Ozgur employed solid particle leaching method to fabricated a microporous dielectric layer by dissolving sugar granules away (**Figure 1-7(a)**).[87] When combined with knitted conductive fabrics, the resulted sensor can detect up to 1 MPa pressure

with sensitivity of 121 x 10 $^{-4}$ kPa^{-1}. Another piezocapacitive sensor with micro-sized pores were developed by Donguk at el. with sensitivity of 0.601 kPa^{-1} within the low-pressure regime.[88] Shuai et al. utilized a buckled bottom electrode with PVDF as the dielectric and achieved a pressure sensor with a sensitivity as high as 2.94 kPa^{-1}, and a low detection limit which was smaller than 3 Pa (**Figure 1-7(b)**).[34, 85] The sensor that was attached to a human neck successfully detected the voice vibration during speech. Besides deformation through pressure, tensile force can also result in the thinning of a dielectric layer, which renders a strain-sensing property to the parallel-plate sensor. Brochu et al. fabricated a sandwich-structured sensor with a silicone based dielectric and carbon nanotube composite electrodes.[41]

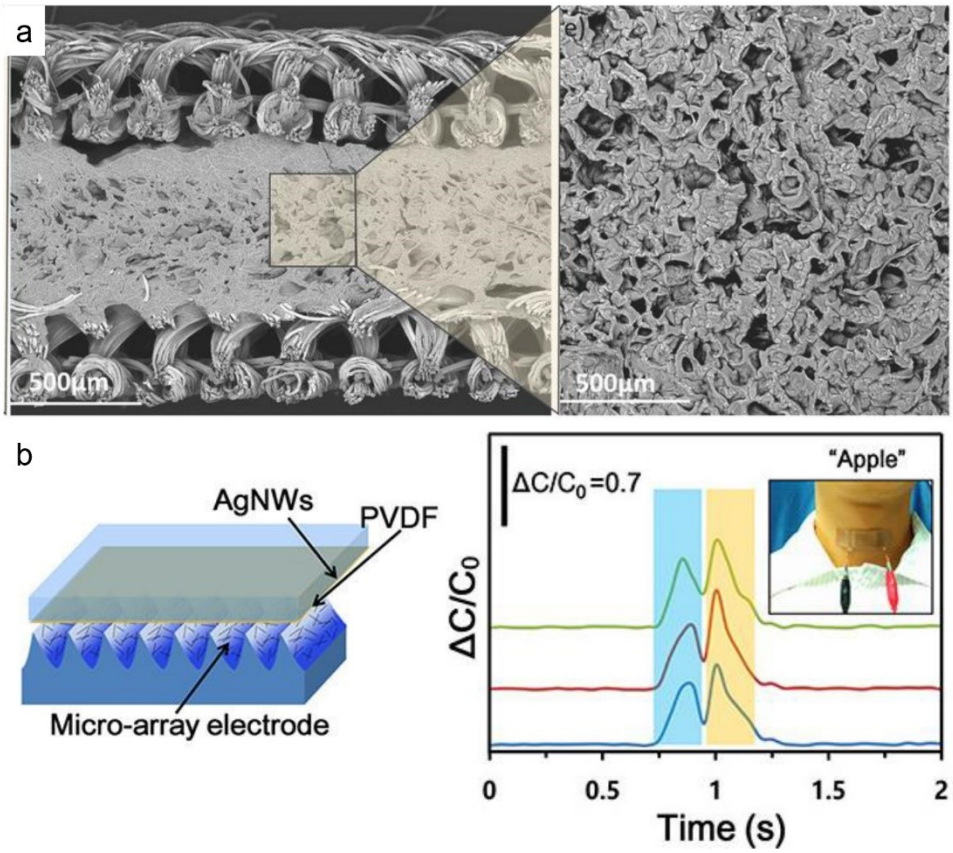

Figure 1-7. Structure and performance of capacitive pressure sensors. (a) Left: Cross-sectional SEM image of the sensor. Right: Enlarged SEM image showing microporous dielectric layer. **(b)** Left: Sandwiched structure of the capacitive sensor with patterned bottom electrode. Right: Real-time capacitance change of a flexible pressure sensor with three times of pronunciation of "Apple". Adapted and reproduced with permission from Ref. 87. Copyright 2017, WILEY-VCH; Ref. 34. Copyright 2017, American Chemical Society.

1.3 Bistable Electroactive Polymer

With the modern demand for flexible and stretchable electronic devices, polymeric dielectric materials have gain tremendous attentions. For dielectric elastomers, customized strains can be actuated with varied external electric field. But the maintenance of the large deformation requires consistent input of energy, which impede the practical employment of dielectric elastomers in real life. To reduce the energy consumption, researchers have turned their ways to bistable electroactive polymers (BSEPs). BSEP is a type of dielectric elastomer that has phase transition-induced shape memory property, which can achieve a rigid-to-rigid actuation.[73] A typical working principle of BSEP is shown in **Figure** 1-**8**. Below transition temperature, BSEP possesses high elastic modulus and acts like rigid material. It can turn into rubbery elastomer when heated above its transition temperature and behaves like dielectric elastomer. In the rubbery state, BSEP can be actuated into different shapes by the application of electric field. This deformation is maintained without an electric field by cooling the BSEP below transition temperature. By re-heating the BSEP above its transition temperature without applied electric field, the shape change could be restored.

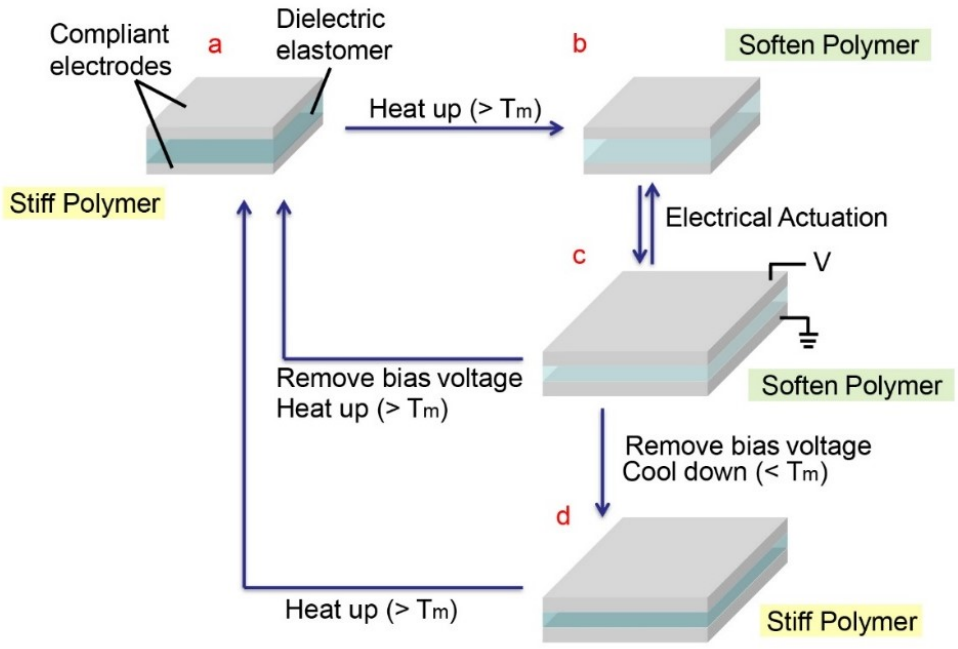

Figure 1-8. Schematic illustration of actuation mechanism of BSEP. The rigid nanocomposite (a) softens upon heating above its phase-changing temperature (b), applied electric field actuates the softened polymer (c), film returns to rigid state when cooled below the phase-change temperature, locking the large applied strain (d), and the film recovers its original rigid shape (a) by heating above the phase-changing temperature and then cooling back down.

The rigid-to-rigid actuation of BSEP not only saves tremendous energy to preserve the film's deformation, it also provides stronger mechanical support for adaptive structures while not compromising large actuation strain. One adaptive structure application, braille display, can benefits from the energy conservation and high mechanical modulus for finger touching experience. Braille consists of 2 columns of 3 dots for each character.[89] A typical height for the dot in each character is 0.5 mm, and the diameter of the dot ranges from 1.27 mm to 1.65 mm.[90-91] Pei group developed a refreshable and bistable braille display by taking advantage of

BSEP.[43, 73-74, 92] By heating above its transition temperature, the dielectric elastomer can be actuated to form domes with an external electric field as shown in **Figure 1-9**.[92] The deformation was locked after the temperature dropped. The force that was applied vertically on the top of the dome was calculated to be 0.6 N, and a full refreshing cycle took about 40 seconds.

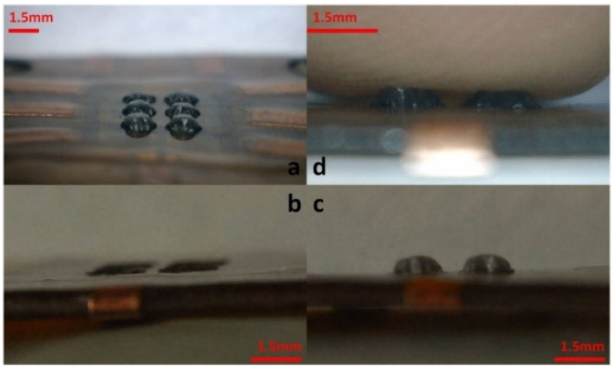

Figure 1-9. A six-dot Braille character display. (a) All six dots were at ON state. **(b)** Side view of OFF state. **(c)** Side view of ON state. **(d)** Braille character (ON state) was touched by a human finger. Adapted and reproduced with permission from Ref. 92. Copyright 2012, SPIE.

1.4 Scope and Layout of the Dissertation

Based on the previous introduction, polymeric dielectric materials show promising potentials in electromechanical transducing and capacitive sensing applications. The combined phase transition-induced shape memory property in BSEP material further facilitate its practical appliance prospectus since it saves great energy to retain the shape deformation of BSEP. The dielectric, electroactive and phase transition properties of the as mentioned BSEP were studied and adapted for specific applications in this dissertation. Based on each aspect of these properties, unique devices, such as rewritable photonic paper, light modulation smart window and fiber-based pressure sensor were developed.

This dissertation is divided into five chapters.

The current chapter, Chapter 1, gives an overview of polymeric dielectric materials, focusing on their dielectric and electroactive properties with applications. One type of dielectric materials, BSEP, was also introduced here.

In Chapter 2, the electroactive and shape memory properties of BSEP were taken advantaged by combining them with photonic crystals to fabricate an ink-free rewritable paper concept that matches the benefits of paper as a zero-energy, long-term data storage medium, but provides the additional advantage of rewritability. The rewritable paper consists of a ferroferric oxide-carbon (Fe_3O_4@C) core–shell nanoparticle (NP)-based photonic crystal embedded in a BSEP. Electrical actuation induces large deformation in the z-axis of the nanocomposite, creating distinct color change in the actuated area. This nanocomposite stores high fidelity color images without inks, the images remain stable after more than a year of storage in ambient conditions without external energy supply thanks to the rigid-to-rigid actuation of BSEP. The stored images can then be rewritten over 500 times without degrading. In this work, 7 segmented electrodes were designed to display digits whereas with electrode pixel arrays, images can be created as desired. Given this material's strengths, it shows promise in replacing information displays with long demonstration times but low refresh frequencies, such as billboards and tags.

Chapter 3 exploits the phase transition aspect of the as mentioned BSEP material. The phase transition property of BSEP is realized through the amorphous-to-semicrystalline transition of one constituent polymer, stearyl acrylate (SA). Below melting temperature (T_m), SA is crystallized and opaque; whereas when above T_m, SA transforms into amorphous and transparent state. Based on this opaque-to-transparent transition of BSEP, a light modulation

smart window was designed. The BSEP film was further improved to cover the whole solar spectrum by introducing micro-sized phase separations. A silver nanowire (AgNW) based transparent heater was combined with the smart windows (SW) film to control the amorphous-to-semicrystalline transition more easily. The final smart window application can achieve a large luminous transmittance modulation (ΔT_{lum}) of 80.4% and solar transmittance modulation (ΔT_{solar}) of 70.2%, which rivals the performance of the best reported smart windows. And this work is the first one to report an all-solid thermochromic smart window without the inclusion of any metal/metal oxides or liquid crystals to enable strong control in the full solar spectrum.

Chapter 4 focus on the dielectric property of polymeric dielectric materials. Instead of constructing capacitive sensors with planar parallel-plate design, a fibrous capacitive pressure sensor was fabricated in this chapter. TEMPO-oxidized bacterial cellulose (TOBC)/silver nanowire (AgNW) composite fibers were used as the conducting cores of the sensor. The excellent flexibility, high strength and biocompatibility of TOBC makes the sensor suitable for wearable devices. A layer of PDMS was covered on the outside of TOBC/AgNW fibers as the dielectric layer. Due to the porous hierarchical structure of TOBC/AgNW core, the TOBC/AgNW/PDMS fibrous sensor can sustain larger deformation, thus has higher sensitivity towards pressures. A voice detector was fabricated on the basis of this sensor. The small pressure changes on throat when speaking different numbers (1-10) can be recognized and distinguished. A machine learning model was built to classify the spoken numbers from the voice waveform. And 90.7% of predictive accuracy on test data was achieved through a random forest model.

Chapter 5 provides an outlook for future research and concludes this dissertation.

1.5 Reference

[1] J. Lee, J. Wu, M. Shi, J. Yoon, S. I. Park, M. Li, Z. Liu, Y. Huang, J. A. Rogers, *Advanced Materials* **2011**, 23, 986.

[2] M. Kaltenbrunner, G. Kettlgruber, C. Siket, R. Schwödiauer, S. Bauer, *Advanced materials* **2010**, 22, 2065.

[3] J. Liang, L. Li, X. Niu, Z. Yu, Q. Pei, *Nature Photonics* **2013**, 7, 817.

[4] J. Liang, L. Li, K. Tong, Z. Ren, W. Hu, X. Niu, Y. Chen, Q. Pei, *ACS nano* **2014**, 8, 1590.

[5] Z. Fan, H. Razavi, J.-w. Do, A. Moriwaki, O. Ergen, Y.-L. Chueh, P. W. Leu, J. C. Ho, T. Takahashi, L. A. Reichertz, *Nature materials* **2009**, 8, 648.

[6] D. J. Lipomi, B. C. K. Tee, M. Vosgueritchian, Z. Bao, *Advanced Materials* **2011**, 23, 1771.

[7] S. M. Mirvakili, I. W. Hunter, *Advanced Materials* **2018**, 30, 1704407.

[8] R. Pelrine, R. Kornbluh, Q. Pei, J. Joseph, *Science* **2000**, 287, 836.

[9] J. Liang, L. Li, D. Chen, T. Hajagos, Z. Ren, S.-Y. Chou, W. Hu, Q. Pei, *Nature communications* **2015**, 6, 7647.

[10] T. Q. Trung, S. Ramasundaram, B. U. Hwang, N. E. Lee, *Advanced materials* **2016**, 28, 502.

[11] M.-Y. Wu, J. Zhao, F. Xu, T.-H. Chang, R. M. Jacobberger, Z. Ma, M. S. Arnold, *Applied Physics Letters* **2015**, 107, 75_1.

[12] R. A. Doganov, E. C. O'Farrell, S. P. Koenig, Y. Yeo, A. Ziletti, A. Carvalho, D. K. Campbell, D. F. Coker, K. Watanabe, T. Taniguchi, *Nature communications* **2015**, 6, 6647.

[13] M. Kaltenbrunner, T. Sekitani, J. Reeder, T. Yokota, K. Kuribara, T. Tokuhara, M. Drack, R. Schwödiauer, I. Graz, S. Bauer-Gogonea, *Nature* **2013**, 499, 458.

[14] X. Wang, L. Dong, H. Zhang, R. Yu, C. Pan, Z. L. Wang, *Advanced Science* **2015**, 2, 1500169.

[15] X. Pu, M. Liu, X. Chen, J. Sun, C. Du, Y. Zhang, J. Zhai, W. Hu, Z. L. Wang, *Science advances* **2017**, 3, e1700015.

[16] Q. Wang, M. Jian, C. Wang, Y. Zhang, *Advanced Functional Materials* **2017**, 27, 1605657.

[17] P. Polygerinos, N. Correll, S. A. Morin, B. Mosadegh, C. D. Onal, K. Petersen, M. Cianchetti, M. T. Tolley, R. F. Shepherd, *Advanced Engineering Materials* **2017**, 19, 1700016.

[18] X. Chen, X. Pu, T. Jiang, A. Yu, L. Xu, Z. L. Wang, *Advanced Functional Materials* **2017**, 27, 1603788.

[19] J. C. Nawroth, H. Lee, A. W. Feinberg, C. M. Ripplinger, M. L. McCain, A. Grosberg, J. O. Dabiri, K. K. Parker, *Nature biotechnology* **2012**, 30, 792.

[20] J. H. Lee, K. Y. Lee, M. K. Gupta, T. Y. Kim, D. Y. Lee, J. Oh, C. Ryu, W. J. Yoo, C. Y. Kang, S. J. Yoon, *Advanced Materials* **2014**, 26, 765.

[21] C. K. Jeong, J. Lee, S. Han, J. Ryu, G. T. Hwang, D. Y. Park, J. H. Park, S. S. Lee, M. Byun, S. H. Ko, *Advanced materials* **2015**, 27, 2866.

[22] S. Park, H. Kim, M. Vosgueritchian, S. Cheon, H. Kim, J. H. Koo, T. R. Kim, S. Lee, G. Schwartz, H. Chang, *Advanced Materials* **2014**, 26, 7324.

[23] F. Yi, L. Lin, S. Niu, P. K. Yang, Z. Wang, J. Chen, Y. Zhou, Y. Zi, J. Wang, Q. Liao, *Advanced Functional Materials* **2015**, 25, 3688.

[24] C. L. Choong, M. B. Shim, B. S. Lee, S. Jeon, D. S. Ko, T. H. Kang, J. Bae, S. H. Lee, K. E. Byun, J. Im, *Advanced materials* **2014**, 26, 3451.

[25] L. Cai, S. Zhang, Y. Zhang, J. Li, J. Miao, Q. Wang, Z. Yu, C. Wang, *Advanced Materials Technologies* **2018**, 3, 1700232.

[26] X. Wang, Y. Zhang, X. Zhang, Z. Huo, X. Li, M. Que, Z. Peng, H. Wang, C. Pan, *Advanced Materials* **2018**, 30, 1706738.

[27] Q. Hua, J. Sun, H. Liu, R. Bao, R. Yu, J. Zhai, C. Pan, Z. L. Wang, *Nature communications* **2018**, 9, 244.

[28] R. Ma, B. Kang, S. Cho, M. Choi, S. Baik, *ACS nano* **2015**, 9, 10876.

[29] T. Yamada, Y. Hayamizu, Y. Yamamoto, Y. Yomogida, A. Izadi-Najafabadi, D. N. Futaba, K. Hata, *Nature nanotechnology* **2011**, 6, 296.

[30] P. H. Vargantwar, A. E. Özçam, T. K. Ghosh, R. J. Spontak, *Advanced Functional Materials* **2012**, 22, 2100.

[31] F. Carpi, I. Anderson, S. Bauer, G. Frediani, G. Gallone, M. Gei, C. Graaf, C. Jean-Mistral, W. Kaal, G. Kofod, *Smart Materials and Structures* **2015**, 24, 105025.

[32] D. Chen, Q. Pei, *Chemical reviews* **2017**, 117, 11239.

[33] S. Wang, J. Xu, W. Wang, G.-J. N. Wang, R. Rastak, F. Molina-Lopez, J. W. Chung, S. Niu, V. R. Feig, J. Lopez, *Nature* **2018**, 555, 83.

[34] X. Shuai, P. Zhu, W. Zeng, Y. Hu, X. Liang, Y. Zhang, R. Sun, C.-p. Wong, *ACS applied materials & interfaces* **2017**, 9, 26314.

[35] S. Ji, J. Jang, E. Cho, S. H. Kim, E. S. Kang, J. Kim, H. K. Kim, H. Kong, S. K. Kim, J. Y. Kim, *Advanced Materials* **2017**, 29, 1700538.

[36] J. Zhao, J. Niu, D. McCoul, J. Leng, Q. Pei, *Meccanica* **2015**, 50, 2815.

[37] D. Rus, M. T. Tolley, *Nature* **2015**, 521, 467.

[38] M. Duduta, D. R. Clarke, R. J. Wood, presented at 2017 IEEE International Conference on Robotics and Automation (ICRA) **2017**.

[39] D. Yurchenko, Z. Lai, G. Thomson, D. Val, R. Bobryk, *Applied energy* **2017**, 208, 456.

[40] X. Zhao, P. Sharma, *Soft Matter* **2017**, 13, 4552.

[41] P. Brochu, H. Stoyanov, R. Chang, X. Niu, W. Hu, Q. Pei, *Advanced Energy Materials* **2014**, 4, 1300659.

[42] S. Li, J. Wang, W. Peng, L. Lin, Y. Zi, S. Wang, G. Zhang, Z. L. Wang, *Advanced Energy Materials* **2017**, 7, 1602832.

[43] X. Niu, P. Brochu, B. Salazar, Q. Pei, presented at Electroactive Polymer Actuators and Devices (EAPAD) 2011 **2011**.

[44] Y. Qiu, Z. Lu, Q. Pei, *ACS applied materials & interfaces* **2018**, 10, 24807.

[45] F. Carpi, G. Frediani, S. Turco, D. De Rossi, *Advanced Functional Materials* **2011**, 21, 4152.

[46] S. H. Chae, W. J. Yu, J. J. Bae, D. L. Duong, D. Perello, H. Y. Jeong, Q. H. Ta, T. H. Ly, Q. A. Vu, M. Yun, *Nature materials* **2013**, 12, 403.

[47] F. Xu, M.-Y. Wu, N. S. Safron, S. S. Roy, R. M. Jacobberger, D. J. Bindl, J.-H. Seo, T.-H. Chang, Z. Ma, M. S. Arnold, *Nano letters* **2014**, 14, 682.

[48] T. Sekitani, Y. Noguchi, K. Hata, T. Fukushima, T. Aida, T. Someya, *Science* **2008**, 321, 1468.

[49] D.-H. Kim, J. Song, W. M. Choi, H.-S. Kim, R.-H. Kim, Z. Liu, Y. Y. Huang, K.-C. Hwang, Y.-w. Zhang, J. A. Rogers, *Proceedings of the National Academy of Sciences* **2008**, 105, 18675.

[50] Y. Mengüç, Y.-L. Park, H. Pei, D. Vogt, P. M. Aubin, E. Winchell, L. Fluke, L. Stirling, R. J. Wood, C. J. Walsh, *The International Journal of Robotics Research* **2014**, 33, 1748.

[51] H. L. Filiatrault, G. C. Porteous, R. S. Carmichael, G. J. Davidson, T. B. Carmichael, *Advanced Materials* **2012**, 24, 2673.

[52] N. Matsuhisa, M. Kaltenbrunner, T. Yokota, H. Jinno, K. Kuribara, T. Sekitani, T. Someya, *Nature communications* **2015**, 6, 7461.

[53] D. J. Lipomi, Z. Bao, *Energy & Environmental Science* **2011**, 4, 3314.

[54] J. Ge, L. Sun, F. R. Zhang, Y. Zhang, L. A. Shi, H. Y. Zhao, H. W. Zhu, H. L. Jiang, S. H. Yu, *Advanced Materials* **2016**, 28, 722.

[55] J. Xu, S. Wang, G.-J. N. Wang, C. Zhu, S. Luo, L. Jin, X. Gu, S. Chen, V. R. Feig, J. W. F. To, *Science* **2017**, 355, 59.

[56] W. Roentgen, *Ann. Phys. Chem* **1880**, 11, 771.

[57] Q. Pei, M. A. Rosenthal, R. Pelrine, S. Stanford, R. D. Kornbluh, presented at Smart Structures and Materials 2003: Electroactive Polymer Actuators and Devices (EAPAD) **2003**.

[58] X. Niu, H. Stoyanov, W. Hu, R. Leo, P. Brochu, Q. Pei, *Journal of Polymer Science Part B: Polymer Physics* **2013**, 51, 197.

[59] Z. Suo, *Acta Mechanica Solida Sinica* **2010**, 23, 549.

[60] P. Brochu, Q. Pei, *Macromolecular rapid communications* **2010**, 31, 10.

[61] Y. Bar-Cohen, S. P. Leary, M. Shahinpoor, J. S. Harrison, J. G. Smith, presented at Smart Structures and Materials 1999: Electroactive Polymer Actuators and Devices **1999**.

[62] F. Carpi, G. Gallone, F. Galantini, D. De Rossi, *Advanced Functional Materials* **2008**, 18, 235.

[63] C. Tugui, S. Vlad, M. Iacob, C. Varganici, L. Pricop, M. Cazacu, *Polymer Chemistry* **2016**, 7, 2709.

[64] R. Pelrine, R. D. Kornbluh, J. Eckerle, P. Jeuck, S. Oh, Q. Pei, S. Stanford, presented at Smart Structures and Materials 2001: Electroactive Polymer Actuators and Devices **2001**.

[65] X. Niu, R. Leo, D. Chen, W. Hu, Q. Pei, presented at Electroactive Polymer Actuators and Devices (EAPAD) 2013 **2013**.

[66] R. Pelrine, R. Kornbluh, J. Joseph, R. Heydt, Q. Pei, S. Chiba, *Materials Science and Engineering: C* **2000**, 11, 89.

[67] P. Brochu, Q. Pei, in *Electroactivity in Polymeric Materials*, Springer **2012**, p. 1.

[68] J. Biggs, K. Danielmeier, J. Hitzbleck, J. Krause, T. Kridl, S. Nowak, E. Orselli, X. Quan, D. Schapeler, W. Sutherland, *Angewandte Chemie International Edition* **2013**, 52, 9409.

[69] Q. Zhang, J. Su, C. H. Kim, R. Ting, R. Capps, *Journal of Applied Physics* **1997**, 81, 2770.

[70] C. Huang, Q. Zhang, G. DeBotton, K. Bhattacharya, *Applied Physics Letters* **2004**, 84, 4391.

[71] W. Hu, S. N. Zhang, X. Niu, C. Liu, Q. Pei, *Journal of Materials Chemistry C* **2014**, 2, 1658.

[72] G. Mathew, J. Rhee, C. Nah, D. Leo, *Polymer Engineering & Science* **2006**, 46, 1455.

[73] Z. Yu, W. Yuan, P. Brochu, B. Chen, Z. Liu, Q. Pei, *Applied Physics Letters* **2009**, 95, 192904.

[74] Z. Ren, X. Niu, D. Chen, W. Hu, Q. Pei, presented at Electroactive Polymer Actuators and Devices (EAPAD) 2014 **2014**.

[75] W. Sun, F. Liu, Z. Ma, C. Li, J. Zhou, *Journal of Applied Physics* **2016**, 120, 084901.

[76] C. T. Nguyen, H. Phung, T. D. Nguyen, H. Jung, H. R. Choi, *Sensors and Actuators A: Physical* **2017**, 267, 505.

[77] T. Li, G. Li, Y. Liang, T. Cheng, J. Dai, X. Yang, B. Liu, Z. Zeng, Z. Huang, Y. Luo, *Science Advances* **2017**, 3, e1602045.

[78] Y. Liu, L. Shi, L. Liu, Z. Zhang, J. Leng, presented at Electroactive Polymer Actuators and Devices (EAPAD) 2008 **2008**.

[79] S. Shian, K. Bertoldi, D. R. Clarke, *Advanced Materials* **2015**, 27, 6814.

[80] C. Jean-Mistral, S. Basrour, J.-J. Chaillout, presented at Electroactive Polymer Actuators and Devices (EAPAD) 2008 **2008**.

[81] S. Wan, H. Bi, Y. Zhou, X. Xie, S. Su, K. Yin, L. Sun, *Carbon* **2017**, 114, 209.

[82] L. Viry, A. Levi, M. Totaro, A. Mondini, V. Mattoli, B. Mazzolai, L. Beccai, *Advanced Materials* **2014**, 26, 2659.

[83] L. Y. Chen, B. C.-K. Tee, A. L. Chortos, G. Schwartz, V. Tse, D. J. Lipomi, H.-S. P. Wong, M. V. McConnell, Z. Bao, *Nature communications* **2014**, 5, 5028.

[84] M. Kang, J. Kim, B. Jang, Y. Chae, J.-H. Kim, J.-H. Ahn, *ACS nano* **2017**, 11, 7950.

[85] S. Pyo, J. Choi, J. Kim, *Advanced Electronic Materials* **2018**, 4, 1700427.

[86] Y. Joo, J. Byun, N. Seong, J. Ha, H. Kim, S. Kim, T. Kim, H. Im, D. Kim, Y. Hong, *Nanoscale* **2015**, 7, 6208.

[87] O. Atalay, A. Atalay, J. Gafford, C. Walsh, *Advanced Materials Technologies* **2018**, 3, 1700237.

[88] D. Kwon, T.-I. Lee, J. Shim, S. Ryu, M. S. Kim, S. Kim, T.-S. Kim, I. Park, *ACS applied materials & interfaces* **2016**, 8, 16922.

[89] Y. Bar-Cohen, presented at Electroactive Polymer Actuators and Devices (EAPAD) 2010 **2010**.

[90] Y. Kato, T. Sekitani, M. Takamiya, M. Doi, K. Asaka, T. Sakurai, T. Someya, *IEEE transactions on electron devices* **2007**, 54, 202.

[91] M. Matysek, P. Lotz, H. F. Schlaak, presented at Electroactive Polymer Actuators and Devices (EAPAD) 2009 **2009**.

[92] X. Niu, P. Brochu, H. Stoyanov, S. R. Yun, Q. Pei, presented at Electroactive Polymer Actuators and Devices (EAPAD) 2012 **2012**.

Chapter 2

Bistable and Reconfigurable Photonic Crystals – Electroactive Shape Memory Polymer Nanocomposite for Ink-free Rewritable Paper

2.1 Introduction

Recent attempts to create and popularize rewritable paper can greatly lessen the heavy environmental burden brought about by traditional pulp and paper industry.[1][2] Currently, paper-replacement effort is developing around several distinct technologies: electrophoretic inks,[3-7] electrowetting inks,[8-9] cholesteric liquid-crystals,[10-13] reprintable coatings on paper[14-17] and responsive photonic crystals.[18-39] Microencapsulated electrophoretic display was first introduced by a MIT group in 1998,[3] which quickly enabled the commercially successful, monochromic e-readers popular for their low power consumption due to its bistability and paper-like legibility under sunlight. A reliable full-color electrophoretic e-paper with simple fabrication process is yet to be achieved.[4-5] Current proposals either suffer from significant reflected light intensity loss due to color filters, or require complex manufacturing processes to create sub-

pixels with different colors and convoluted charging system.[6-7] Electrowetting displays are another commercialized electronic paper that was invented by Liquavista® in 2003.[8] They were capable of framerates suitable for video-play with their fast switching speed through applied voltages.[9] However, electrowetting displays are not bistable, and they consume extra energy to keep the pixels in uncolored states. Kent Displays developed the most paper-like writing tablet, the Boogie board®, which delivers a natural writing experience based on the reorientation of cholesteric liquid crystals (CLCs) under stylus pressure.[10-13] CLC displays also consume zero energy to maintain the written contents, due to the inherent bistability of the cholesteric texture. However, the pitch of the underlying CLC, and by extension the displayed color, is predetermined during manufacturing, making the display elements monochromatic. As for reprintable paper coatings, reconfigurable dyes are adaptable to laser or ink-jet printer designs,[14-17] but the dyes are usually toxic and cost prohibitive, and the colors are only temporary, for they disappear over the course of a few days as the organic dyes oxidize.

Compared to dyes used in most current commercial e-papers, photonic crystals, which derive their colors from structures, exhibit brighter colors, are more stable, and are resistant to photobleaching.[40] Furthermore, full-color presentation is easier to achieve without needing complicated sub-pixel systems, as the reflected color (also called the "stopband") of the photonic crystals is easily modulated by changing the lattice constant or the refractive index of the photonic crystal, achievable through pH control, chemical vapors, humidity variation, solvent swelling, temperature changes, or electric and magnetic fields.[26, 29, 34, 41-49] One example of ink-based rewritable photonic paper used various inks to cause differing degrees of swelling in the polymer matrix, which in turn changed the lattice constant of the embedded photonic crystal to create patterns with different colors.[18-22] The photonic paper is erased by letting the ink

evaporate or washing the paper in a cleansing solution. However, wet-erase procedures are usually cumbersome, and the erasing solutions degrade the rewritable paper over time, limiting their cycle lifetime. The ink itself is volatile and renders these photonic papers unsuitable for long-term information storage.[18, 36] Other types of rewritable photonic paper opted to directly control the erasing step. Photonic crystals formed in a shape memory polymer (SMP) could hold stamped images, fingerprints, or other patterned images, until a heat or water evaporation-based recovery process began.[23-27] This type of photonic paper is good for handwriting, but for printing, methods reliant on stamp printing require complex fabrication processes for every new pattern. Thus, they cannot match the printing speed of traditional paper. For other methods focused on precise pattern display control, electric fields were used to manipulate the lattice constant of photonic crystals, as it is a well understood and easily implemented method. For example, electrophoresis was used to tune full-color pixels made from solvent-suspended photonic crystals.[29-32] By utilizing ionic electroactive polymers (EAPs), photonic polymer matrices can be reversibly swelled to tune colors through redox reactions or hydrogel hysteresis.[34, 37-39, 50] Another type of EAP, dielectric elastomers, can be employed to mechanically compress or stretch a photonic crystal polymer matrix with an applied electric field.[28, 33, 35] However, all electric field-based photonic displays require additional energy input to maintain the written information. So far, no stamp-free photonic paper that is both rewritable and bistable has been developed.

In this work, we report a facile fabrication of reconfigurable and bistable, multi-color, photonic crystals nanocomposite, combining the bistability of shape memory polymers and precise electric control from electroactive polymers. The nanocomposite displays bistable color tuning, and is rewritable without requiring inks, stamps, or a liquid-based recovery process.

Colors are reflected by a ferroferric oxide-carbon (Fe_3O_4@C) core-shell nanoparticle (NP) based photonic crystal embedded in a bistable electroactive polymer (BSEP) matrix (**Figure 2-1**). Electric fields locally actuate areas of the nanocomposite film with Maxwell forces, which creates distinct color contrast (~130 nm) between the actuated and non-actuated sections due to the stopband shift. Any written pattern is maintained permanently by the thermal-responsive shape memory property until a rapid recovery process initiates. This process takes only a few seconds and simply requires exposure to heat above its phase-change temperature. A seven-segment numerical display was also demonstrated to show the ability of displaying user-defined patterns with pixelated electrodes, eliminating the need for stamps that are required in SMP-based displays. Despite significant advances in photonic crystal films from prior research into SMPs and EAPs, this paper is the first to leverage the advantages of each polymer to offset the other's deficiencies in a manner that fully satisfies the demands of a rewritable paper.

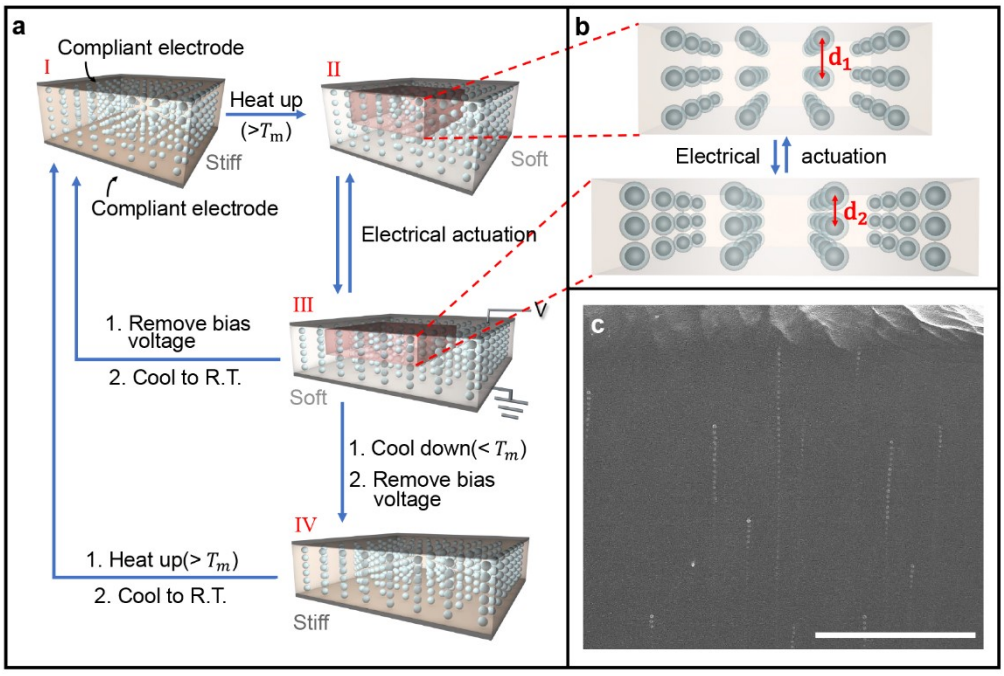

Figure 2-1. **Schematics demonstrating the electroactive and the shape memory properties of a Fe_3O_4@C-BSEP photonic nanocomposite and its writing/erasing mechanism. (a)** The rigid nanocomposite (I) softens upon heating above its phase-changing temperature (II), applied electric field actuates the softened polymer (III), film returns to rigid state when cooled below the phase-change temperature, locking the large applied strain (IV), and the film recovers its original rigid shape (I) by heating above the phase-changing temperature and then cooling back down. **(b)** Enlarged cross sections of the photonic nanocomposite showing the interparticle distance changing during electric field actuation. **(c)** Cross-sectional SEM image of nanochain structures of Fe_3O_4@C nanoparticles in a cured BSEP substrate. The scale bar is 5 μm in length.

2.2 Experimental

2.2.1 Materials

Stearyl acrylate (SA), benzophenone (BP), 2,2-Dimethoxy-2-phentlacetophenone (DMPA) and trimethylolpropane trimethacrylate (TMPTA) were obtained from Sigma-Aldrich. Ferrocene was purchased from Alfa Aesar. Urethane diacrylate (CN9021) was supplied by Startomer. AgNWs with an average diameter of 25-35 nm, length of 15-25 um were provided by Kechuang.

2.2.2 Synthesis of Fe_3O_4@C Core-Shell Nanoparticles

Following the procedure previously reported, with modification:[51, 58] In a typical synthesis, ferrocene (0.27 g) was dissolved in acetone (27 mL) through mechanical stirring for 30 mins, followed by sonication for another 30 mins. Hydrogen peroxide (0.9-1.35 mL) was then

added into the mixture dropwise. The amount of hydrogen peroxide determined the size of synthesized nanoparticles. 0.9-1.35 mL was chosen as to synthesize nanoparticles with desired diameters of (110-160 nm). After 30 mins of sonication and 1 hour of mechanical stirring, the homogenous mixture was transferred to a Teflon-lined stainless-steel autoclave (45 mL). The whole setup was left in an oven at 210 ºC for 30 hrs. After synthesis, the product was washed three times with acetone once the autoclave cooled down to room temperature. The final product was left in the ambient environment to dry.

2.2.3 Fabrication of Fe_3O_4@C-BSEP Photonic Precursors

The BSEP mixture was prepared by mixing SA and UDA oligomers with 40:60 to 80:20 weight ratios. After adding small amounts of BP and DMPA as co-photoinitiators and TMPTA as the crosslinker, the entire SA-UDA mixture was sonicated for 30 mins before use. Fe_3O_4@C powder was added into the SA-UDA mix (4 wt% - 7 wt%), followed by long sonication to form a uniform photonic precursor.

2.2.4 Preparation of Patterned AgNWs Electrodes

Purchased AgNWs were diluted with methanol and isopropanol in a 1:2:4 weight ratio. The AgNW mixture was shaken by vortex for at least 1 hour before use to form a homogenous electrode film. Specially designed masks were taped onto glass slides before spray coating the AgNWs to make the desired electrode shapes. Scotch Magic Tape was used as the mask material, and it was pre-cut by a laser cutter (Epilog Zing Laser). The AgNW mixture was

sprayed coated onto the prepared glass slides with an air gun (Paasche, H0610). After spray coating, the AgNW electrodes were washed once with isopropanol and twice with water.

2.2.5 Fabrication of Fe_3O_4@C-BSEP Rewritable Photonic Films with Patterned Electrodes

Two glass slides were pre-cleaned in acetone and spray coated with patterned AgNW-electrodes through pre-cut Scotch Magic Tape masks. Photonic precursor was then infiltrated in between the two glass slides separated by spacers (90 μm). The infiltrated film was cured under UV light with an external magnet (~2300 G) for 3 min. After curing, the film was peeled off as a freestanding rewritable photonic film.

2.2.6 Characterization

Reflection spectra were taken using an Ocean Optics USB2000 fiber optic vis–NIR spectrometer with a reflection probe (R600–7) and a tungsten halogen light source (LS-1). TEM images were taken using a FEI T12 Quick CryoEM and CryoET microscope. SEM images were taken by a FEI Nova Nano 230 scanning electron microscope. Magnetization of the Fe_3O_4@C nanoparticles was tested by a MPMS3 Superconducting Quantum Interference Device (SQUID) magnetometer. Shape memory cycle test was conducted with a TA Instrument RSA-G2 Solid Analyzer with a temperature sweep rate of 10 ºC min^{-1} and a stretching rate of 0.1 mm s^{-1}. Samples were made to 5 mm in widths and 90 μm in thicknesses. The separation between thin film grips of DMA was set to 4 mm. Other mechanical properties were tested on a TA Instruments RSAIII dynamic mechanical analyzer (DMA). Samples were made to 5 mm in

widths and 90 μm thicknesses. The separation between thin film grips of DMA was set to 5 mm. Dynamic temperature sweep tests were operated at a 2 ºC min^{-1} ramp rate and 1 Hz frequency. The stress-strain cycles and fracture tests were conducted at 50 ºC with a stretching rate of 1 mm s^{-1}. The A high-voltage power supply was built in-house to actuate the Fe_3O_4@C-BSEP nanocomposite films. Resistance measurements for the AgNW electrodes were conducted on a motorized linear stage (Zaber Technologies), measured by a Keithley 2400 digital multimeter, and recorded with a custom LabView code.

2.2.7 Calculation of Effective Refractive Index of Fe_3O_4@C-BSEP Nanocomposites

For a Fe_3O_4@C-BSEP photonic nanocomposite with 3 wt% of Fe_3O_4@C nanoparticles, its effective refractive index can be calculated with

$$n_{eff}^2 = \sum n_i^2 V_i, \qquad \textbf{(1)}$$

which is the volume-weighted average of refractive index for all film components. The refractive indices of Fe_3O_4, C and BSEP are 2.42, 2.4168 and 1.46 respectively. We chose 2.42 as the the average refractive index of Fe_3O_4@C since the values for Fe_3O_4 and C are very close. To find the volume for Fe_3O_4@C, its average density needed to be calculated with **Equation (2)**,

$$\bar{\rho} = \frac{\rho_1 V_1 + \rho_1 V_1}{V}. \qquad \textbf{(2)}$$

The densities of Fe_3O_4 and C are 5.17 g/cm^3 and 2.1 g/cm^3. According to TEM image of 120 nm Fe_3O_4@C nanoparticles, the diameter of the Fe_3O_4 core is 82 nm and the thickness of the C shell is 40 nm, so the effective density of Fe_3O_4@C is:

$$\bar{\rho} = \frac{5.17 \times \frac{4}{3}\pi \times (\frac{82}{2})^3 + 2.1 \times \frac{4}{3}\pi \times [\left(\frac{122}{2}\right)^3 - \left(\frac{82}{2}\right)^3]}{\frac{4}{3}\pi \times (\frac{122}{2})^3}.$$

For a 3 wt% Fe_3O_4@C-BSEP film, we assumed Fe_3O_4 nanoparticles weigh 3 g and the BSEP weighs 97 g. Therefore, the volume of Fe_3O_4 nanoparticles can be calculated as

$$\mathrm{V}_{Fe_3O_4@C} = \frac{m}{\rho} = \frac{3g}{3.03g/cm^3} = 0.99\ mL.$$

The measured density of the BSEP polymer is 0.807 g/cm^3, and the volume of BSEP is calculated the same way:

$$\mathrm{V}_{BSEP} = \frac{m}{\rho} = \frac{97g}{0.807g/cm^3} = 120.2\ mL.$$

Finally, the effective refractive index of the Fe_3O_4@C-BSEP photonic film was determined based on **Equation (1)**:

$$n^2 = 2.42^2 \times \frac{0.99}{0.99 + 120.2} + 1.46^2 \times \frac{120.2}{0.99 + 120.2},$$

$$n_{eff} = 1.47$$

For photonic papers with 4 wt%, 5 wt%, 6 wt% and 7 wt%, their refractive indices as calculated with the same method are:

4 wt% $\quad n_{eff} = 1.474$

5 wt% $\quad n_{eff} = 1.4775$

6 wt% $\quad n_{eff} = 1.48$

7 wt% $n_{eff} = 1.485$

2.2.8 Calculation of Stopbands of Fe_3O_4@C-BSEP with Different NPs Concentrations

According to Bragg's diffraction equation **(Equation (3))**, the stopband of a photonic crystal can be determined with its lattice constant,

$$\lambda = 2n_{eff}Dsin\alpha, \qquad \textbf{(3)}$$

where λ represents peak wavelength of the stopband and D is the lattice constant of the photonic crystal.

For Fe_3O_4@C-BSEP nanocomposites with different concentrations, the calculations for their refractive index can be found in **section 2.2.7**. The average NP-NP distances taken as lattice constants were measured through SEM images. **Table 2-1** shows the average NP-NP distance results for Fe_3O_4@C-BSEP nanocomposites at each concentration. For our actual experimental setup, a factor of sin66º was included to account for the ~66º incident angle of the light source. Taken together, the equation for peak reflected wavelength as calculated from NP-NP distances is:

$$\lambda = 2n_{eff}Dsin\alpha = 2 \times n_{eff} \times sin66° \times D, \textbf{(4)}$$

The calculated λ for each Fe_3O_4@C-BSEP nanocomposite wt% can be found in **Table 2-1**. The experimental results (stopbands measured from reflective specturm) of the nanocomposites with 3 wt%-7 wt% match well with the reflective wavelengths determined from the NP-NP distances provided by the SEM images.

2.3 Results and Discussion

2.3.1 Preparation of Fe_3O_4@C Core-Shell Nanoparticle BSEP Nanocomposite

We chose Fe_3O_4@C core-shell nanoparticles synthesized via ferrocene hydrolysis as the building blocks of the photonic crystals. Compared with other common nanoparticles bases, such as self-assembled polystyrene or silica, Fe_3O_4@C offers both order of magnitude faster assembly time due to its superparamagnetic nature, and better color contrast because of its darker inherent color and large refractive index.[51] Furthermore, the carbon shell helps stabilize the nanoparticles and prevent them from aggregating. By manipulating the size of Fe_3O_4@C nanoparticles and the interparticle distances, we customized the reflected color of the Fe_3O_4@C-BSEP nanocomposite into visible light range. **Figure 2-2** shows the TEM images of Fe_3O_4@C core-shell nanoparticles with different diameters. Out of the 100 nm to 180 nm diameter range for the Fe_3O_4@C core-shell nanoparticles that will create stopbands in the visible light range, the optimal diameters lie within 110 nm to 140 nm. Below 110 nm, the nanoparticles only form ordered structures under powerful magnetic fields, and they preferentially reflect blue light. Above 160 nm, the large size limits the approach of the nanoparticles as they come into contact, constricting their reflected color to red.[52]

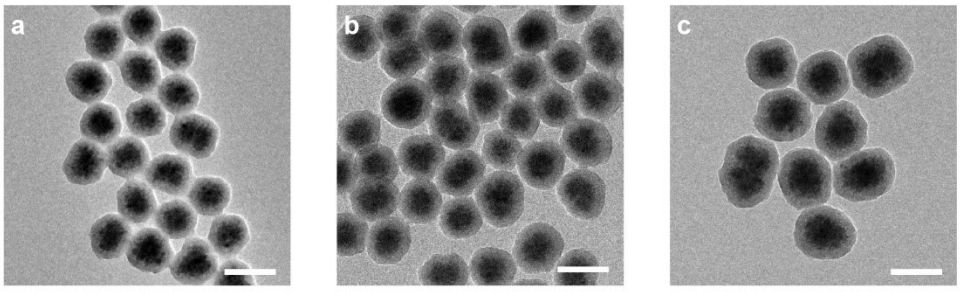

Figure 2-2. TEM images of Fe_3O_4@C core-shell nanoparticles with diameters of **(a)** 120nm, **(b)** 140nm and **(c)** 160nm. The scale bars are 150 nm in length.

The BSEP that forms the polymer matrix is a photocured copolymer that consists of stearyl acrylate (SA) and urethane diacrylate (UDA) in weight ratios of 40:60 to 80:20. The phase-change temperature (T_m) of the BSEP varies from 30 ºC to 45 ºC depending on the composition. The electroactive, shape memory properties and crystallinity of SA-UDA copolymers have been described elsewhere.[53] For demonstration purposes, we used a SA-UDA copolymer with a 60:40 weight ratio (BS60) throughout this work for its high stretchability and good fixing ratio. **Figure 2-3** provides the structures of each components within BSEP and a schematic network structure of cured BSEP.

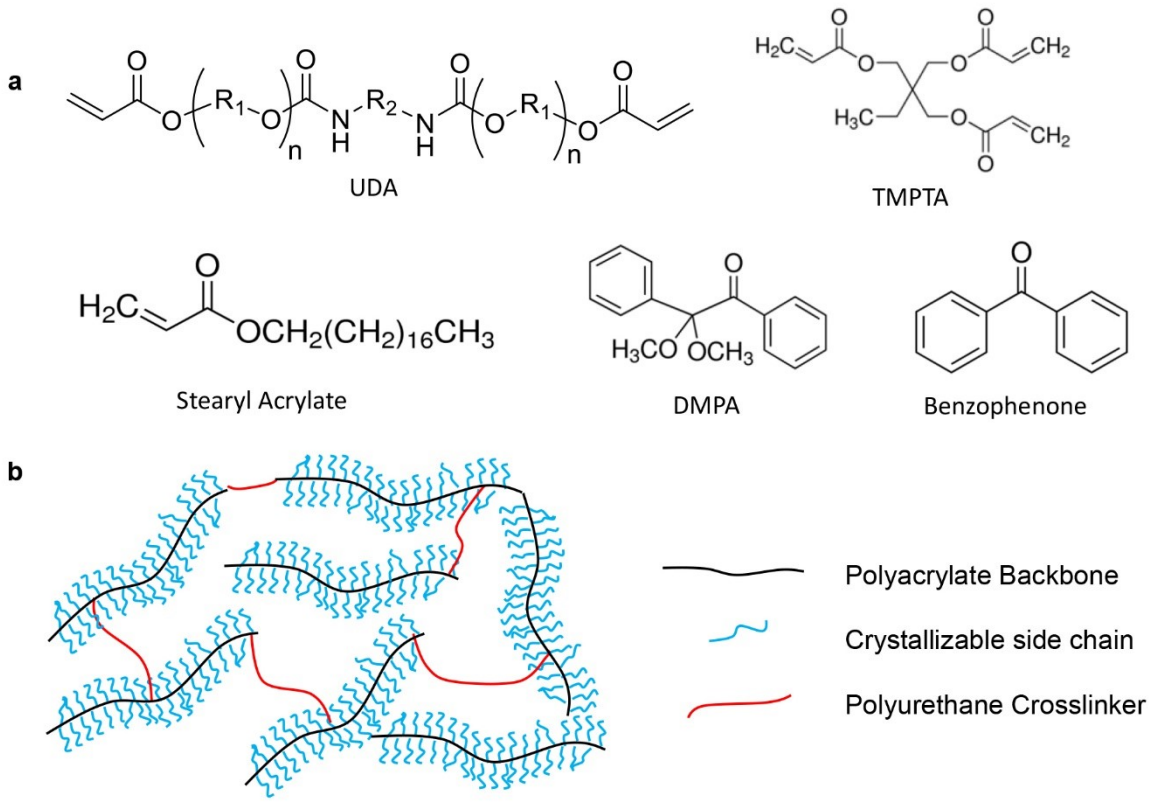

Figure 2-3. (**a**) Chemical structures of each components of BSEP. (**b**) Schematic illustration of crosslined BSEP network.

To create the nanocomposite, SA and UDA co-monomers were first mixed with a crosslinker and a photo-initiator. Then, prepared Fe_3O_4@C powder was homogenously mixed in to create a thick slurry photonic precursor. A film of photonic slurry is then exposed to a magnetic field, which aligns the superparamagnetic Fe_3O_4@C nanoparticles into nanochain structures. The magnetic field induces a dipolar magnetic attractive force to counter the electrostatic repulsive force between the nanoparticles. A stronger magnetic field induces a stronger interparticle attractive force, decreasing the lattice constant and blue shifting the reflected spectrum. **Figure 2-4** confirms the magnetization of Fe_3O_4@C nanoparticles at room temperature under external magnetic field. The photonic slurry is then UV cured while under a persistent external magnetic field (~2300 G). While the photonic film exhibited a brilliant purple color before curing, it red-shifted during the curing process. After curing, the photonic crystal chains were immobilized within the polymer matrix, fixing the nanoparticle alignment, interparticle distance, and stopband. After fixation, external magnetic fields no longer significantly alter the reflection color, so the final reflected color after cure is determined by the size and concentration of Fe_3O_4@C nanoparticles. An SEM image of Fe_3O_4@C nanochain structures in cured BSEP substrate is shown in **Figure 2-1(c)**.

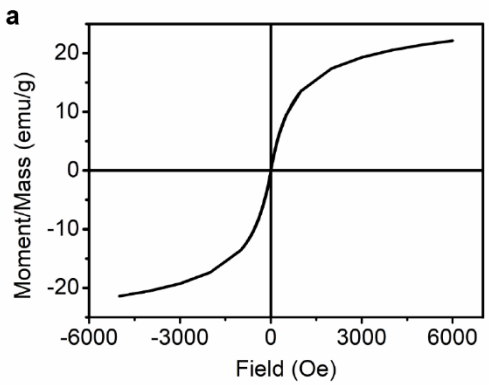

Figure 2-4. **(a)** Magnetization curve of Fe_3O_4@C nanoparticles powder at room temperature.

2.3.2 Nanoparticle Concentration Effect on Film Initial Color

To accommodate for the blueshift in reflectance during the actuation of the photonic nanocomposite, we experimented with different concentrations of Fe_3O_4@C nanoparticles in the precursor to achieve the optimal initial reflected color that lies on the lower energy end of the visible light range. We started with Fe_3O_4@C-monomer precursor slurries with nanoparticle concentrations of 3 wt% to 7 wt%, which all appeared purple when exposed to a magnetic field of ~2300 G. Though most of the samples redshifted to some degree during curing, those with higher concentrations redshifted further after curing, as shown in **Figure 2-5(a)**.

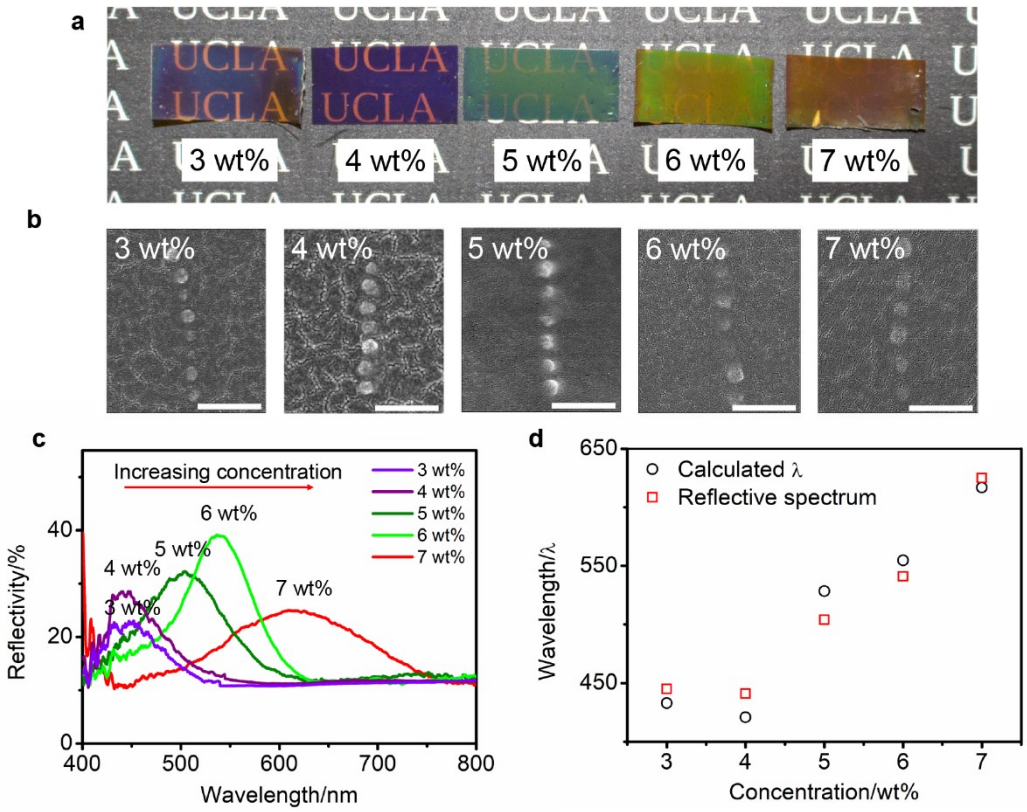

Figure 2-5. **BSEP-Fe_3O_4@C photonic nanocomposite films with increasing nanoparticle concentrations. (a)** Optical images of the photonic nanocomposites showing red shift in base reflected color. **(b)** Cross-sectional SEM images of the Fe_3O_4@C nanochains in the BSEP matrix. Interparticle distance increased with increasnig Fe_3O_4@C weight fraction. All the scale bars are 500 nm in length. **(c)** Reflective spectra at each concentration. **(d)** Peak wavelength of the stopbands as a function of the concentration of nanoparticles. Black circles are calculated values based on Bragg's diffraction equation using the NP-NP distances meansured by SEM. Calculation details can be found in **section 2.2.7** and **2.2.8**. Red square values were directly meansured by the reflective photospectrometer.

The lattice constant increase may have resulted from the stronger repulsive forces between nanochains, given that the higher NP concentration puts them in greater proximity.

Specifically, applying a magnetic field before UV-cure induces a dipole-dipole interaction between individual nanoparticles. For any two nanoparticles, the force generated between them is described by **Equation (3)**:

$$F = 3\mu^2(1-3cos2\theta)/d^4, \qquad \textbf{(5)}$$

where μ is the effective magnetic moment of a given nanoparticle, θ is the angle between the magnetic field vector and the line intersecting the centers of both nanoparticles, and d is the interparticle distance. While $\theta < 54.09^o$, the force between two nanoparticles is attractive. Whereas when $54.09^o < \theta < 90^o$, the force is negative.[54] When dispersed in monomers, the nanoparticles chains are balanced between the repulsive force from surface charges and the attractive force induced by magnetic field. As the curing process shrinks the film laterally, the nanochains are brought closer together. For a low nanoparticle concentration film, the nanochains are still far away to influence each other. But with a higher nanoparticle concentration, a closer interchain distance will result in an extra dipole-dipole repulsive interaction between adjacent chains. Since there is no space for nanochains to move in xy-directions, they will push away nanoparticles from adjacent chains along z direction, and thus lead to an increase in the lattice constant and red shift in the color.

The SEM images (**Figure 2-5(b)**) confirm the increment in NP-NP separation along the magnetic field within each nanochain (i.e. the increase in lattice constant), and the reflective spectra (**Figure 2-5(c)**) demonstrates the stopband red shift as nanoparticle concentration exceeds 4 wt%. The same pattern occurs for Fe_3O_4@C nanoparticles embedded in a different polymer system (PEGDA), as shown in **Figure 2-6**, which suggests that this phenomenon is not a special interaction or chance.

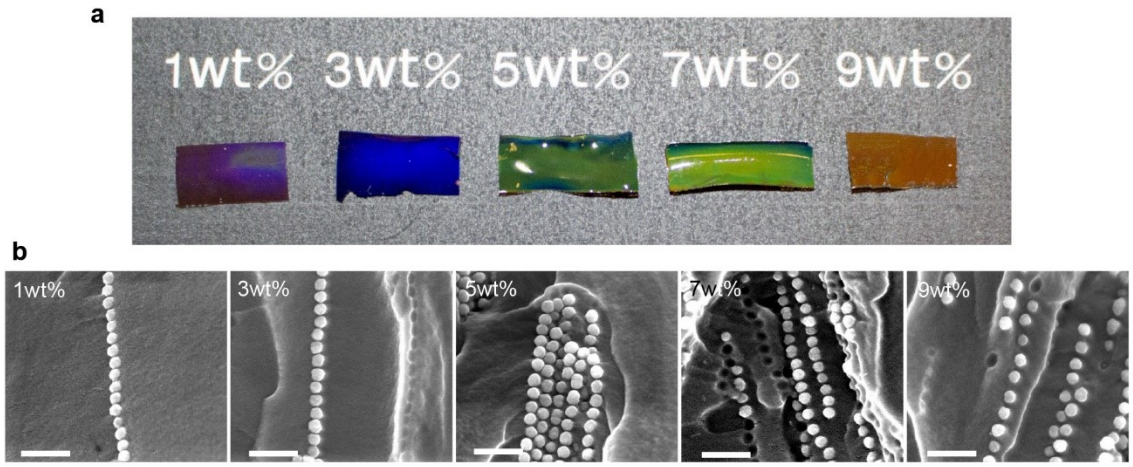

Figure 2-6. **Fe_3O_4@C-PEG nanocomposites with increasing nanoparticle concentrations.** (**a**) Optical images of the nanocomposites showing red shift in reflection color. (**b**) Cross-sectional SEM images showing Fe_3O_4@C nanochains in the PEG matrix. Interparticles distance is increased with Fe_3O_4@C weight fraction. The scale bars are 500 nm in length.

Table 2-1 contains the NP-NP distances as measured from the SEM images for each sample concentration. The calculated stopbands of these Fe_3O_4@C-BSEP nanocomposites films were derived from Bragg's diffraction equation **Equation (4)**:

$$\lambda = 2\, n_{eff} D \sin\alpha, \qquad \textbf{(6)}$$

where λ is the peak wavelength of the stopband, D represents the measured lattice constant of the photonic crystal, and n_{eff} is volume-weighted average refractive index for the whole film. The Fe_3O_4@C nanoparticles used in this series of Fe_3O_4@C-BSEP nanocomposites had a core diameter of 82 nm and a C shell thickness of 44 nm measured from TEM images. The calculation of n_{eff} for each Fe_3O_4@C-BSEP nanocomposite can be found in the **section 2.2.7**. As shown in **Figure 2-5(d)**, the calculated stopbands (black circles) of this series of films match

well with the experimental data measured directly from the reflective spectra (red squares). More calculation details can be found in the **section 2.2.8**.

Table 2-1. Interparticle distances (D determined from SEM images), refractive index (n), calculated peak wavelengths of stopbands (λ) and measured reflective wavelengths (λ, by reflective spectrum) for Fe_3O_4@C-BSEP nanocomposites with different nanoparticle concentrations (C).

C [wt%]	D [nm]	n	Calculated λ [nm]	Measured λ [nm]
3	161.8	1.47	434.5	445
4	156.3	1.474	420.9	401
5	195.8	1.4775	528.5	504
6	204.1	1.48	551.8	541
7	227.4	1.485	616.9	625

Ultimately, based on the reflective spectra results, nanoparticle concentrations between 5 wt% and 7 wt% produced the best finalized films with the desired initial red-green range of color.

2.3.3 Mechanical Properties Characterization

Based on previous research, we expected the BSEP to fit the desired mechanical property profile for a photonic paper, but we needed to verify its properties and understand what changes result from adding in the NPs.[53] For this purpose, we compared BSEP with 0 wt% NPs and BSEP with 7 wt% NPs, the highest NP density used in our paper. The evaluation of our

thermally activated BSEP are divided into three major categories: properties of the low temperature state, properties of the high temperature state, and properties of the transition.

In the low temperature state, the BSEP must be rigid enough to store information in the form of deformation until reactivated by heat. At low temperatures, both 0 wt% and 7 wt% have elastic moduli on the order of 10^2 MPa, more than rigid enough to endure external stimuli (**Figure 2-7(a)**). In the high temperature state, the BSEP needs a low young's modulus to lower the force requirements needed for electric field actuation. Both samples had a rubbery modulus on the order of 10^{-1} MPa; the 7 wt% film's rubbery modulus was slightly lower likely due to the reduced crosslinking density. The increase in mechanical loss factor (**Figure 2-7(b)**) for 7 wt% Fe_3O_4@C-BSEP nanocomposite compared to pure BSEP after phase transition further supports a lower crosslinking density. The increase in viscoelasticity is best explained by the weakened resilience force due to the reduced number of crosslinked bonds between the long UDA chains and dispersed nanoparticles blocking film recovery. This agrees with previously reported studies where composite networks with higher nanoparticle concentrations had lower crosslinking densities, as evidenced by a higher degree of swelling in solvent.[55]

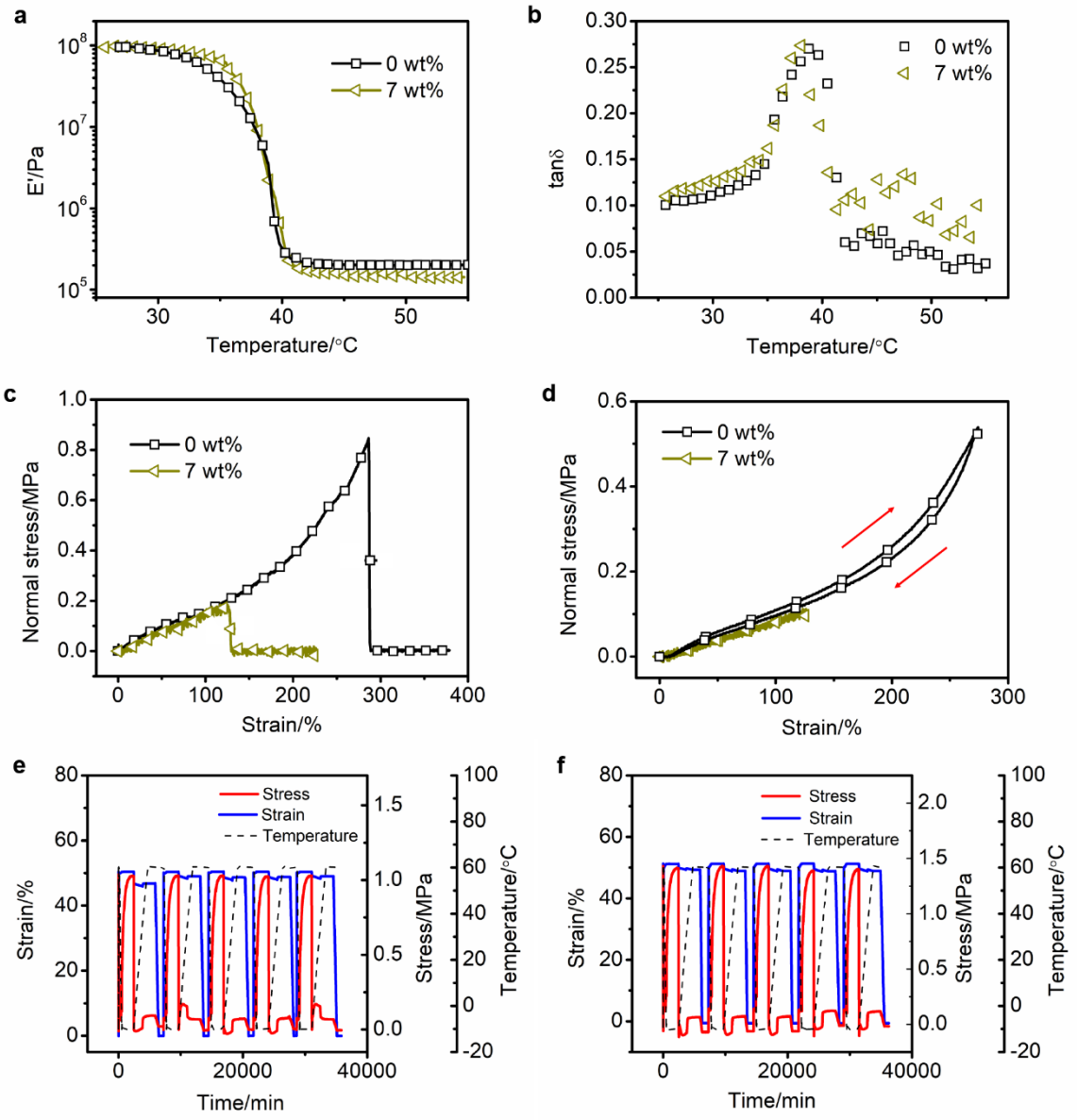

Figure 2-7. **Mechanical properties of a 7 wt% BSEP-Fe_3O_4@C photonic nanocomposite compared to pure BSEP**. **(a)** Storage modulus (E') as a function of temperature showing a glass transition temperature of ~38 ºC for both 7 wt% nanocomposite and pure BSEP. **(b)** Loss factor of both 7 wt% nanocomposite and pure BSEP as a function of temperature. **(c)** Tensile stress-strain curves. Frature strain is 125% for the 7 wt% nanocomposite and 286% for the pure BSEP. **(d)** A tensile loading-unloading cycle for the pure BSEP polymer and 7 wt% nanocomposites. **(e)** Shape memory cycle test for pure BSEP polymer. **(f)** Shape memory cycle test for 7 wt% nanocomposite.

Furthermore, the film needs high elasticity above the transition temperature so that localized deformation doesn't cause fracture at the border between actuated and non-actuated sections. The 7 wt% sample experienced a significantly lower fracture elongation rate at 125% compared to 286% for pure BSEP, potentially from nanoparticles impeding the extension of the long, entangled, UDA chains (**Figure 2-7(c)**). Furthermore, the non-uniform nanochain distribution amplifies their inherent stress concentration behavior, which contributes to the decrease in elongation at break as well. However, 50% strain is sufficient to achieve a distinct stopband shift, which leaves a large margin before failure.

The transition region must also conform to the intended use. The transition temperature must be low enough for a conventional or household appliance to achieve quickly and inexpensively while high enough that ambient temperatures won't erase it. The transition temperature measured from the dynamic mechanical analyzer (DMA) was 38 ºC, as tested with a 2 ºC min^{-1} ramp rate (**Figure 2-7(a)**). The temperature is well within the range reasonably achievable with cheap localized heating. In addition, **Figure 2-7(d)** shows a cyclic tensile loading-unloading test for the pure SA-UDA polymer and 7 wt% Fe_3O_4@C-BSEP nanocomposite. Both polymers show great elastic properties dictated by tiny hysteresis loops, which helps reduce recovery time and energy loss compared to viscoelastic materials.

For shape memory properties, the fixing ratio and recovery ratio of both pure SA-UDA polymer and 7 wt% Fe_3O_4@C-BSEP nanocomposite were tested through DMA as shown in **Figure 2-7(e)(f)**. Based on the averaged data of 5 cycles, the fixing ratio and recovery ratio of pure SA-UDA polymer are 96.1% and 100%; whereas the fixing ratio and recovery ratio of 7

wt% Fe_3O_4@C-BSEP nanocomposite are 96.6% and 100%, showing no obvious influence of nanoparticles to the mechanical properties of the polymer matrix.

2.3.4 Shape Memory Property Characterization and Color Change

Color contrast and color persistence are the two key parameters for evaluating Fe_3O_4@C-BSEP nanocomposite color tuning properties. Change in reflected spectra is a function of deformation of the lattice matrix, so we opted to characterize the stopband shift with a tensile load test. A sample film with a 10 mm x 6 mm active area was kept at 50 °C, well above the transition temperature to soft state, and stretched along a single axis (x-axis) to a maximum 100% strain with nanoparticle chains embedded along the z-axis. Strain along the x-axis induces compression along the z-axis, reducing the interparticle distance within the nanochains. The film was then cooled in the air with load to maintain the deformation and color change. Measurements of the reflected spectra and interparticle distances were taken at 25% strain intervals from 0% strain to 100% strain. 50% strain along the x-axis lead to a color change from red to green as seen in **Figure 2-8(a)**, corresponding to a 177 nm stopband shift (**Figure 2-8(c)**). After stretching the sample to 75% strain, the color changed into a dark green, and further strain induced only slight darkening in the sample. At 100% strain, the stopband shifted a maximum 276 nm.

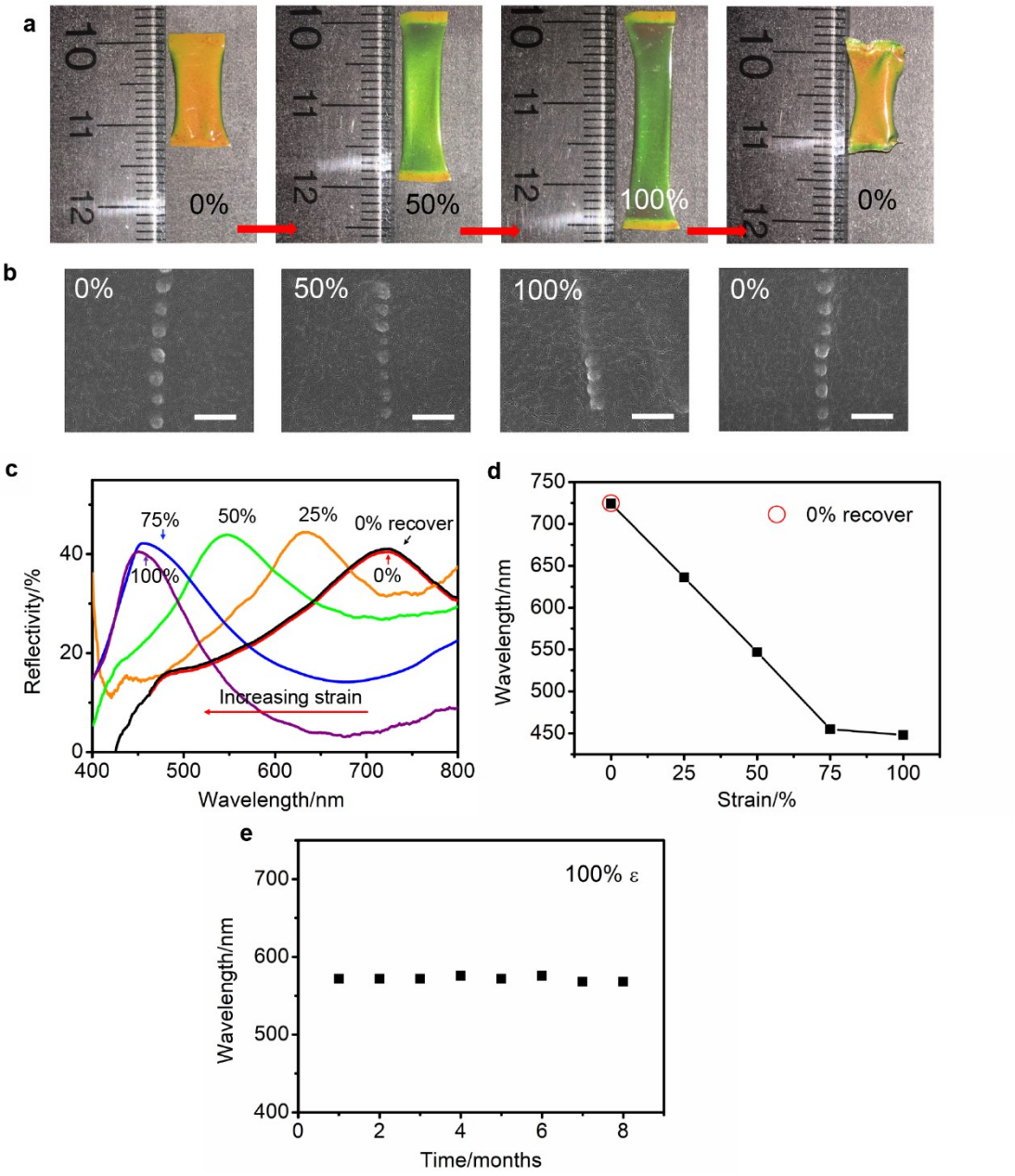

Fig 2-8. **Shape memory property of the photonic nanocomposite containing 6 wt% Fe_3O_4@C nanoparticles. (a)** Optical images of the a red photonic nanocomposite at 0%, 50%, and 100% tensile strains. Note that all of the films are free-standing and rigid at room temperature. The rightmost image is the recovered shape of the the nanocomposite film after 100% strain. **(b)** Cross-sectional SEM images of the same photonic nanocomposite at 0%, 50% and 100% tensile strains. Interparticle distance decreases with increasing film strain. All the scale bars are 500 nm in length. Reflective spectra **(c)** and peak

reflective wavelengths **(d)** of this photonic nanocomposite as a function of tensile strain. "0% recover" data points in both figures indicate the complete recovery of the photonic film after 100% strain. **(e)** Peak reflective wavelengths of a 100% strained photonic nanocomposite measured over an eight-month span.

SEM images in **Figure 2-8(b)** and **Figure 2-9** show the change in interparticle distance of the Fe_3O_4@C-BSEP film at different tensile strain (ε) states. Data measurements for the interparticle distances (D) and their corresponding strains (ε_z) are shown in **Table 2-2**. We measured 281.9 nm as the initial Fe_3O_4@C interparticle distance at 0% tensile strain based on the SEM images. Using this initial distance as the baseline and assuming a Poisson ratio of 0.5 which is typically observed for rubbery elastomers, we calculated the theoretical interparticle distances as a function of tensile strain. As shown in **Table 2-2**, the theoretical values match well with the measured distances until 75% tensile strain. At 100% tensile strain, the theoretical distance is smaller than the measured distance. In the nanocomposite, the minimum interparticle distance is constrained by the rigid nanoparticles contacting each other. The measured reflective wavelengths (λ) confirm the physical limit on compression, as there is a negligible change in wavelength between 75% and 100% strain (**Figure 2-8(c)**, **Table 2-2**). The calculated reflective wavelengths derived from Bragg's diffraction equation and the measured Fe_3O_4@C interparticle distances are consistent with the measured reflectance data at each strain level. The large stop-band shift creates a distinct color contrast between the stretched and unstretched film, which is easily noticeable to human eyes.

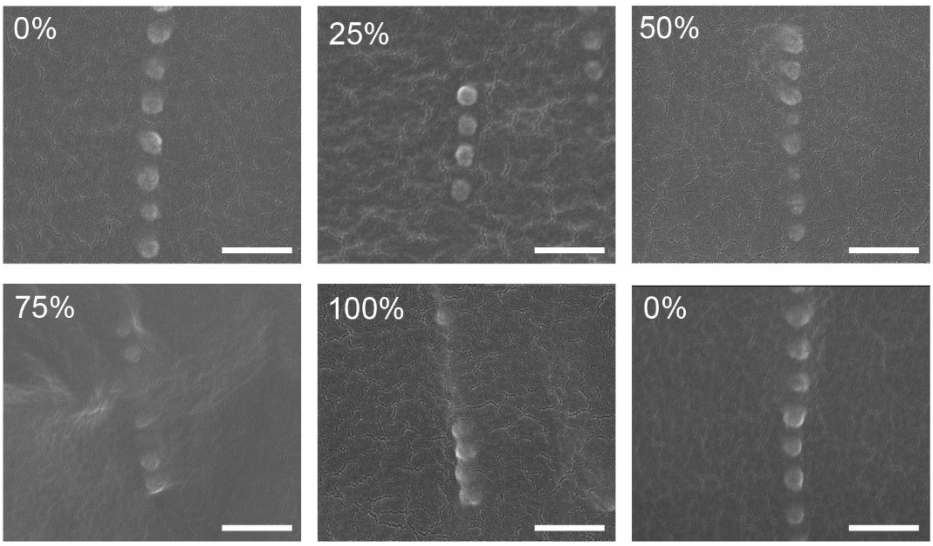

Figure 2-9. **SEM images of Fe_3O_4@C chains within BSEPs with different tensile strain levels.** Fe_3O_4@C interparticle distances are shown in **Table 2-2**. The scale bars are 500 nm in length.

Table 2-2. Theoretical (ε_Z^*) and actual (ε_Z) thickness strains, theoretical (D*) and measured (D) Fe_3O_4@C interparticle distances, calculated (λ*) and measured (λ) reflective wavelengths of Fe_3O_4@C-BSEP nanocomposites with different tensile strains (ε). ε_Z^* is calculated from ε, using 0.5 as Poisson ratio; D is measured from the SEM images shown in **Figure 2-9**; ε_Z^* is calculated according to D; D* is calculated using ε_Z^*, and use 281.9 nm as the initial Fe_3O_4@C interparticle distance with 0% tensile strain; λ* is measured from reflective spectrum; λ* is calculated according to the actual interparticle distances from D, 1.48 and 60º are used as refractive index and incident light angle respectively, based on previous calculation in this supporting information. For the 100% tensile strain sample, D is smaller than D* because of the physical impedence after two nanoparticle touched, and the measured reflective wavelength result λ is consistant with D.

ε [%]	ε_Z^* [%]	ε_Z [%]	D* [nm]	D [nm]	λ* [nm]	λ [nm]
0	0	0	281.9	281.9	722.6	724.05
25	12.5	12.3	246.7	247.3	633.9	636.2
50	25	24.7	212.4	212.2	543.9	547
75	37.5	37.4	176.2	176.53	452.5	445
100	50	38.7	141	172.7	442.7	448
0 recover	0	0	281.9	282	722.89	724.72

In addition to pattern clarity, pattern persistence is also a critical parameter for practical applications of this nanocomposite. We tested pattern permanence by exposing a 100% strained photonic film to ambient temperature and measuring its reflectance every week. The peak reflectance wavelength data in **Figure 2-8(e)** shows that the 100% strained film retains its color without noticeable variation for over a year (figure represents an 8-month segment). By raising the temperature above T_m and releasing the stress on the sample, it recovers to its original state, which is also verified by the near identical reflective spectra in **Figures 2-8(c) and 2-8(d)**.

2.3.5 Electroactive Properties Characterization

The Fe_3O_4@C-BSEP photonic nanocomposite has both electroactive and shape memory properties due to the nature of the SA-UDA copolymer. **Figure 2-1(a)** demonstrates the working principle of this Fe_3O_4@C-BSEP nanocomposite film with compliant electrodes on each face. The rigid photonic film softens after it is heated above its T_m , at which point the photonic film is responsive to external electric fields. Under an electric field, charges along the same electrode

surface repel each other, but they attract the charges from the opposite electrode surfaces, causing the film to expand in-plane but shrink in the z direction. Thus, the interparticle distance shortens, as shown in **Figure 2-1(b)**. This dimensional change blue-shifts the stopband, which in turn changes the color the photonic paper reflects. To prevent buckling as the nanocomposite film actuates, the film is biaxially pre-stretched by 15% strain in each direction using a custom two-dimensional frame before applying the electric field.[56] As the film cooled below T_m under a maintained electric field, the deformation and blueshifted color became permanent. Below T_m, the photonic paper no longer requires the electric field to display color. Heating the film above T_m recovers its original shape and coloration.

An important step in building the electroactive photonic nanocomposite is ensuring that the electrodes that induce actuation can survive the stresses applied by the polymer as it expands and contracts. For this purpose, we chose transparent silver nanowire (AgNW) electrodes for their visible light transparency and mechanical compliancy. We fabricated Fe_3O_4@C-BSEP composite pixel samples with patterned AgNW electrodes along the top and bottom surfaces of the film, as explained in **Figure 2-10**. Details for the electrode fabrication can be found in the Methods section. To test the stretchability of the transparent AgNW-BSEP composite electrodes, sheet resistance of samples with 15 Ω sq^{-1} (active area: 5 mm x 5 mm) were prepared. Samples were heated to 45 °C and subjected to a tensile strain test of either increasing uniaxial strain (ε_x) to 100% or increasing biaxial strain (ε_A) to 70% (**Figures 2-11(a) and (b)**). **Figure 2-11(c)** shows transient resistances of the AgNW-BSEP composite electrode under 10 cycles of stretching-releasing between 0% and 10%, 0% and 20%, 0% and 30%, 0% and 40%, 0% and 50% strains in succession with a stretching speed of 1 mm s^{-1}. The initial strain leads to a permanent increase in resistance, with higher strains leading to larger initial jumps. However,

resistance does not significantly increase in the subsequent cycles, staying with a new bounded region. The strain dependent permanent increase in resistance is likely due to the irreversible breaking and sliding of AgNWs in the mesh electrodes during the stretching process. As the sample entered the 0%-50% stage, both peak and base resistances increased slightly as it cycled, which may have related to the BSEP viscoelasticity.

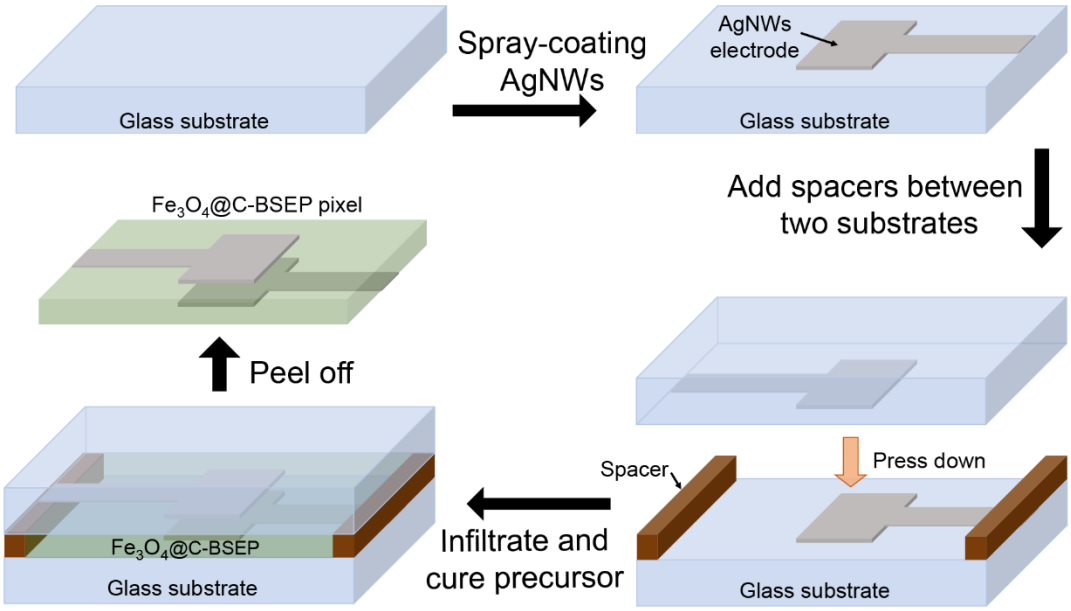

Figure 2-10. A schematic illustration for the fabrication process of Fe_3O_4@C-BSEP nanocomposite pixel sample with patterned AgNWs electrodes.

The planar strain test places significantly more stress on the sample than can be accommodated by AgNW slip, so we expect greater changes in resistivity in the AgNW-BSEP composite electrodes. As shown in **Figure 2-11(b)**, the resistance increases steadily while remaining within the kΩ range until 45% area strain, after which the sheet resistance rapidly increases into the MΩs. The SEM images in **Figure 2-12** verify the breakdown of AgNWs when

the AgNW-BSEP film stretches to 50% strain. Given the high voltage, low current actuation mechanism of our BSEP, the composite film would still function with transient resistance at several MΩ . For our sample, we achieved maximum color tuning with at most 40% area strain (including pre-strain), and the sheet resistance still remained below 3 kΩ.

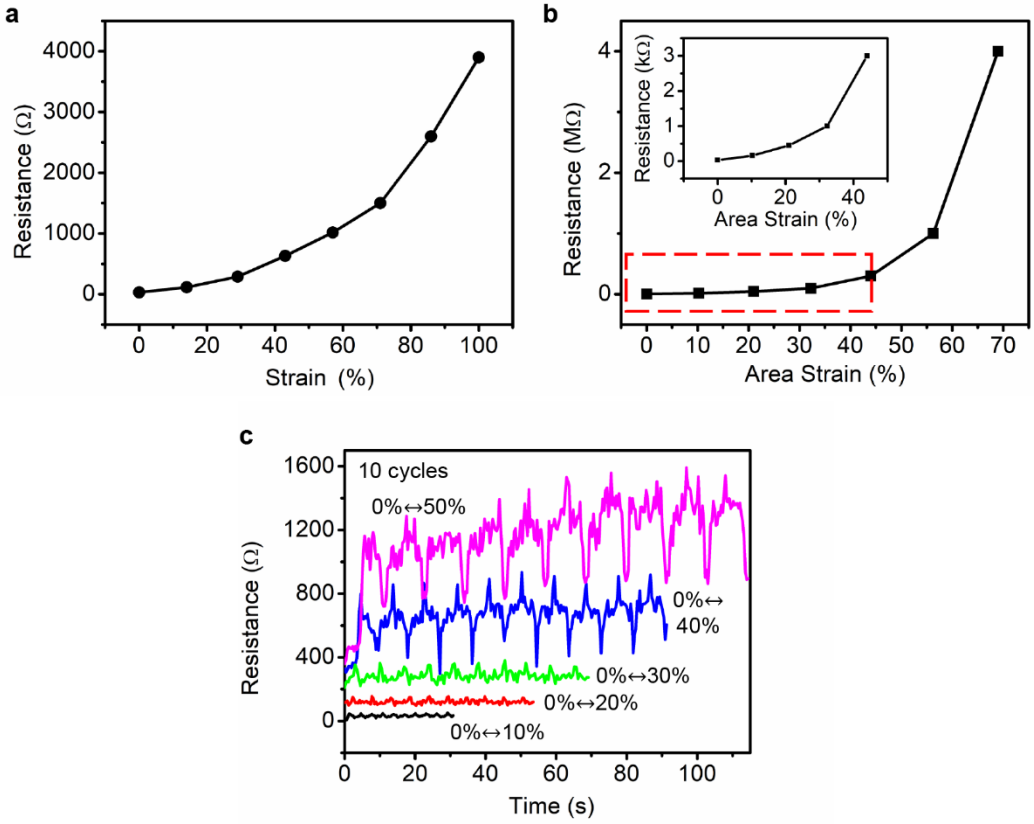

Figure 2-11. Sheet resistance of a AgNW-BSEP composite electrode (active area 5 mm x 5 mm) with increasing **(a)** uni-axial tensile strain, and **(b)** bi-axial area strain. The **inset in (b)** enlarges the sheet resistance change from 0%-45% area strain, as indicated by the red dashed square. **(c)** Transient resistances measured during 10 cycles of sequentially stretching–relaxing for a 15 Ω sq^{-1} AgNW–BSEP composite electrode between 0% and 10%, 0% and 20%, 0% and 30%, 0% and 40%, 0% and 50% strains (sample size: 5×5 mm^2; stretch speed: 1 mm s^{-1}, sample was at 45 ºC when measured).

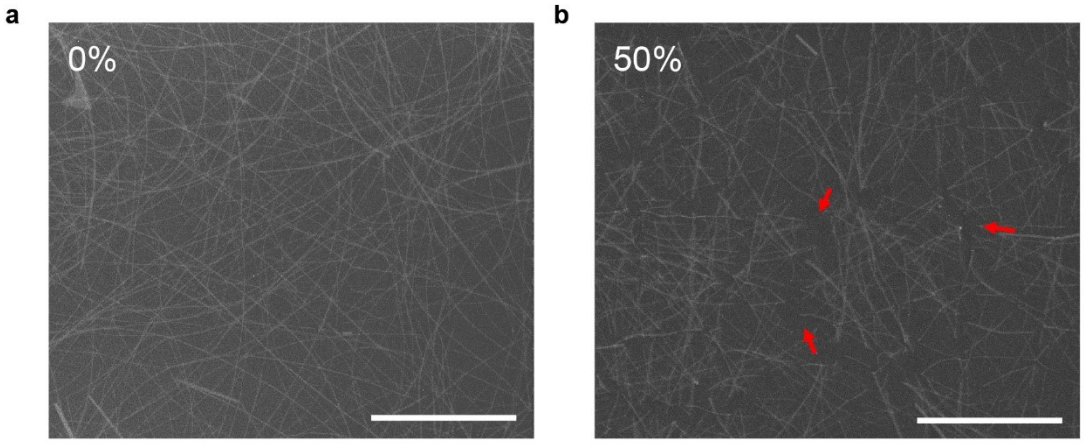

Figure 2-12. **(a)**, **(b)** TEM images of a AgNW-BSEP composite electrode with no strain and 50% area strain. Red arrows indicate the areas where AgNWs broke.

Now that we had an electrode capable of surviving the stresses exerted by the substrate, we tested the electroactive property of the Fe_3O_4@C-BSEP nanocomposite with a smaller inset 5 mm x 5 mm electrode area acting as a single photonic pixel with a red initial color. We began by varying the strength of the electric field from 16.7 kV m^{-1} to 26.7 kV m^{-1} in 1.1 kV m^{-1} increments with an additional baseline measurement without any electric field, shown in **Figure 2-13(a)**. Comparing the stopband against the electric field, **Figure 2-13(b)** reveals an inverse linear relationship, which matches well with theoretical values for the stopband, shown by red circles, that were derived from the measured strains. Details for the calculation can be found in **Table 2-3**.

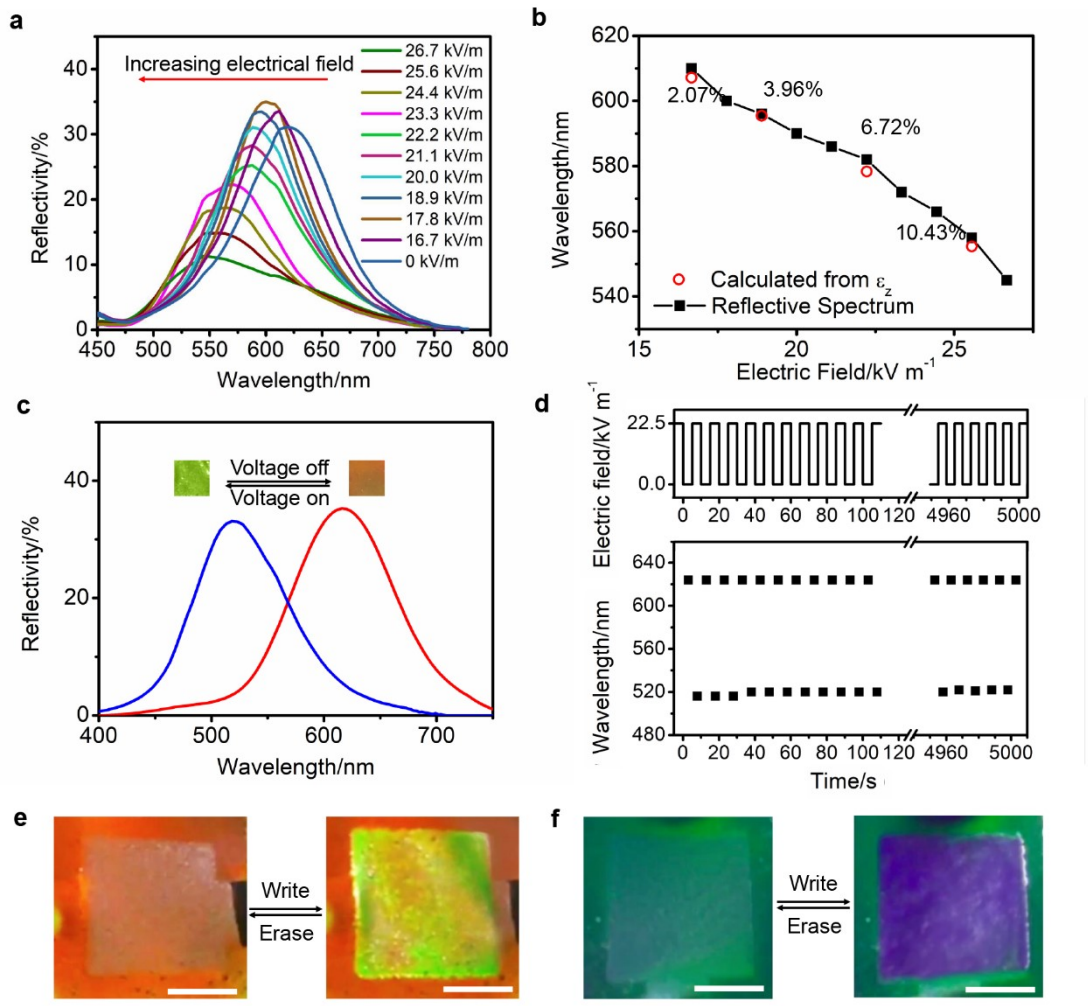

Fig 2-13. Electrical actuation of the photonic nanocomposite pixel above transition temperature. (a) Reflective spectra with incremental increase in applied electric field. **(b)** Peak reflective wavelengths as a function of electric field. Red open circles are stopbands calculated from thickness strains of the film, which are shown next to the circles. Calculation procedure can be found in **Table 2-3**. **(c)** Reversible writing and erasing of a red photonic nanocomposite pixel by switching the 22.5 kV m^{-1} electrical field on and off. **(d)** Peak reflective wavelength across 500 writing and erasing cycles following a square wave signal operating between 0 and 22.5 kV m^{-1}. **(e), (f)** Written and erased states of photonic nanocomposite pixels switching between **(e)** red and green colors, and **(f)** green and purple colors under electric field

actuation. The color-changing area is the "active area" where the AgNW electrodes on top and bottom surfaces overlap. The scale bars are 3mm in length.

Table 2-3. Calculated strains along x-direction (ε_x) and thickness direction (ε_z), calculated (λ*) and measured (λ) reflective wavelength of Fe_3O_4@C-BSEP nanocomposites with different electric field E. ε_x were measured from video snapchats that were recorded perpendicular to the surface of the film. Assuming the film is incompressible, and the lengths of the Fe_3O_4@C-BSEP pixel along x-direction and y-direction are the same, then ε_z can be calculated from the following equation:

$$1 = (1 + \varepsilon_x)(1 + \varepsilon_x)(1 + \varepsilon_z). \quad \textbf{(6)}$$

The initial reflective color of the unactuated film is 620nm as indicated by the reflected spectrum for **Figure 2-13(a)**. Then the predicted stopband change (Δλ) of the film can be calculated by the Bragg's law:

$$\Delta\lambda = 2\sin\theta, \quad \textbf{(7)}$$

Where Δd is the interparticle distance difference under various electric fields. Thus, the change in stopband is proportional to thickness strain (ε_z) of the film:

$$\Delta\lambda \propto \varepsilon_z.$$

The results of predicted stopbands of the film are shown in **Figure 2-13(b)**, which are consistent with the results measured from reflective spectrophotometer.

E[kV/m]	ε_x[%]	ε_z[%]	λ*[nm]	λ[nm]
16.7	1.05	2.07	610	610
18.9	2.04	3.96	597.4	596

22.2	3.54	6.72	585.8	586
25.6	5.66	10.43	570.8	572

Figure 2-13(c) demonstrates the writing and erasing processes of the single photonic pixel. After applying an electric field of 22.5 kV m^{-1}, the photonic pixel expanded in-plane, generating a 108 nm stopband shift from 624 nm to 516 nm. The heated film reverted from green to red once the electric field was switched off. **Figure 2-13(e)** is a visual comparison between the on and off states of the photonic pixel. The square grey area on the film is the partial discoloration by the upper AgNW electrode, as the film is otherwise uniformly red. Since the applied electric field is localized, only the middle square area of the film expanded. There was a clear color change from red to green with significant color contrast between the red background and the green written pixel. Both the activation and recovery times of the pixel measured around 0.8 s. **Figure 2-13(f)** is a similar photonic pixel but with a green initial color due to a different Fe_3O_4@C nanoparticle size and concentration. After electrical actuation, the area of the film between the patterned AgNWs electrodes switched from green to purple, generating a similarly distinct color change between the two states.

The Fe_3O_4@C-BSEP nanocomposite was tested for durability by cycling it under an electric field following a square wave signal operating between 0 and 22.5 kV m^{-1}. Reflective wavelength was measured 3 s after each change in electric field to leave time for the film to equilibrate. Across 500 periods, cycling produced no appreciable change in color fidelity or film integrity, as shown in **Figure 2-13(d)**.

2.3.6 Bistable Electroactive Photonic Paper

With patterned electrodes, we built a basic rewritable photonic paper demonstrating the strengths of Fe_3O_4@C-BSEP nanocomposite in color contrast and ease of operation. For conventional paper, the exhibited information cannot be changed once printed. And for SMP-based photonic paper, cumbersome fabrication of new stamps is needed to demonstrate different patterns. But for our rewritable paper, with pixelated electrode matrix, any desired patterns can be displayed by selectively actuating electrode pixels. And this photonic film can be refreshed with new patterns by selecting different electrode pixels to actuate. As a demonstration, we fabricated a 7-segemented numerical display. Details about the electrode preparation and photonic paper fabrication can be found in the Methods section. After curing and heating it above its transition temperature, the photonic paper was green in the absence of an applied electric field. By applying a 30 kV m^{-1} electric field to specific segments of the electrode, it displayed the digits 0 to 9 in purple color against the green background, as seen in **Figure 2-14(a)**. The photonic paper maintained the digits without the aid of the electric field once brought below T_m, and bringing the film above the T_m erased it completely. When placed in contact with a 65 ºC hot plate, the photonic paper fully recovered within a second. Recovery at more practical temperatures, e.g. 40 ºC, remains below 8 seconds.

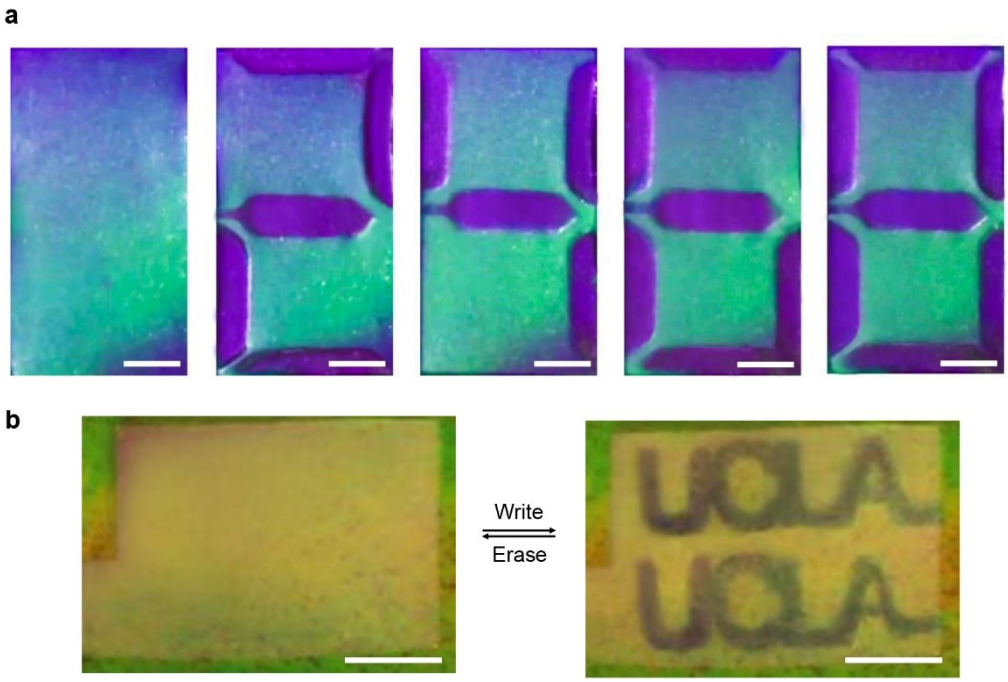

Fig 2-14. **Demonstration of rewritable photonic papers. (a)** Selected images of a photonic paper sequentially demonstrating digits 0-9. **(b)** Writing and erasing a "UCLA" pattern with font size of 10 on a photonic paper. The scale bars are all 3mm in length.

Another key parameter for the practical application of this new photonic paper is achieving a comparable resolution to conventional paper. A "UCLA" pattern in Calibri font size 10 was used as a sample to evaluate resolution limits of the photonic film. To prepare the film, a "UCLA"-shaped electrode with a feature size of 300 μm was transferred onto the back side of a photonic paper. Once actuated by an electric field, the "UCLA" pattern showed up clearly, as demonstrated in **Figure 2-14(b)**. The size of the electrode defines the resolution of the photonic paper, which for our work was limited by the minimum feature size of the spray coating mask prepared by laser cutter. However, screen printing techniques can create arrays of electrode pixels with feature sizes of ~50 μm, comparable to current paper printing resolution.[57]

2.4 Conclusion

In conclusion, we have described a new rewritable photonic nanocomposite derived from Fe_3O_4@C core-shell nanoparticles embedded in a SA-UDA based bistable electroactive polymer. It is a durable information storage medium that can retain messages indefinitely without energy input, and its high color contrast and high resolution guarantee enduring legibility. It is erased through a simple heating mechanism, which can be adjusted to avoid accidental activation. The nanocomposite is rewritable across several hundred cycles without noticeable degradation. Finally, the electric field writing mechanism opens many practical applications where modern technology can easily control the nanocomposite. In our work, 7 segmented electrodes were designed to display digits; while with electrode pixel arrays, images can be created as desired. Given this material's strengths, it shows promise in replacing information displays with long demonstration times but low refresh frequencies, such as billboards and tags. In future studies, we seek to improve the polymer matrix with the aim of targeting full-color range photonic paper.

2.5 Reference

[1] *United States Environmental Protection Agency* **2015**.

[2] B. K. Ince, Z. Cetecioglu, O. Ince, in *Environmental Management in Practice*, InTech **2011**.

[3] B. Comiskey, J. Albert, H. Yoshizawa, J. Jacobson, *Nature* **1998**, 394, 253.

[4] B.-R. Yang, L. Wang, Y.-C. Wang, J. Qiu, G. Liu, S. Deng, presented at SID Symposium Digest of Technical Papers **2017**.

[5] L. Wang, G. S. Liu, Y. C. Wang, J. Su, X. D. Wang, X. Zeng, Z. S. Zhang, S. Z. Deng, H. P. D. Shieh, B. R. Yang, *Journal of the Society for Information Display* **2017**, 25, 384.

[6] M. Wang, Y. Li, H. Du, X. Zhang, H. Gu, R. Ivanov, R. Sprague, Google Patents, 2016.

[7] X. Wang, H. Zang, P. Li, presented at SID Symposium Digest of Technical Papers **2006**.

[8] P. F. Bai, R. A. Hayes, M. Jin, L. Shui, Z. C. Yi, L. Wang, X. Zhang, G. Zhou, *Progress In Electromagnetics Research* **2014**, 147, 95.

[9] Y. Deng, B. Tang, A. V. Henzen, G. G. Zhou, presented at SID Symposium Digest of Technical Papers **2017**.

[10] Y. K. Fung, D. K. Yang, J. W. Doane, presented at High-Resolution Displays and Projection Systems **1992**.

[11] J. W. Doane, D.-K. Yang, L.-C. Chien, Google Patents, 2000.

[12] M. Lightfoot, E. N. Montbach, D. Marhefka, A. A. Khan, Google Patents, 2018.

[13] E. N. Montbach, C. I. Braganza, M. Echeverri, D. Marhefka, D. J. Davis, F. Nicholson, A. Khan, presented at SID Symposium Digest of Technical Papers **2017**.

[14] J. Wei, X. Jiao, T. Wang, D. Chen, *ACS Appl Mater Interfaces* **2016**, 8, 29713.

[15] L. Sheng, M. Li, S. Zhu, H. Li, G. Xi, Y. G. Li, Y. Wang, Q. Li, S. Liang, K. Zhong, S. X. Zhang, *Nat Commun* **2014**, 5, 3044.

[16] W. Wang, J. Feng, Y. Ye, F. Lyu, Y. S. Liu, J. Guo, Y. Yin, *Nano Lett* **2017**, 17, 755.

[17] W. Wang, N. Xie, L. He, Y. Yin, *Nat Commun* **2014**, 5, 5459.

[18] J. Ge, J. Goebl, L. He, Z. Lu, Y. Yin, *Advanced Materials* **2009**, 21, 4259.

[19] H. Fudouzi, Y. Xia, *Langmuir* **2003**, 19, 9653.

[20] P. Jiang, D. W. Smith, J. M. Ballato, S. H. Foulger, *Advanced Materials* **2005**, 17, 179.

[21] M. Moirangthem, A. F. Scheers, A. Schenning, *Chem Commun (Camb)* **2018**, 54, 4425.

[22] H. Wan, X. Li, L. Zhang, X. Li, P. Liu, Z. Jiang, Z. Z. Yu, *ACS Appl Mater Interfaces* **2018**, 10, 5918.

[23] Y. Fang, Y. Ni, S. Y. Leo, B. Wang, V. Basile, C. Taylor, P. Jiang, *ACS Appl Mater Interfaces* **2015**, 7, 23650.

[24] Y. Fang, S. Y. Leo, Y. Ni, J. Wang, B. Wang, L. Yu, Z. Dong, Y. Dai, V. Basile, C. Taylor, P. Jiang, *ACS Appl Mater Interfaces* **2017**, 9, 5457.

[25] S. Y. Leo, W. Zhang, Y. Zhang, Y. Ni, H. Jiang, C. Jones, P. Jiang, V. Basile, C. Taylor, *Small* **2018**, 14, e1703515.

[26] Y. Fang, Y. Ni, B. Choi, S. Y. Leo, J. Gao, B. Ge, C. Taylor, V. Basile, P. Jiang, *Adv Mater* **2015**, 27, 3696.

[27] Y. Fang, Y. Ni, S. Y. Leo, C. Taylor, V. Basile, P. Jiang, *Nat Commun* **2015**, 6, 7416.

[28] J. Xia, Y. Ying, S. H. Foulger, *Advanced Materials* **2005**, 17, 2463.

[29] I. Lee, D. Kim, J. Kal, H. Baek, D. Kwak, D. Go, E. Kim, C. Kang, J. Chung, Y. Jang, *Advanced Materials* **2010**, 22, 4973.

[30] K. H. Ko, E. Park, H. Lee, W. Lee, *ACS Appl Mater Interfaces* **2018**, 10, 11776.

[31] T. S. Shim, S. H. Kim, J. Y. Sim, J. M. Lim, S. M. Yang, *Adv Mater* **2010**, 22, 4494.

[32] H. S. Yang, J. Jang, B. S. Lee, T. H. Kang, J. J. Park, W. R. Yu, *Langmuir* **2017**, 33, 9057.

[33] Z. H. Fang, C. Punckt, E. Y. Leung, H. C. Schniepp, I. A. Aksay, *Applied optics* **2010**, 49, 6689.

[34] A. C. Arsenault, D. P. Puzzo, I. Manners, G. A. Ozin, *Nature Photonics* **2007**, 1, 468.

[35] T. Yin, D. Zhong, J. Liu, X. Liu, H. Yu, S. Qu, *Soft Matter* **2018**, 14, 1120.

[36] H. Fudouzi, Y. Xia, *Advanced Materials* **2003**, 15, 892.

[37] K. Hwang, D. Kwak, C. Kang, D. Kim, Y. Ahn, Y. Kang, *Angew Chem Int Ed Engl* **2011**, 50, 6311.

[38] Y. Lu, C. Meng, H. Xia, G. Zhang, C. Wu, *Journal of Materials Chemistry C* **2013**, 1, 6107.

[39] T. J. Park, S. K. Hwang, S. Park, S. H. Cho, T. H. Park, B. Jeong, H. S. Kang, D. Y. Ryu, J. Huh, E. L. Thomas, *ACS nano* **2015**, 9, 12158.

[40] H. Kim, J. Ge, J. Kim, S.-e. Choi, H. Lee, H. Lee, W. Park, Y. Yin, S. Kwon, *Nature Photonics* **2009**, 3, 534.

[41] I. B. Burgess, L. Mishchenko, B. D. Hatton, M. Kolle, M. Loncar, J. Aizenberg, *Journal of the American Chemical Society* **2011**, 133, 12430.

[42] P. K. Kundu, D. Samanta, R. Leizrowice, B. Margulis, H. Zhao, M. Borner, T. Udayabhaskararao, D. Manna, R. Klajn, *Nat Chem* **2015**, 7, 646.

[43] X. Du, T. Li, L. Li, Z. Zhang, T. Wu, *Journal of Materials Chemistry C* **2015**, 3, 3542.

[44] M. M. Hawkeye, M. J. Brett, *Advanced Functional Materials* **2011**, 21, 3652.

[45] B. Viel, T. Ruhl, G. P. Hellmann, *Chemistry of Materials* **2007**, 19, 5673.

[46] H. Hu, C. Chen, Q. Chen, *Journal of Materials Chemistry C* **2013**, 1, 6013.

[47] H. Li, J. Wang, L. Yang, Y. Song, *Advanced functional materials* **2008**, 18, 3258.

[48] Y. Takeoka, M. Watanabe, *Langmuir* **2003**, 19, 9104.

[49] K. Yoshino, Y. Shimoda, Y. Kawagishi, K. Nakayama, M. Ozaki, *Applied Physics Letters* **1999**, 75, 932.

[50] A. Seyfoddin, A. Chan, W. T. Chen, I. D. Rupenthal, G. I. Waterhouse, D. Svirskis, *Eur J Pharm Biopharm* **2015**, 94, 419.

[51] H. Wang, Y.-B. Sun, Q.-W. Chen, Y.-F. Yu, K. Cheng, *Dalton Transactions* **2010**, 39, 9565.

[52] J. Ge, Y. Hu, Y. Yin, *Angewandte Chemie* **2007**, 119, 7572.

[53] Z. Ren, W. Hu, C. Liu, S. Li, X. Niu, Q. Pei, *Macromolecules* **2015**, 49, 134.

[54] L. He, Y. Hu, H. Kim, J. Ge, S. Kwon, Y. Yin, *Nano Letters* **2010**, 10, 4708.

[55] C. M. Yakacki, N. S. Satarkar, K. Gall, R. Likos, J. Z. Hilt, *Journal of applied polymer science* **2009**, 112, 3166.

[56] R. Pelrine, R. Kornbluh, Q. Pei, J. Joseph, *Science* **2000**, 287, 836.

[57] J. Liang, K. Tong, Q. Pei, *Advanced Materials* **2016**, 28, 5986.

[58] J. Zhang, A. Sun, X. Qiao, C. Chu, C. Wang, T. Chen, J. Guo, G. Xu, *Materials Research Express* **2014**, 1, 045037.

Chapter 3

A Phase-Changing Polymer Film for Broadband Smart Windows Applications

3.1 Introduction

The global issues of climate change and the rapidly escalating energy consumption have inspired developments in the efficiency of energy usage. These global issues have been identified by the United Nations (UN) as an increasing danger in the improvement of life.[1] American Physical Society states that by reducing the 40% of energy used in residential and commercial buildings from air conditioning and heating could potentially reduce 30% of the total United States' carbon emissions.[2-3] Utilizing smart windows' tunable opacity to control both the timing and amount of light transmission would have a direct reduction in the overall demand for air conditioning and heating. Through regulation of solar-irradiation into buildings and residences the potential to save 1% of the annual total energy consumption in United States would make smart windows a must-have for zero-emission buildings.[4-5] Furthermore, smart windows can also be deployed in business and household rooms to improve privacy protection.[6] Three

different technologies have been developed for smart windows: photochromic, electrochromic and thermochromic technologies.[4, 7-20] Currently available photochromic, electrochromic, and thermochromic smart window materials have limited bandwidth modulation, have short lifetimes, and/or must undergo complex production methods.[21-27]

Photochromic materials, such as tungsten bronze (M_xWO_3), noble metals (Ag, Au), semiconductor oxides (ITO, AZO), etc., change color under sunlight or UV irradiation due to localized surface plasma resonance (LSPR).[7-11] Photochromic-based smart windows can be operated with narrow light frequency switching, but this is not a desirable feature. This absorbance mechanism hinders a wide-range bandwidth switch that covers the whole spectrum from UV to near infrared (NIR) light.[21-22] Moreover, the absorption at a certain wavelength range usually results in a fixed color for dark or transparent states of the smart windows, which is undesirable for general applications.[7]

Electrochromic smart windows utilize the insertion and extraction of electrons in electrochemical redox reactions of the host materials to change colors.[11-14] The switching speed depends on the active device area, diffusion length, and coefficient of electrolyte ions. The switching time of large-area electrochromic windows can take up to 10 minutes for practical usage.[10] Attempts have been made to integrate dye-sensitized solar cell units within the electrochromic windows to enhance their switching speed, as well as to reduce the energy consumption from external electricity supplies.[10] However, electrochromic windows overall share the same issue with photochromic windows in that they have fixed colorations at either the transparent state, dark state, or both.[14] More critically, electrochromic windows have complicated structures, limited cycle lifetime, and excessive sealant due to the use of liquid electrolytes.[23]

Thermochromic smart windows, on the other hand, started to gain interest due to their simple fabrication, adaptability to electrically controlled devices, and inexpensive nature. Traditional VO_2-based smart windows can change colors due to a metal-insulator transition at critical temperatures, but these materials have low transmittance at visible light range for the transparent state, low oxidation resistance, and high cost for fabrication.[24-26] More recently explored thermochromic smart windows are made of hydrogels, ionic liquids, and liquid crystals which utilize solution-based processes to simplify the fabrication, and can help with increasing the transparency at visible light range for the transparent state of smart windows.[4, 15-20] Hydrogel-based thermochromic smart windows take advantage of hydrogels' phase separation property to enable a wide modulation wavelength range and high transmittance modulation contrast.[4, 15-18] When heated above its low critical solution temperature (LCST), the polymer chains of hydrogels separate out from water to form polymer-rich and water-rich domains, which will cause the transition from a transparent state to an opaque state. However, the inclusion of water in a hydrogel-based thermochromic smart window hinders the cyclic stability due to water evaporation. In response to the thermal instability of hydrogels, ionic gels were introduced as a replacement, but the introduction of ions may still degrade the polymer matrix over time.[28] Thermochromic polymer-dispersed or polymer-stabilized liquid crystals are favored for smart window applications because of their fast switching speed when adapted with electrical controls, large transmittance modulation contrast, and adaptability to roll-to-toll manufacturing.[19-20] Although liquid crystals have become attractive as a smart window material, they suffer from having a limited bandwidth due to their fixed pitches.[27] Cholesteric liquid crystals or stacked liquid crystals with various pitches were used to enable large bandwidth switching, but they are expensive for large area applications in buildings.[20, 29-30]

Solution-processed UV curable polymer smart windows are attractive to manufacture due to their simple fabrication methods. The inclusion of water or solvents in the final device should also be avoided for high cycle life and thermal stability. Here we introduce a new wide bandwidth thermochromic smart window (SW) material based on a phase change polymer that can be reversibly switched between an opaque semicrystalline state and a transparent amorphous state. The SW film consists of a crosslinked network of this phase changing polymer and poly(ethylene oxide) oligomer with highly different hydrophilia. The transmittance switching property of the SW film is the combination of three different mechanisms, which are detailed in **section 3.3.1**: (1) phase separation between the two distinct constituent polymers, (2) a large change of refractive index, and (3) opacity of the phase-changing polymer during the amorphous-to-semicrystalline transition. Micro-sized surface patterns generated from the two-polymer phase separation help increase the overall opacity of SW film at the opaque state for the whole solar spectrum. The two constituent polymers share the same refractive index at the transparent state which enables high transmittance, but upon cooling stearyl acrylate's (SA) refractive index changes rendering the film opaque. The reversible phase transition of the phase changing polymer provides the repeatability of the transparent-to-opaque transition of the SW film. This reported solution processed fabrication procedure delivers a faster and simpler way to construct smart windows. The final all-solid SW film also has a long cycle lifetime when compared to hydrogels due to no water evaporating problem. A silver nanowire (AgNW) based transparent heater was combined with the SW film to control the amorphous-to-semicrystalline transition more easily. The final smart window application can achieve a large luminous transmittance modulation (ΔT_{lum}) of 80.41% and solar transmittance modulation (ΔT_{solar}) of 70.16%. In this paper, we will introduce the switching mechanism of the SW films, the

characterization of AgNW heater, and a smart window application. To our knowledge, this work is the first one to report an all-solid thermochromic smart window film without the inclusion of any metal/metal oxides or liquid crystals to enable a large light modulation over the whole solar spectrum.

3.2 Experimental

3.2.1 Materials

Stearyl acrylate (SA), 2,2-Dimethoxy-2-phentlacetophenone (DMPA) and trimethylolpropane trimethacrylate (TMPTA) were purchased from Sigma-Aldrich. Ethoxylated trimethylolpropane triacrylate (ETPTA), polyurethane acrylate (CN9009), difunctional acrylic monomer (SR306) were supplied by Sartomer. AgNWs with an average diameter of 25-35 nm, length of 15-25 um were provided by Kechuang.

3.2.2 Fabrication of Smart Window (SW) films

Stearyl acrylate and SR415 were mixed with ratio 1:1 to 6:1, then 1 wt% of DMPA was added in as photo-initiator. The whole mixture was dissolved in 25-30 wt% acetone to render a clear solution, followed with thorough sonication. The film was fabricated by injecting the clear solution between two glass slides separated by spacers (170 μm), and then cured under UV light for 3 mins. After curing, the film was peeled off as a freestanding SW film with thickness around 150 μm due to the evaporation of acetone.

3.2.3 Fabrication of AgNW/PUA Composite Heaters

PUA polymer precursor was prepared by mixing CN9009 and SR306 with a ratio 5:1, 1 wt% of DMPA was then added. Ultrasonication was applied to get a uniform mixture. The transparent and flexible heater was fabricated in two steps. Firstly, a dispersion of AgNWs in isopropanol (~2 mg ml^{-1} concentration) was coated on a pre-cleaned glass slide with Meyer bar (RD Specialist). Secondly, another pre-cleaned glass slide was applied on top of the conductive coating with spacers. The thickness of the spacers can be chosen from 50 μm to 170 μm, which can decide the thickness of the resultant AgNW/PUA composite heater. PUA polymer precursor was then injected in between the two glass slides, followed by UV curing for 3 minutes. Then the AgNW/PUA film can be peeled off as a free-standing composite heater.

3.2.4 Fabrication of Smart Window Devices

The smart window devices consist of lamination of three layers: top PUA film with thickness of 70 μm, middle SW film with thickness of 150 μm and bottom AgNW/PUA composite heater with 70 μm in thickness. The top PUA film can be fabricated using the same process as the fabrication of AgNW/PUA composite heaters but eliminating the AgNWs coating step. The top PUA layer was designed to be smaller than the bottom AgNW/PUA layer by 1 cm in only one dimension to allow the exposure of the conductive embedded AgNWs. The stacked structure was then laminated by a hot press machine several times with temperature below 40 °C to ensure a good sealing. Aluminum foil stripes were fixed to both sides of the exposed AgNWs. Silver paste were applied between aluminum foil and AgNW/PUA film to establish solid pathways for electrons.

3.2.5 Characterization

Transmittance spectrum was taken using a Shimadzu UC-3101PC UV-Vis-NIR spectrophotometer with tungsten halogen and deuterium lamps. SEM images were taken by a FEI Nova Nano 230 scanning electron microscope. Optical microscope images were obtained from a Zeiss microscope. Cyclic bending tests were performed on a motorized linear stage with built-in controller (Zaber Technologies Inc.). Mechanical properties were tested on a TA Instruments RSAIII dynamic mechanical analyzer (DMA). Samples were made to 3 mm in widths and 70 μm in thicknesses. The separation between thin film grips of DMA was set to 5 mm. Dynamic temperature sweep tests were operated at a 2 °C min^{-1} ramp rate and 1 Hz frequency. Transition temperature of SW film was measured with a PerkinElmer differential scanning calorimeter (DSC 8000) at a ramping rate of 15 °C min^{-1}. The heating performance of the AgNW/PUA heater was tested with a DC power voltage supplier (Agilent E3612A). The temperature of the AgNW/PUA heater was measured by an infrared camera (ICI 9320P). Contact angles of films were detected with an APPR telescope-goniometer. And refractive indices of films were measured by a Metricon refractometer (2010/M). Film X-ray diffraction data was obtained using a Panalytical X'Pert Pro X-ray diffractometer with Cu Kα radiation.

3.3 Results and Discussion

3.3.1 Preparation and Characterization of Smart Window Film

The SW film is prepared from a mixture of two acrylate compounds. For the phase changing component, SA is selected due to its sharp and reversible crystalline-to-amorphous transition with a melting temperature (T_m) around 32-34 ℃. Cured poly(stearyl acrylate) film has a melting temperature around 49.3 ℃ as determined by the differential scanning calorimetry result (see **Figure 3-1(a)**). This temperature is sufficiently high for the polymer film to stay stable at the semicrystalline (opaque) state under an ambient environment, and a modest temperature increase could transform it into an amorphous (transparent) state. However, neat poly(SA) film is not visually opaque enough at its semicrystalline state. The parallel transmittance of a 170 μm neat poly(SA) film at a semicrystalline state ranges from 11% to 36.8% in the visible range, and rises rapidly at longer wavelengths (**Figure 3-2**). Based on the full width at half max (FWHM) of the wide-angle X-ray diffraction (XRD) of the neat poly(SA) film (**Figure 3-1(b)**) and the Schererr equation, the crystal size of the poly(SA) aggregate is calculated to be 3.53-4.36 nm ($2\theta \approx 21°$), which is much smaller than visible light wavelength. Rayleigh scattering is thus expected to be the dominating factor for the diminished light transmission, which is proportional to λ^{-4}. As the result, the parallel transmittance is low in the deep blue and high in the red and infrared regions. The opposite trend is observed for the diffusive transmittance spectrum.

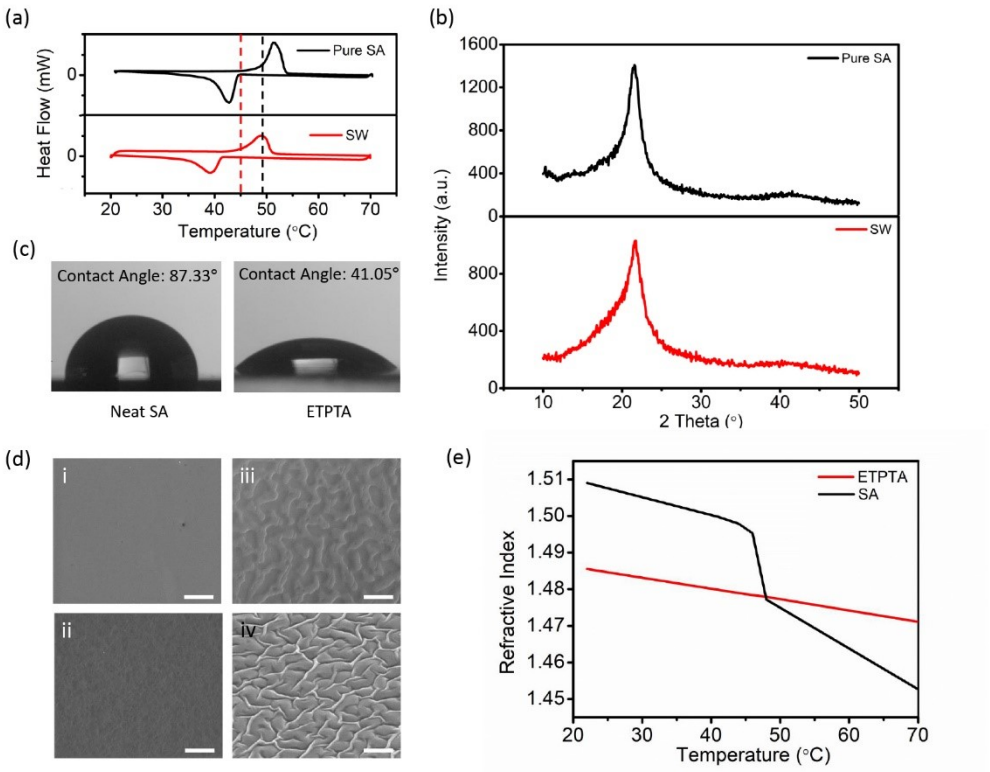

Figure 3-1. Comparison between neat SA and SW films. (a) Differential scanning calorimetry results showing a shift of melting temperature of SW film to lower degree. **(b)** X-Ray Diffraction results for both SA and SW films. **(c)** Contact angles of both neat SA film and neat ETPTA film. **(d)** SEM images of neat SA film and SW film. As-prepared (i) neat SA film and (iii) SW film, (ii) neat SA film and (iv) SW film after one cycle of heating above T_m and then cooled to below Tm. The film surface in image iv was tilted with 45° to give a better view of the patterns. All scale bars represent 10 μm. **(e)** Refractive indices of both pure ETPTA film and neat SA film as a function of temperature.

To increase the wide bandwidth opacity of the poly(SA) film, Mie scattering needs to be introduced: the scattering of light by particles larger than the light's wavelength is relatively wavelength independent. Thus, a second tri-functional acrylate was introduced in the SA system. This tri-functional acrylate, ethoxylated trimethylolpropane triacrylate (ETPTA), also serves as a

crosslinker to enhance the toughness of the SW film, since the SA film itself is very brittle. The poly(ethylene oxide) segments on ETPTA provides good water wettability; while the long alkyl chains on SA affords a hydrophobic property. According to the contact angle experiments as shown in **Figure 3-1(c)**, ETPTA ($\theta \approx 41.05°$) and SA ($\theta \approx 87.33°$) have a large difference in hydrophilia. When these two components are mixed together with an optimized ratio, the resultant film will generate a rough surface with micro-sized patterns due to phase separation, and these micro-sized patterns can help diffract the whole solar spectrum.

The weight ratio of SA and ETPTA was optimized to be between 6:1 to 4:1. In this work, the ratio of 6:1 was used due to the high opacity of SW film at opaque state. Higher concentration of ETPTA will hinder the crystallization of SA moieties, and thus affect the opacity of the film at the opaque state; while lower concentration will result in a brittle film, which is undesired for practical applications. The SA and ETPTA monomers do not dissolve into each other; the as-cured SA-ETPTA mixture films had a coarse surface with large phase separations visible to the naked eyes. Acetone was added as a solvent to co-dissolve SA and ETPTA which confined the phase separation to the micron scale. The optimal concentration of acetone is around 25%, which affords a clear liquid solution. The clear solution was cast into thin films of 150 μm thickness after cured under UV light. The remaining acetone was evaporated during the curing process, and the co-polymerization of SA and ETPTA caused phase separation. However, the domain size is constrained thanks to the copolymerization and crosslinking between SA and ETPTA chains. The resulting crosslinked copolymer films (SW films) have a visibly smooth surface.

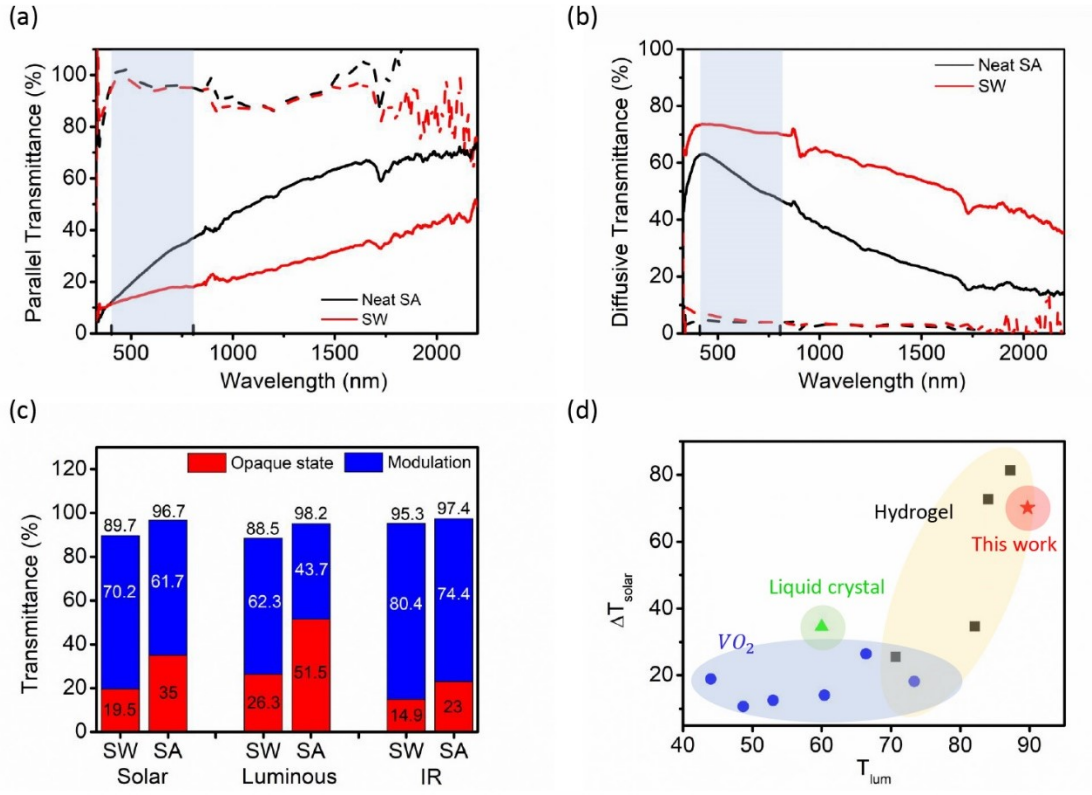

Figure 3-2. Transmittance spectrum of both neat SA and SW films. (a) Parallel transmittance spectrum for both pure SA and SW films. **(b)** Diffusive transmittance spectrum for both films. Dotted lines show transmittance of both films at transparent status. Solid lines represent transmittance of both films at opaque status. The blue shaded areas represent visible light range from 400 nm to 800 nm. **(c)** Solar, luminous and IR transmittance comparison between SW and neat SA films. **(d)** Transmittance modulation performance (Luminous Transmittance, T_{lum}, at transparent state) for some of the best reported thermochromic smart windows: hydrogel films, VO_2 based films, liquid crystals hybrid films. Adapted and reproduced with permission from Ref. 4. Copyright 2019, Elsevier Inc.; Ref. 15. Copyright 2018, WILEY-VCH; Ref. 19. Copyright 2017, American Chemical Society; Ref. 31. Copyright 2015, The Royal Society of Chemistry; Ref. 32. Copyright 2014, The Royal Society of Chemistry; Ref. 33. Copyright 2014, The Royal Society of Chemistry; Ref. 34. Copyright 2013, the Owner Societies; Ref. 35. Copyright 2017, The Royal Society of Chemistry and the Centre National de la Recherche Scientifique;

Ref. 36. Copyright 2014, The Royal Society of Chemistry; Ref. 37. Copyright 2017, Elsevier B.V; Ref. 38. Copyright 2016, American Chemical Society.

Scanning Electron Microscopy (SEM) reveals the micrometer-size phase separation patterns as shown in **Figure 3-1(d)**. Both neat SA film and SW film SEM images were captured in their pristine states, and in semicrystalline states after being heated and cooled once. According to the DSC result for the mixed film of SA and ETPTA (**Figure 3-1(a)**), the T_m of the film became lower (45 ℃), and the energy absorption peak became wider. This can be explained by the interrupted crystallization of SA moieties by ETPTA crosslinkers. The decrease in T_m is favored to reduce the energy cost when heating the film. When preparing for the SEM images of both films in semicrystalline states, a heating process was required and allowed the films to be kept at 50 °C to become fully soft and transparent. Then the films were left in ambient temperature until they change back to rigid and opaque state. Based on the SEM images, neat SA film was smooth at both pristine and semicrystalline states, showing a uniform morphology with no surface patterns. On the contrary, the SEM images for SW film at both pristine and semicrystalline states display a rough surface with phase separation induced patterns. As seen in **Figure 3-1(d)-iii,iv**, the feature size of the patterns are around 2-3 μm, which is large enough to scatter the whole solar spectrum. This morphology difference between neat SA film and SW film matches the transmittance spectrum difference of the two films as shown in **Figure 3-2**. Based on the XRD results (**Figure 3-1(b)**), the slightly widened XRD peak of SW film demonstrates a little larger crystalline size (4.7-5 nm) when compared to neat SA film. This size of crystals still strongly scatters UV-blue light and contributes to the low transmittance of SW film shown on the transmittance spectrum (**Figure 3-2**), but the micro-sized patterns on the SW film at the opaque

state helps lower the transmittance of red-NIR light by 34% (at 1500 nm) when compared to neat SA film. An optical microscope was utilized to record the in-situ transition of the films from opaque to transparent states and the recovery process. The films were heated and cooled several times before characterization to stabilize the surface patterns. **Figure 3-3(a)** shows the surface morphology of the SW film during the cold state where the micro-sized patterns can be clearly observed on the optical image. When heated up, the film became transparent due to the relaxation of SA moieties, and the surface patterns became more flattened. In **Figure 3-3(b)**, the surface of the heated SW film cannot become completely smooth due to cured bonds between SA and ETPTA chains, which are responsible for preserving the phase separation between the two components. This observation matches the transmittance spectrum of the heated film as shown in **Figure 3-2**. At the transparent state, the neat SA film with a smooth surface has a high parallel transmittance around 97% at 550 nm, while a SW film shows a small drop of 1.5% in parallel transmittance. The overall transmittance of SW film at transparent state is still comparable to a transparent glass. The SW film recovery property was evaluated by cooling the film back to room temperature where the same spot was captured under optical microscope. As shown in **Figure 3-3(c)**, the surface patterns were restored.

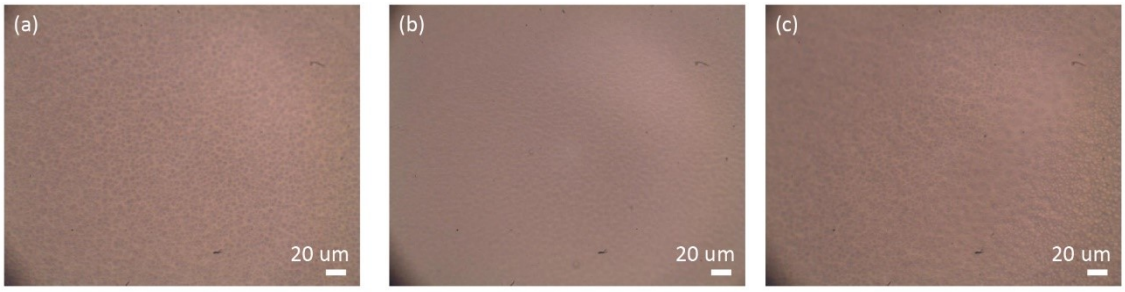

Cold Heat Cold

Figure 3-3. Microscope images of SW films during one switching cycle. Initial opaque status **(a)** showing a rough surface patterns induced by phase separation. After being heated up, the transparent film **(b)** demonstrates a smoother surface. When being cooled down again, the surface patterns **(c)** restored.

In addition to the micro-phase separation, the difference of refractive indices of SA and ETPTA components also contribute to the opacity switch. With matching refractive indices, light can pass through a film even though multiple domains exist, rendering the film transparent. When the contrast of refractive index of different domains become large, the light will scatter at the interface of domains, and result in an opaque film. The refractive index of neat SA film and neat ETPTA film under elevated temperatures were investigated with a refractometer. As shown in **Figure 3-1(e)**, the refractive index of ETPTA film only slowly decreased from 1.486 (at R.T.) to 1.478 (at 48 °C); whereas the refractive index of neat SA film decreased gradually before T_m, but sharply dropped from 1.498 (at 44 °C) to 1.477 (at 48 °C) near the melting temperature. The large difference in refractive index of SA film and ETPTA film at room temperature aids the opacity of SW film at the opaque state. At approximately 48 °C, when the SA component completely transitioned into amorphous state, the refractive indices of SA and ETPTA nearly matched (less than 0.1% difference). This matching refractive index guarantees the transparency of SW film even with separated SA and ETPTA domains.

An all-solid smart window without any inclusion of nanoparticles or liquid crystals is possible due to a combination of three mechanisms: the reversible crystalline-to-amorphous transition of SA enables the switching property of this SA-ETPTA smart windows; the phase separation between SA and ETPTA components improves the whole solar spectrum opacity of

the SW film at opaque state; and the matching refractive index of SA and ETPTA at transparent state assist the high transparency even with separated SA and ETPTA domains.

With these combined three mechanisms, the resulted SW film has a good light modulation capability over the whole solar spectrum. The integral solar, luminous and IR transmittances ($T_{solar/lum/IR}$) were calculated based on the measured transmittance spectra with the following equation:

$$T_{solar/lum/IR} = \frac{\int \varphi(\lambda) T(\lambda) d\lambda}{\int \varphi(\lambda) d\lambda},$$

where λ is the light wavelength, T(λ) is the measured transmittance. For T_{solar} or T_{IR}, ψ(λ) is the solar irradiance spectrum for air mass 1.5; and for T_{lum}, ψ(λ) is the CIE "physiologically-relevant" luminous efficiency functions.[4] And transmittance modulation ($\Delta T_{solar/lum/IR}$) of the film was calculated through subtracting the transmittance at transparent state by the transmittance at opaque state. As shown in **Figure 3-2(c)**, SW film and neat SA film are compared for solar (300 – 2500 nm), luminous (390 – 780 nm) and IR (780 – 2500 nm) transmittance performances. In **Figure 3-2(c)**, film transmittances at cold state are denoted as red columns, blue columns mark the solar/luminous/IR transmittance modulation, and the film transmittances at transparent state are represented by the total height of red and blue columns. For the solar/luminous/IR transmittance at opaque state and transmittance modulation, SW films shows much better performances over the neat SA film. And the two films demonstrate comparable performance at transparent state. The high T_{IR} of 51.46% for the neat SA film results in a limited ΔT_{solar} of 61.7%. With the introduction of Mie scattering by the phase separation from the two polymer components, the T_{IR} of the SW film drops to 26.26% and contributes to a high ΔT_{solar} of 70.2%. Since IR light contributes to 53% of the total solar energy,[4] the large

modulation of IR light of the SW film is beneficial for preserving the heat/cold within the building rooms during winter/summer, and can potentially reduce the energy consumption of building heating and cooling. For privacy protection purpose, SW film's luminous transmittance modulation was also evaluated. From opaque state to transparent state, the T_{lum} increases from 14.89% to 95.3%, which creates an 80.41% visible light modulation. The high opacity of the SW film at opaque state rivals with highly textured glasses with high privacy level (level 7-10, 0% - 30% transmittance) for privacy protection purpose. Among the best reported thermochromic smart window films, the ΔT_{solar} and T_{lum} performance of this SW film are at the high end as compared to its counterparts (**Figure 3-2(d)**).[4, 15, 19, 31-38]

Although the SW film can be used as an all-solid smart window, the process to heat up the film involved a cumbersome hotplate and could be significantly improved with an attached heater.

3.3.2 Fabrication and Characterization of AgNW Transparent Heater

Simple operation of a smart window is a key specification for an attractive product, and the use of a hotplate will not be widely accepted. A transparent heater in conjunction with the SW film would enable simple operation of a smart window. In this work, AgNW was selected as the basis of the heater due to its high transparency and flexibility. The fabrication of AgNW heater is illustrated in **Figure 3-4** and described in the Materials and Method section. The final AgNW composite heater consists of a percolation network of AgNWs that is embedded in a polyurethane acrylate (PUA) matrix. The selected PUA matrix imparts excellent transparency, toughness, and non-yellowing properties. The transparency of this composite heater surpasses

previous reported AgNW transparent electrodes.[39] As seen in the transmittance spectrum (**Figure 3-6(a)**), the neat PUA films shows a 100% transmittance at 550 nm. With embedded AgNW networks of different conductivities, the transmittances at 550 nm for 10 Ω sq^{-1}, 15 Ω sq^{-1}, 20 Ω sq^{-1}, 25 Ω sq^{-1} composite heaters are 87.6%, 90.8%, 93.4% and 94.2% respectively. Commercial ITO-glass and ITO-polyethylene terephthalate (PET) films have transmittance of 84% @ 10 Ω sq^{-1} and 80% @ 30 Ω sq^{-1}, respectively. AgNWs composite heaters with a little higher resistance (20 Ω sq^{-1} or 25 Ω sq^{-1}) were selected to retain high transparency for the smart window films. The PUA matrix also helps protect the embedded AgNWs network from environment and normal working wear. The storage modulus of the pure PUA film was measured to be 190 MPa at room temperature (**Figure 3-5**). Scotch magic tape was adhered to the conductive side of the composite heater and then peeled off, after 100 cycles of this peeling experiments, the transient resistances (**Figure 3-6(b)**) didn't change for both heaters with resistance of 20 Ω sq^{-1} and 25 Ω sq^{-1}, indicating a strong bonding between AgNWs and PUA matrix. Mechanical flexibility of the composite heater was also evaluated through a bending experiment (**Figure 3-6(c)**). The heater was attached to a custom-designed linear stage and was repeatedly bent to a radius of 2 mm (**Figure 3-6(d)**). The resistance of this AgNWs composite heater remained stable after 1600 bending-unbending cycles with a moving speed of 50 mm s^{-1}.

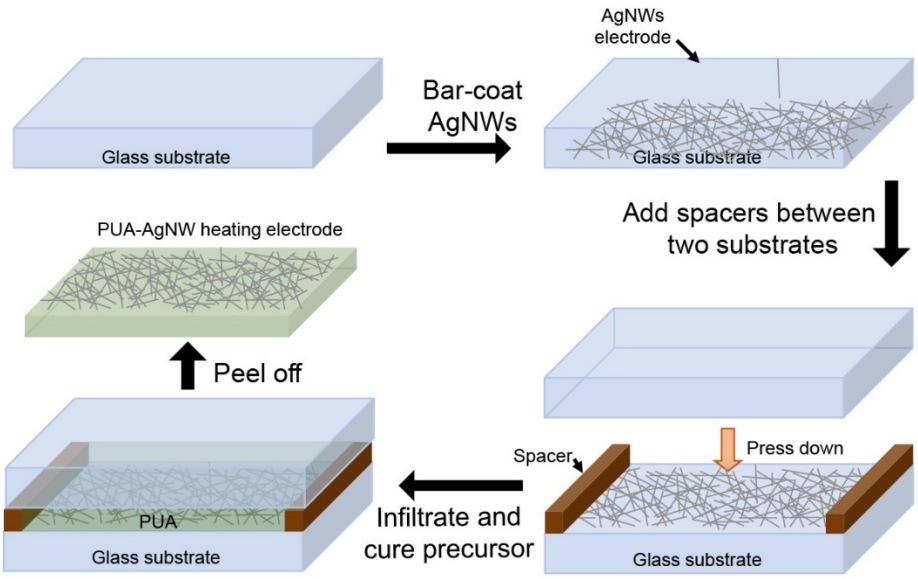

Figure 3-4. A schematic illustration for the fabrication process of AgNW/PUA composite heater.

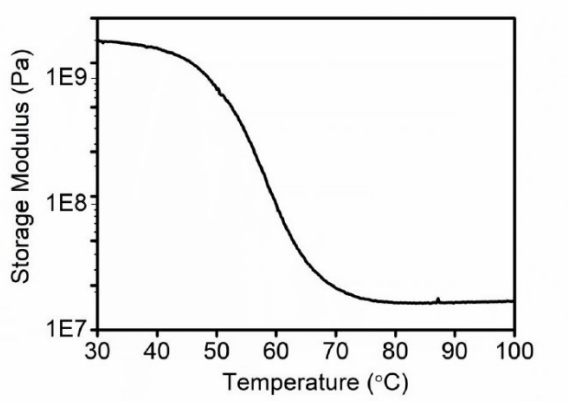

Figure 3-5. Storage modulus versus temperature for AgNW/PUA composite heater.

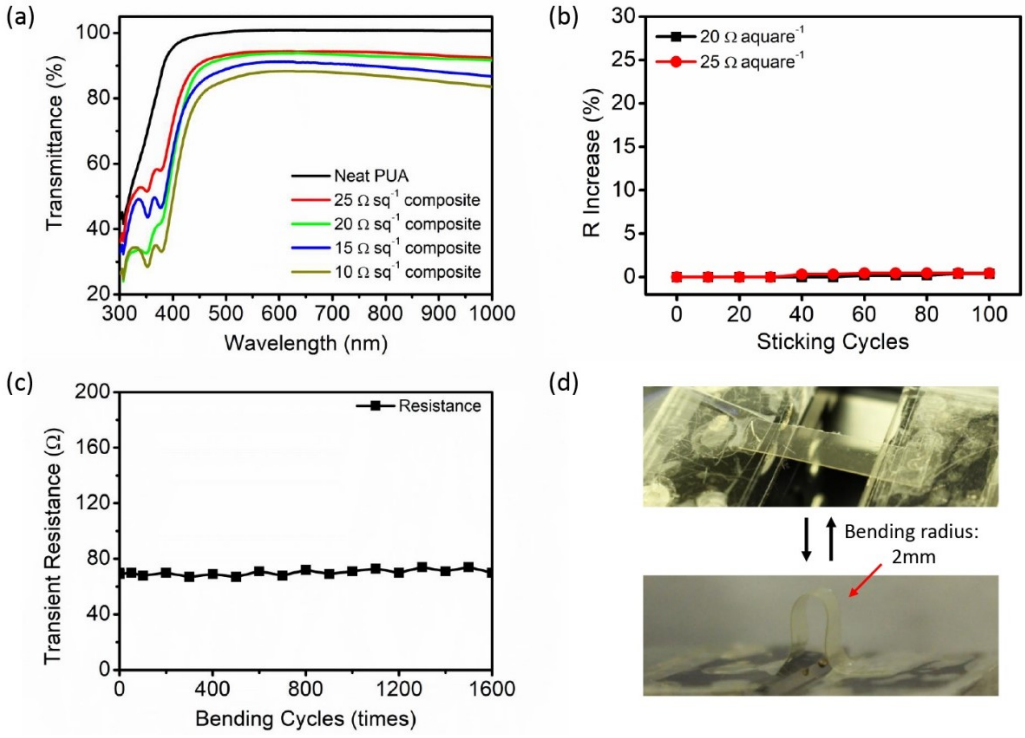

Figure 3-6. Performances of AgNW/PUA composite heaters. (a) Transmittance spectrum of AgNW/PUA composite heaters with different sheet resistance. **(b)** Resistance change with sticking cycles. **(c)** Resistance change with bending-unbending experiments. **(d)** Setup for bending-unbending experiments.

To gauge the heating performance of the AgNWs composite heater, aluminum and silver paste was applied to two sides of the heater film as the side contacts, leaving an active heating area of 2.37 cm x 2.43 cm. A similar setup is shown in **Figure 3-9(a),** and the active heating area is indicated with a dotted red square frame. The prolonged joule heating property also demonstrates the stability of these two AgNWs composite heaters. As shown in **Figure 3-7(a)**, when applied with certain DC voltages (4-5 V), both heaters can be ramped up to and maintained at 70 °C for more than 2 hours without adjusting the external voltage. The constant temperature

output reflects the stable resistance of the oxidation-free AgNWs, thanks to the protection of PUA matrix. Different DC voltages were then applied to the composite heater, and the saturation temperatures were measured with an infrared (IR) camera. **Figure 3-7(c)** shows the time dependent temperature change of the composite heaters with different resistances. Each level of DC voltage was kept until the temperature of the films were saturated. **Figure 3-7(d)** displays the IR images of the composite heater with 25 Ω sq^{-1} sheet resistance at different DC voltages. A relatively uniform heating property throughout the whole film was observed even at high temperatures. As compared in **Figure 3-7(e)**, the temperature of the composite heater with a lower sheet resistance increased slightly faster with applied voltage. The fitted curves of the two composite heaters reflect a linear relationship between the temperature and square of the applied DC voltage. As for the power efficiency, the two heaters with different resistances show a similar performance as seen in **Figure 3-7(f)**. The slope of the saturated temperature-power density curve exhibited a power efficiency of >300 °C cm^2 W^{-1} for both heaters. Since the transition temperature of the working SW film is around 45 °C, only 3-4 V DC voltage is needed to switch on the SW film with a required working power density that is less than 0.1 W cm^{-2}. The heating cycle property of the AgNWs composite heaters were also assessed by repeatedly applying and removing DC voltages. As shown in **Figure 3-7(b)**, specified square wave voltages were applied to AgNWs composite heaters with different resistances, both heaters were heated to 70 °C, and then cooled to room temperature for 6 cycles. The temperatures of the films showed no deviation between each cycle, indicating good repeatability.

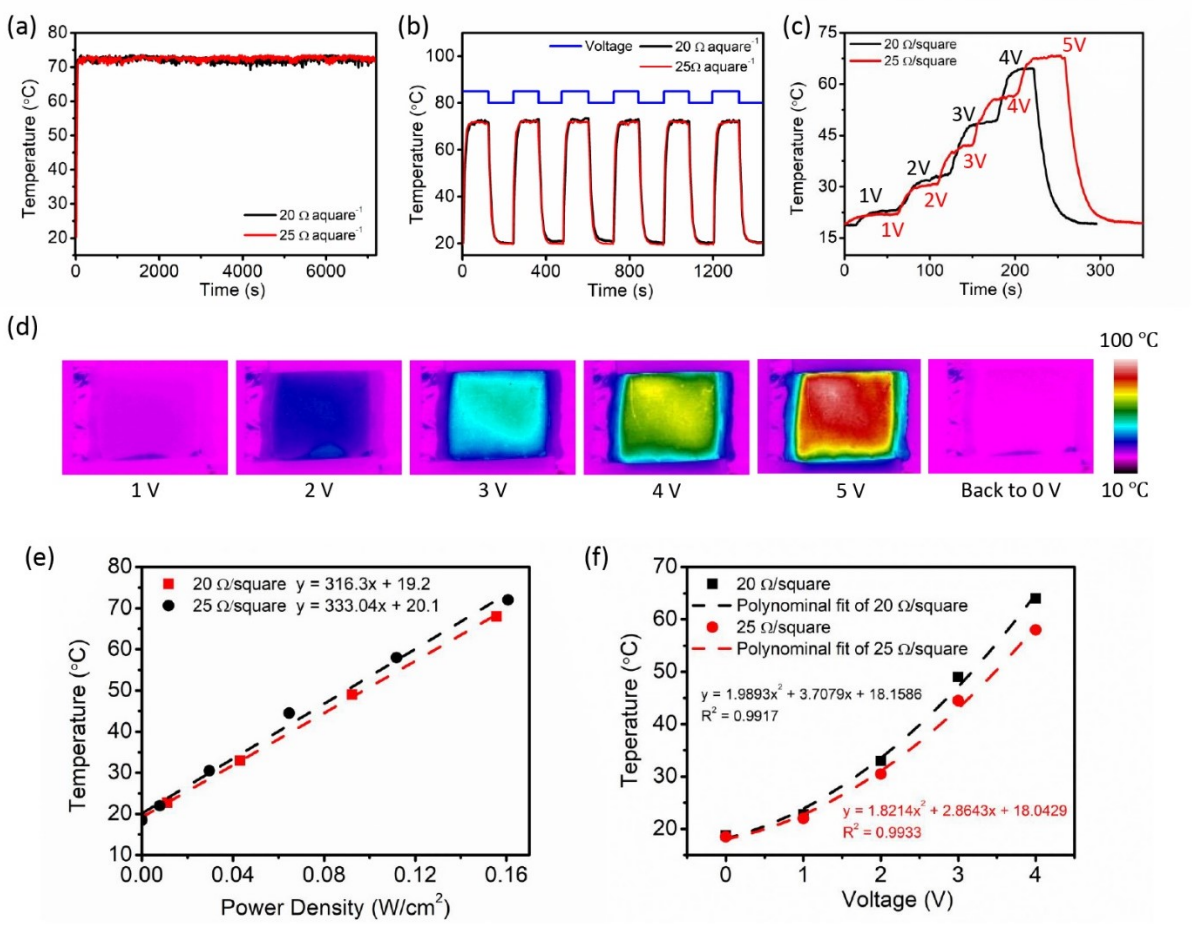

Figure 3-7. Heating performance of AgNW/PUA composite heaters. (a) Long term joule heating properties. **(b)** Cyclic joule heating tests with applied square wave voltages. **(c)** Time-dependent temperature change with increased external voltages. **(d)** IR images at different applied voltages showing temperature distributions of AgNW/PUA composite heaters. **(e)** Saturation temperatures at various power densities. The power efficiency is indicated by the slope. **(f)** Heater saturation temperature as a function of external voltage.

3.3.3 Smart Window Demonstration

With a switchable working SW film and a transparent AgNWs composite heater, a smart window application was demonstrated by sandwiching a SW film in between a transparent AgNWs composite heater and a transparent PUA film, followed by a hot pressing process to seal the device. The structure of this smart window can be seen in **Figure 3-8**. Both top PUA transparent film and bottom PUA/AgNW electrode have thickness around 70 μm. For the smart window device (**Figure 3-9(a)**), the initial state of the film is opaque, and the "UCLA" patterns cannot be seen through the SW film. When heated above its transition temperature, the SW film becomes transparent and the text "UCLA" becomes visible. After cooled to room temperature again, the SW film returns to its opaque state and blocks "UCLA" patterns underneath. 500 opaque-transparent switching cycles were tested on this smart window device. **Figure 3-9(d),(e)** shows the parallel and diffusive transmittances change for the first 5 and last 5 switching cycles. For the last 5 switching cycles, the transmittance remains consistent at both opaque and transparent states of the smart window. For a typical switching cycle, the parallel transmittance of the smart window changed from 92% to 13% (at 550 nm). And the averaged transmittance modulation contrast is about 79%. The diffusive transmittance of a smart window was recorded for one switching cycle to measure its switching speed. As seen in **Figure 3-9(c)**, even though it takes 160s for the smart window (1.5 cm x 2.5 cm) to equilibrate at its transparent/opaque states after turning on/off the heater, but less than 60s is needed for it to reach 90% of the total light modulation before equilibrium. A larger SW film (5 cm x 7 cm) was attached to a real window to show its feasibility for practical applications (**Figure 3-10(a),(b)**). By heating up and cooling down the SW film, the background building can be controlled to show up or hide. Since all the components for the smart window are flexible, the SW device was also attached to a curved surface to test the performance for the need of windows with curved shape. The SW device was

fixed to the outer surface of a vial with radius of 1 cm (see **Figure 3-9(b)**). A piece of paper printed with "UCLA" patterns were attached the other outer side of the vial. With the application and removal of external DC power supply, the SW device can be switched between opaque and transparent states.

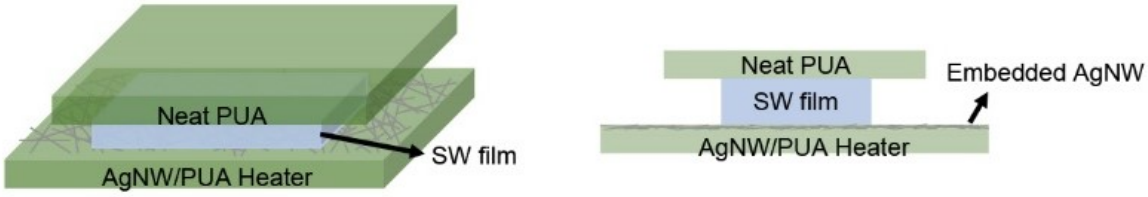

Figure 3-8. Schematic illustration of the device structure for a smart window design.

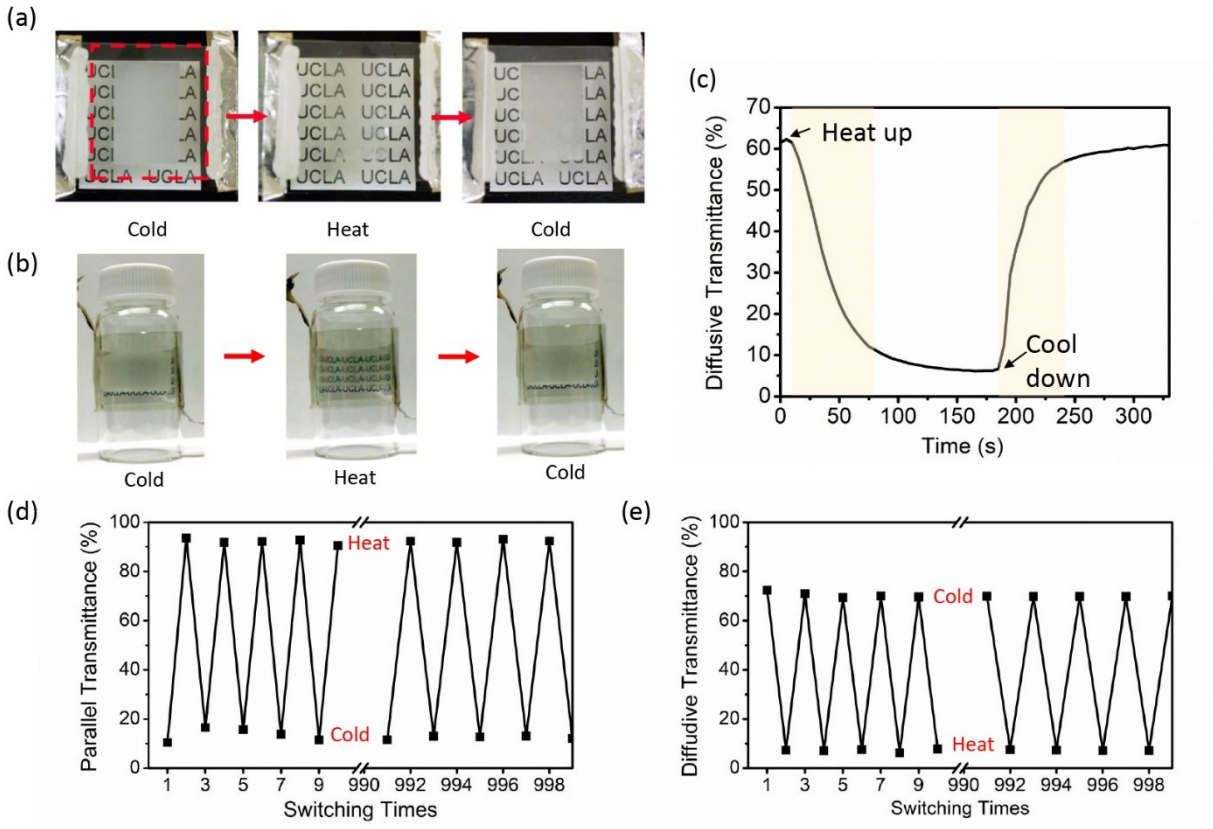

Figure 3-9. Demonstration of all-solid smart windows. (a) One switching cycle of a flat smart window. Underneath "UCLA" patterns can show up or hide upon the switching on/off of this smart window. The red dotted square frame indicates the location of AgNW/PUA composite heater. **(b)** One switching cycle of a curved smart window that is mounted on a round vial. **(c)** Switching speed of smart windows. **(d)** and **(e)** are parallel and diffusive transmittance spectra of cyclic switching of a flat smart window for over 500 cycles.

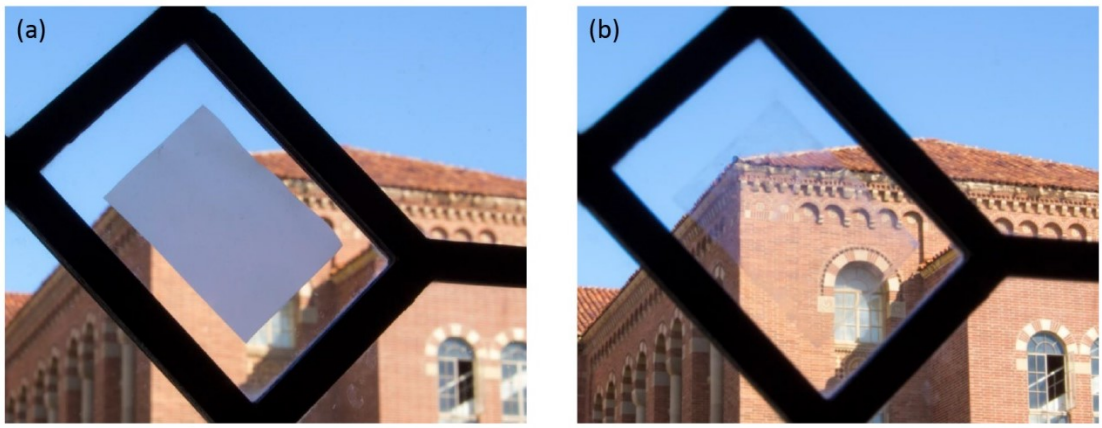

Figure 3-10. Demonstration of all-solid smart windows. (a) and **(b)** are opaque and transparent statuses of a flat smart window that was mounted on a real glass window.

3.4 Conclusion

In conclusion, our work is the first one to utilize a three-fold mechanism to fabricate an all-solid wide-bandwidth thermochromic smart window device without the inclusion of any metal/metal oxide nanoparticles or liquid crystals through a facile solution processed procedure. The opacity switching capability of the SW film comes from three aspects: the reversible

crystalline-to-amorphous transition of SA allows the repeatability switching of the film, micro-phase separation between SA and ETPTA provides high opacity over the whole solar spectrum at opaque state, and the matching refractive indices of SA and ETPTA assures the transparency at transparency state. The all solution processed SW device can be switched among a wide light bandwidth and obtains a large ΔT_{lum} of 80.41% and ΔT_{solar} of 70.16%, which is still functioning on curved surfaces. The free-of-liquid SW film also facilitate the long cycle lifetime. The heating element for the SW device was fabricated with AgNW/PUA composite film, which imparts high transparency and robustness. For further improvement, transparent heaters with higher power efficiency should be investigated to reduce the power consumption.

3.5 Reference

[1] O. Edenhofer, *Climate change 2014: mitigation of climate change*, Cambridge University Press, **2015**.

[2] B. G. Richter, David; Crabtree, George; Glicksman, Leon; Goldstein, David; Greene, David; Kammen, Dan; Levine, Mark; Lubell, Michael; Savitz, Maxine; Sperling, Daniel; Schlachter, Fred; Scofield, John; Dawson, James, *Rev. Mod. Phys.* **2008**, 80, S1.

[3] N. C. Davy, M. Sezen-Edmonds, J. Gao, X. Lin, A. Liu, N. Yao, A. Kahn, Y.-L. Loo, *Nature Energy* **2017**, 2, 17104.

[4] X.-H. Li, C. Liu, S.-P. Feng, N. X. Fang, *Joule* **2019**, 3, 290.

[5] L. Long, H. Ye, *Scientific reports* **2014**, 4, 6427.

[6] R. Yoshikawa, M. Tenjimbayashi, S. Shiratori, *ACS Applied Energy Materials* **2018**, 1, 1429.

[7] U. Joost, A. Šutka, M. Oja, K. Smits, N. Döbelin, A. Loot, M. Järvekülg, M. Hirsimäki, M. Valden, E. Nõmmiste, *Chemistry of Materials* **2018**, 30, 8968.

[8] Y. Ke, S. Wang, G. Liu, M. Li, T. J. White, Y. Long, *Small* **2018**, 14, 1802025.

[9] D. Cao, C. Xu, W. Lu, C. Qin, S. Cheng, *Solar RRL* **2018**, 2, 1700219.

[10] F. Bella, G. Leftheriotis, G. Griffini, G. Syrrokostas, S. Turri, M. Grätzel, C. Gerbaldi, *Advanced Functional Materials* **2016**, 26, 1127.

[11] H. Najafi-Ashtiani, S. Gholipour, A. Rahdar, *Journal of Molecular Structure* **2018**, 1169, 25.

[12] T. D. Nguyen, L. P. Yeo, T. C. Kei, D. Mandler, S. Magdassi, A. I. Y. Tok, *Advanced Optical Materials* **2019**, 1801389.

[13] Q. Zhao, Y. Fang, K. Qiao, W. Wei, Y. Yao, Y. Gao, *Solar Energy Materials and Solar Cells* **2019**, 194, 95.

[14] Z. Wang, M. Zhu, S. Gou, Z. Pang, Y. Wang, Y. Su, Y. Huang, Q. Weng, O. G. Schmidt, J. Xu, *ACS applied materials & interfaces* **2018**, 10, 31697.

[15] Y. Zhou, M. Layani, S. Wang, P. Hu, Y. Ke, S. Magdassi, Y. Long, *Advanced Functional Materials* **2018**, 28, 1705365.

[16] A. K. Singh, S. Kiruthika, I. Mondal, G. U. Kulkarni, *Journal of Materials Chemistry C* **2017**, 5, 5917.

[17] T.-G. La, X. Li, A. Kumar, Y. Fu, S. Yang, H.-J. Chung, *ACS applied materials & interfaces* **2017**, 9, 33100.

[18] S. Kiruthika, G. Kulkarni, *Solar Energy Materials and Solar Cells* **2017**, 163, 231.

[19] X. Liang, M. Chen, S. Guo, L. Zhang, F. Li, H. Yang, *ACS applied materials & interfaces* **2017**, 9, 40810.

[20] X. Liang, S. Guo, M. Chen, C. Li, Q. Wang, C. Zou, C. Zhang, L. Zhang, S. Guo, H. Yang, *Materials Horizons* **2017**, 4, 878.

[21] T. Liu, B. Liu, J. Wang, L. Yang, X. Ma, H. Li, Y. Zhang, S. Yin, T. Sato, T. Sekino, *Scientific reports* **2016**, 6, 27373.

[22] T. Tani, S. Hakuta, N. Kiyoto, M. Naya, *Optics express* **2014**, 22, 9262.

[23] G. Cai, A. L. S. Eh, L. Ji, P. S. Lee, *Advanced Sustainable Systems* **2017**, 1, 1700074.

[24] Y. Ke, C. Zhou, Y. Zhou, S. Wang, S. H. Chan, Y. Long, *Advanced Functional Materials* **2018**, 28, 1800113.

[25] M. Li, S. Magdassi, Y. Gao, Y. Long, *Small* **2017**, 13, 1701147.

[26] N. Wang, M. Duchamp, R. E. Dunin-Borkowski, S. Liu, X. Zeng, X. Cao, Y. Long, *Langmuir* **2016**, 32, 759.

[27] H. Khandelwal, A. P. Schenning, M. G. Debije, *Advanced Energy Materials* **2017**, 7, 1602209.

[28] H. Y. Lee, Y. Cai, S. Velioglu, C. Mu, C. J. Chang, Y. L. Chen, Y. Song, J. W. Chew, X. M. Hu, *Chemistry of Materials* **2017**, 29, 6947.

[29] L. Zhang, M. Wang, L. Wang, D.-k. Yang, H. Yu, H. Yang, *Liquid Crystals* **2016**, 43, 750.

[30] K. M. Lee, V. P. Tondiglia, M. E. McConney, L. V. Natarajan, T. J. Bunning, T. J. White, *ACS Photonics* **2014**, 1, 1033.

[31] Y. Zhou, Y. Cai, X. Hu, Y. Long, *Journal of Materials Chemistry A* **2015**, 3, 1121.

[32] Y. Zhou, Y. Cai, X. Hu, Y. Long, *Journal of Materials Chemistry A* **2014**, 2, 13550.

[33] J. SD, L. YM, *J. Mater. Chem. C* **2014**, 2, 3812.

[34] L. Dai, S. Chen, J. Liu, Y. Gao, J. Zhou, Z. Chen, C. Cao, H. Luo, M. Kanehira, *Physical Chemistry Chemical Physics* **2013**, 15, 11723.

[35] J. Zhu, A. Huang, H. Ma, Y. Chen, S. Zhang, S. Ji, S. Bao, P. Jin, *New Journal of Chemistry* **2017**, 41, 830.

[36] N. Shen, S. Chen, Z. Chen, X. Liu, C. Cao, B. Dong, H. Luo, J. Liu, Y. Gao, *Journal of Materials Chemistry A* **2014**, 2, 15087.

[37] C. Liu, S. Wang, Y. Zhou, H. Yang, Q. Lu, D. Mandler, S. Magdassi, C. Y. Tay, Y. Long, *Journal of Alloys and Compounds* **2018**, 731, 1197.

[38] J. Zhu, A. Huang, H. Ma, Y. Ma, K. Tong, S. Ji, S. Bao, X. Cao, P. Jin, *ACS applied materials & interfaces* **2016**, 8, 29742.

[39] J. Liang, L. Li, X. Niu, Z. Yu, Q. Pei, *Nature Photonics* **2013**, 7, 817.

Chapter 4

Hierarchical Bacterial Cellulose-Silver Nanowire Composite Fiber-Based Wearable Pressure Sensors

4.1 Introduction

To improve human wellness, fitness, and rehabilitation of people with skin damage or amputations, and enhance robotic intelligence, researchers have applied intensive efforts to innovate artificial skin or wearable electronics with multiple functions.[1] These smart medical devices can detect many human-related signals, including perspiration, sound, temperature, electrocardiograms, electroencephalograms and so on.[2] Among them, pressure detection is one of the most important functions for physiological signal monitoring as it is a near instantaneous response mechanism that can be exploited through several sensing methods. Sensors can either be put on stretchable polymeric substrates that can conform to human skin or can be directly integrated into textiles for wearable pressure sensing solutions. Fabric- or fiber-based pressure sensors hold great promise due to the advantages of deformability, breathability, comfort, low cost, and simple integration with clothing.[3] Several fabric- or fiber-based sensing devices have

been explored, and some of the most common are capacitive, piezoresistive, and piezoelectric modalities.[1] Piezoelectric pressure sensors are good for sensing dynamic forces, where as piezoresistive sensors are more suitable for detecting large strains based on their working mechanism. Capacitive pressure sensors are more popular for distinguishing static forces due to their facile fabrication, high sensitivity to static pressure, signal repeatability, and low power consumption.[2-4]

The fabric-/fiber- based capacitive pressure sensors are generally composed of two compliant conductive fibers or fabrics separated by flexible dielectric spacers. Under an applied external force, a change of dielectric thickness leads to the variation of capacitance. For fabric-based sensors, although the design is simple, their relatively large sizes limit the advanced applications for some fields requiring smaller size sensors and higher sensing resolution. Additionally, large sensor patches negatively affect the comfort and flexibility upon integration into clothing. In contrast, fiber-based capacitive sensors could fundamentally resolve the problems since their sizes are comparable to commercial thread, which can be easily woven into clothes for high resolution sensing. Lee et al. fabricated a fiber-based pressure sensor by coating Kevlar fiber with poly(styrene-block-butadien-styrene) (SBS) and Ag nanoparticles as a dielectric and conductive layered medium.[3] Similarly, Jin et al. realized a highly sensitive and wearable sensor by dipping strands of yarn into a polyvinyl alcohol (PVA) solution and a dispersion of graphene nanoplatelets successively.[5] However, these sensors haven't yet satisfied the requirement of high resolution and sensitivity owing to the relatively large diameter of the fibers and limited relative change of the dielectrics thickness under pressure. Microstructures, such as interlocked structures,[6] hollow spheres,[4] sponges,[7] patterned microstructures,[8] have been introduced in dielectric or electrode layers to help increase the sensitivity of sensors. Atalay

at el. assembled a sensor with knitted conductive fabric.[4] This sensor's sensitivity is three times larger than the sensor with woven conductive fabric due to the knitted fabric having a higher volume of air inside. He at el. included a nylon mesh as a porous dielectric layer to improve the sensitivity of the sensor, which can be used to detect human pulse and an elastic interaction of a water drop.[9] Those microporous structures are widely studied in planar fabric-based capacitive sensors, but implementations in fiber-based sensors haven't been reported yet. On the other hand, the fabrication of fabric-/fiber- based electrodes has typically been realized through growing metal nanoparticles on the surface or dip coating with conductive materials. Creating a percolation network of metal nanoparticles typically requires an expensive high metal content, which is further hindered by peeling issues between conductive materials and fabric/fiber due to their weak bonding.

In this chapter, we will introduce a facile fabrication of a low cost, ultrasensitive fiber-based sensor with hierarchical structures and high resolution. The conductive core of the fiber is made of TEMPO-oxidized bacterial cellulose (TOBC)/silver nanowire (AgNW) composite. The hierarchical structure of TOBC/AgNW composite electrode provides a high sensitivity along with the benefits of high strength and biocompatibility provided by the renewable, natural, and inexhaustible source of bacterial cellulose. The AgNWs formed a percolation network within TOBC with a relatively low weight content when compared to nanoparticles due to its high aspect ratio, which is also preferable for its inexpensive nature. The strong bonding between AgNW and TOBC also enables an extensive lifetime of usage. The TOBC/AgNW fiber-based sensor shows a high resolution and sensitivity owing to its ultrathin diameter (53 μm) and high conductivity (1.3×10^4 S cm^{-1}). This ultrathin fiber can be sewn into clothing which can meet both a level of comfort that a user would enjoy while also being fashionable. An additional benefit to

being ultrathin was the development into a highly flexible and sensitive sensor for heartbeat and vocal pulses. The vocal waveforms of the digits 1-10 were fed into a machine learning model for speech recognition, and > 90% predicting accuracy was achieved.

4.2 Experimental

4.2.1 Materials

Poly-(vinylpyrrolidone) (PVP) (MW = 50 000) was purchased from Sigma-Aldrich. AgNWs with an average diameter of 25-35 nm and length of 15-25 um were provided by Kechuang. The Sylgard 184 silicone elastomer was obtained from Dow.

4.2.2 Preparation of TEMPO-Oxidized Bacterial Cellulose

TEMPO-oxidized bacterial cellulose (BC) is prepared based on a previously published paper.[10] Briefly, the BC slurry (1 g) was suspended into the aqueous solution of TEMPO (0.016 wt%) and sodium bromide (0.1 wt %). Subsequently, sodium hypochlorite was added to initiate the reaction at room temperature. Once stable at a pH of 10.3, the solution was titrated by 0.5 M sodium hydroxide for 1 h. Finally, after filtering and washing with distilled water, the oxidized cellulose suspension was concentrated to the desired concentration (0.22 wt %) by centrifugation.

4.2.3 Preparation of TOBC–AgNW Spinning Dope

A PVP solution was created by dispersing PVP in DI water at concentration of 0.5 wt%. Separately, a homogeneous dispersion of AgNW was created by addition of 0.5 mL of 1 wt% AgNW solution into isopropanol (IPA) which was subsequently added into 2.5 mL of the aforementioned PVP solution. The AgNW mixture will then have 3.41 mL of 0.22 wt % TOBC added into the vial and vortex mixed at 3000 rpm for 10 min. Under gentle stirring, 90 mL of acetone was added to the suspension dropwise. The resulting solution was then centrifuged at 5000 rpm for 20 min where the supernatant was subsequently discarded. The precipitate was re-dispersed in 0.25mL of water and vortex mixed until a homogeneous dispersion of TOBC/AgNW ink with AgNW concentration of 20 mg mL^{-1} and TOBC concentration of 30 mg mL^{-1} was formed.

4.2.4 Wet-Spinning of TOBC/AgNW Fibers

The TOBC/AgNW ink was spun through a needle with a diameter of 0.4 mm into the acetone coagulation bath at the speed of 2.1 m min^{-1}. The spun fibers were pulled out from the acetone coagulation bath and dried in air under tension. The dried fibers were then immersed in a 0.1 M calcium dichloride crosslinking solution for 12 hrs. Excess ions/salt were washed away with deionized water.

4.2.5 Assembly of TOBC/AgNW/PDMS sensors

PDMS dielectric was prepared by uniformly mixing PDMS prepolymer (Sylgard 184A) and curing agent (Sylgard 184B) with the ratio of 10:1, and then coated onto the surface of

TOBC/AgNW fibers. The coated TOBC/AgNW/PDMS structure was then cured at 60 °C for 30 min. Two TOBC/AgNW/PDMS fibers were stacked perpendicularly with each other for the assembly of the pressure sensor. Two pieces of aluminum foil were attached at the ends of TOBC/AgNW/PDMS fibers by silver paste for electrical connections. Paper or shape memory polymer were chosen as the substrates for the sensors depending on the exact application.

4.2.6 Characterization

The morphology of the fibers was characterized by a high-resolution field emission scanning electron microscope (FEI Nova Nano SEM 600). The distribution of Ag and Ca elements was tested by Energy-dispersive X-ray spectroscopy (FEI Nova Nano SEM 230). The morphologies of the TOBC and AgNW fibers were analyzed by FEI T12 Quick CryoEM and CryoET microscope. The bending stability of the TOBC/AgNW fibers was conducted on a motorized linear stage with a built-in controller (Zaber Technologies Inc.). Mechanical performance was investigated on a TA Instruments RSAIII dynamic mechanical analyzer (DMA). The capacitance signals were obtained from an LCR meter (Agilent 4284A) at a voltage of 1 V and frequency of 1 MHz. The assembly of Mark-10 M7-012 force gauge and ESM 303 test stand were used to load specific pressures onto the pressure sensor.

4.2.7 Machine Learning Classification Model for Phonation Recognition

4.2.7.1 Data Collection

The TOBC/AgNW/PDMS pressure sensor was mounted on the throat of a female test subject. The vocal waveforms of the numbers 1-10 were collected through the pressure sensor by allowing the test subject to speak each number 10 times. Capacitance vs. time data was recorded for each number at the frequency of 10 Hz, and the capacitance data were labelled manually.

4.2.7.2 Data Pre-processing

The raw vocal waveforms were first selected manually to filter out abnormal data that were affected by test subject's motions, like swallowing. The resultant dataset has 93 valid inputs which was formatted based on the tsfresh formatting rule. Tsfresh is a python package that automatically calculates time series characteristics. 285 relevant features of the 1-10 digit vocal waveforms were extracted through tsfresh augmenter. The feature dataframe was then normalized with zero mean and unit variance which is the final preparation necessary prior to being fed into classifiers.

4.2.7.3 Baseline

Before feeding the feature dataset into classifiers, a baseline classification was performed without feature extraction. Due to each digit's vocal waveform input having varying total time lengths, another time series python package, tslearn, was used to transform all the input data into the same shape (93, 40). The transformed dataset was also normalized with zero mean and unit variance before use. A random forest classifier was selected due to its good performance which was evaluated through a grid search with 6-fold cross validation. The best result achieved used

200 trees and a maximum depth of 45 for each tree. The grid search results are shown **Figure 4-1**, and the best prediction accuracy result for this classifier is 0.7154.

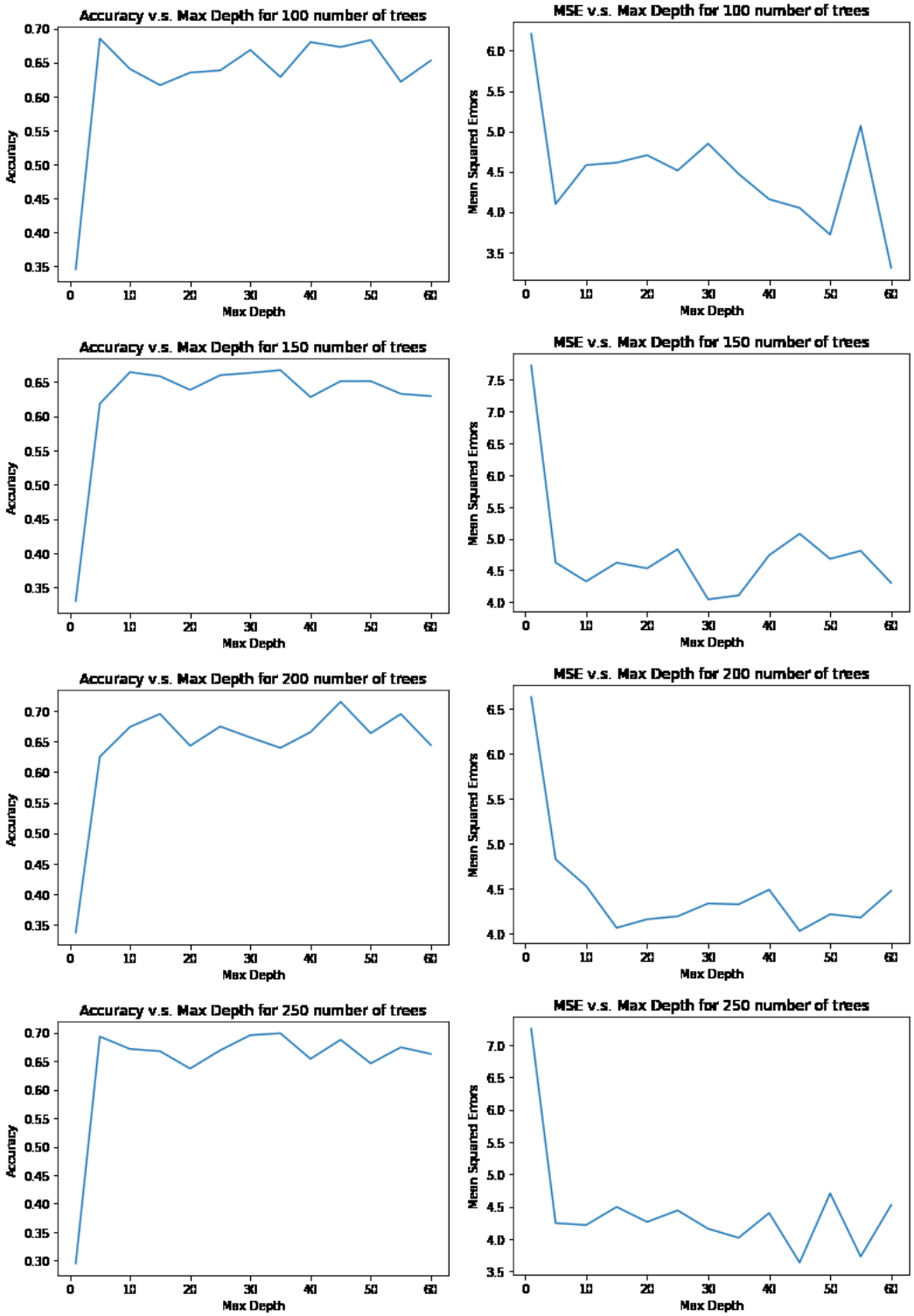

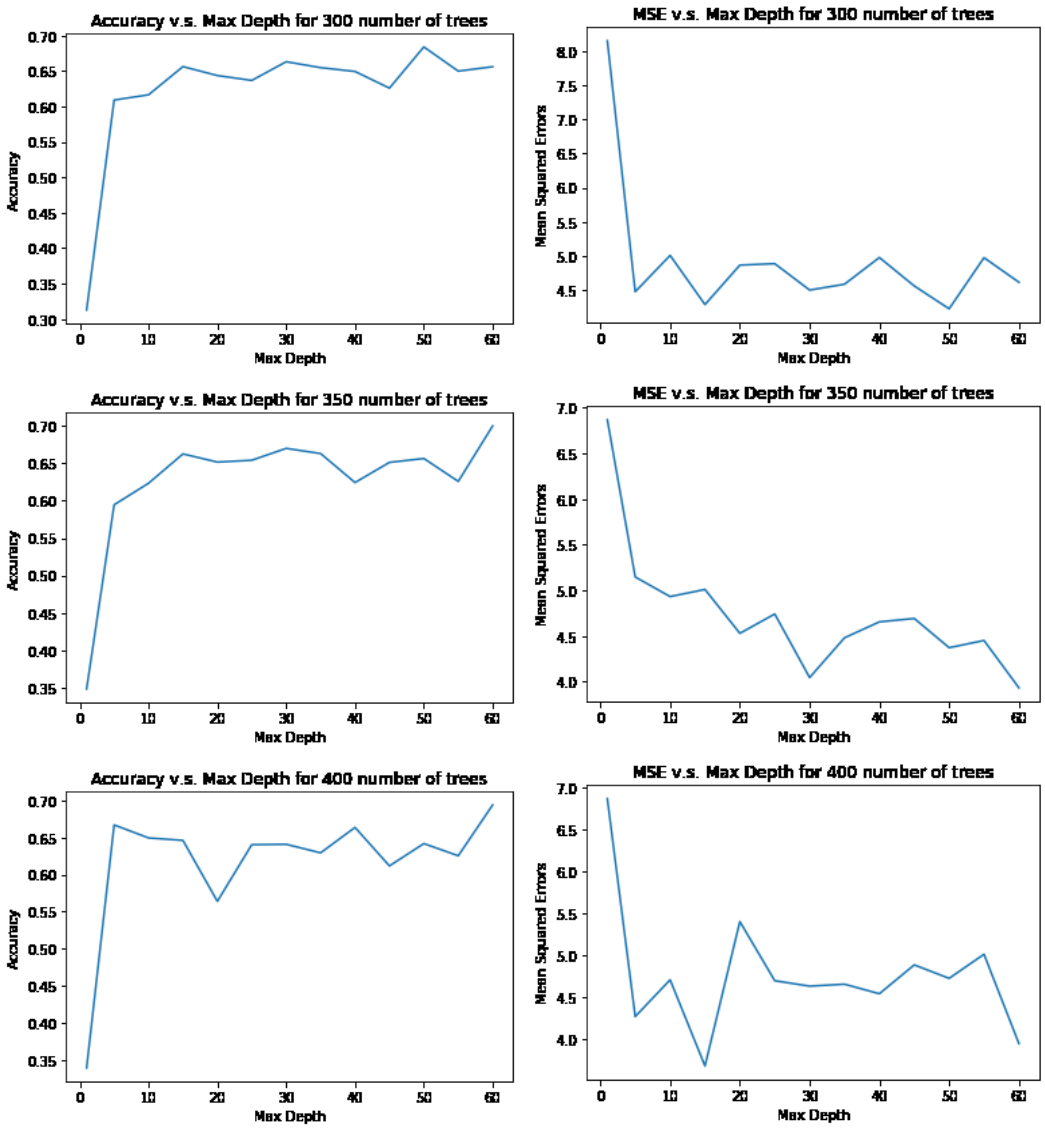

Figure 4-1. Grid search results of baseline random forest model for dataset without feature extractions.

4.2.7.4 Classification

The same random forest classifier was selected for the pre-processed data with the 285 engineered features. After a grid search with 6-fold cross validation, the best result achieved with 150 trees and a maximum depth of 35 for each tree. The grid search results are shown **Figure 4-2**. The best prediction accuracy on the feature dataset is 0.9073, which is 26.8% better than the

prediction results for the dataset without feature selection. This high accuracy also shows the potential for our pressure sensor to be used in voice detection applications, since it can recognize and distinguish small pressures that come from different vocal waveforms.

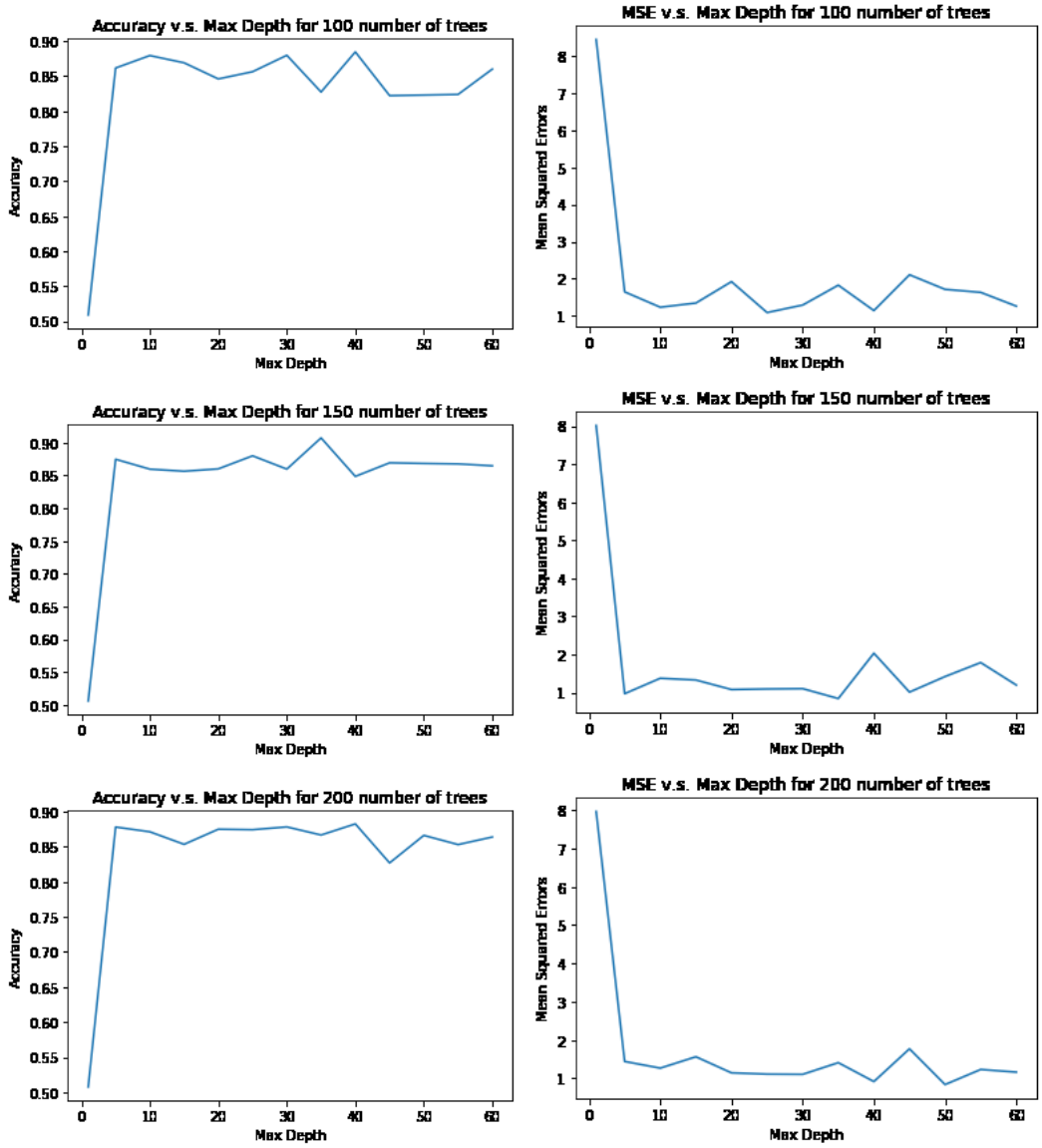

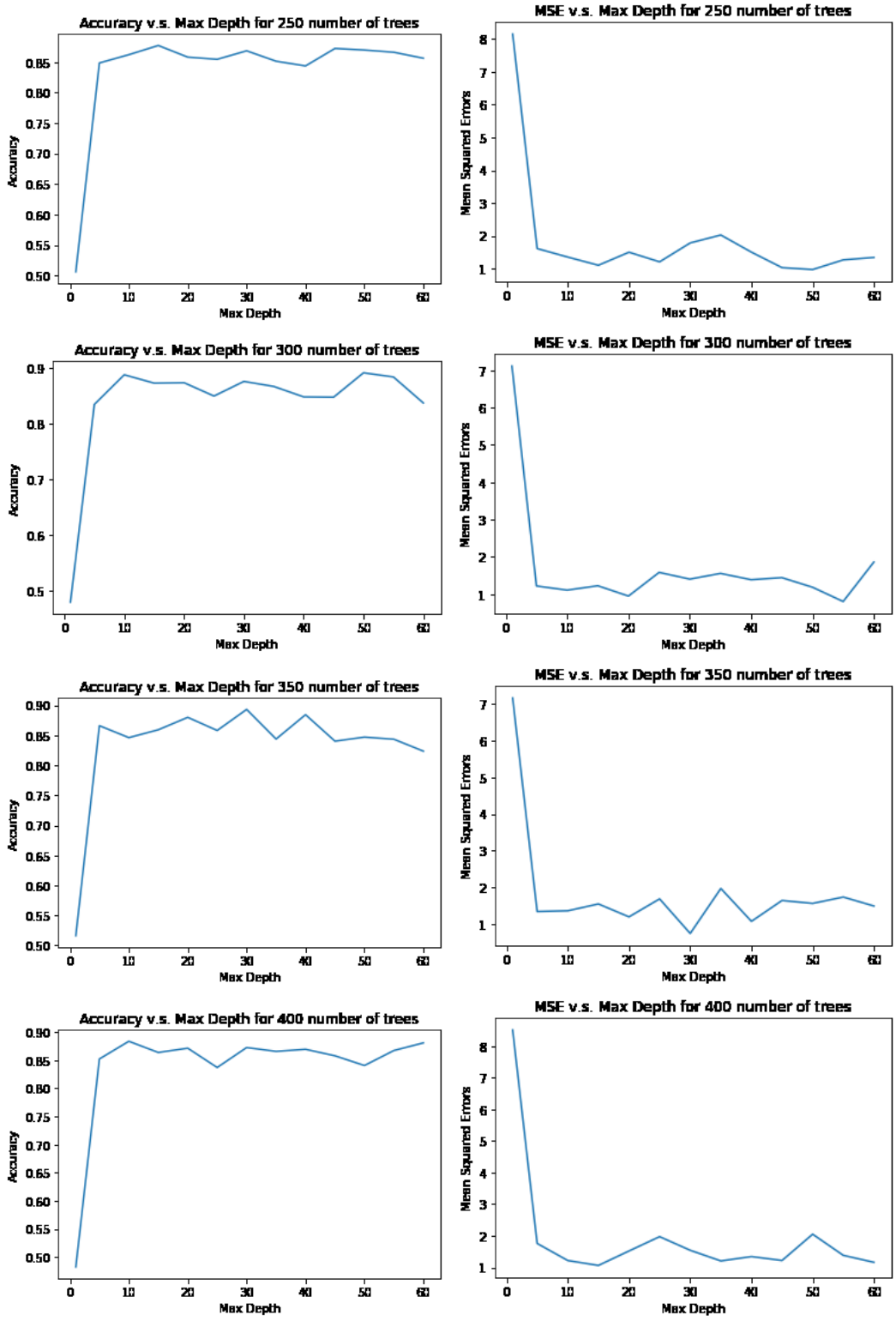

Figure 4-2. Grid search results of random forest model for dataset with feature extractions.

4.3 Results and Discussion

4.3.1 Preparation and Characterization of TOBC/AgNW Conductive Fibers

TOBC and AgNW were chosen as the two building blocks of the conductive fiber due to TOBC being an almost inexhaustible and renewable natural resource and AgNW being highly conductive. When compared to plant cellulose, bacterial cellulose is free of biogenic compounds, like lignin, pectin and hemicellulose, making it a more cost efficient choice.[10] Cellulose also has the advantages of high strength (~10 GPa) and simple fabrication without toxic solvents, which meet the requirements for wearable devices.[11] The inclusion of AgNWs overcomes the resistive nature of TOBC when combined together. **Figure 4-3** depicts TEM images of TOBC nanofibers and AgNWs which have similar width (25-35 nm) and length (15-25 μm). The TOBC/AgNW conductive fibers can be achieved by wet-spinning the homogeneous mixture of TOBC nanofibers and AgNWs. This one-step wet-spinning method overcomes the delamination often experienced by dip coating or growing conductive materials on the surface of the substrate fibers which result in core/shell structures. Strong bonding between TOBC nanofibers and AgNWs eliminates the surface peeling issues that many core/shell conductive fibers have. Also, in comparison with growing contacting metal nanoparticles on the surface, AgNWs need fewer raw materials to accomplish a highly conductive network due to their high aspect ratio. In this work, an optimal AgNW:TOBC ratio of 2:3 was selected where a higher concentration of AgNWs will reduce the strength of the fiber, and a lower concentration of AgNW will impair the fiber's conductivity.

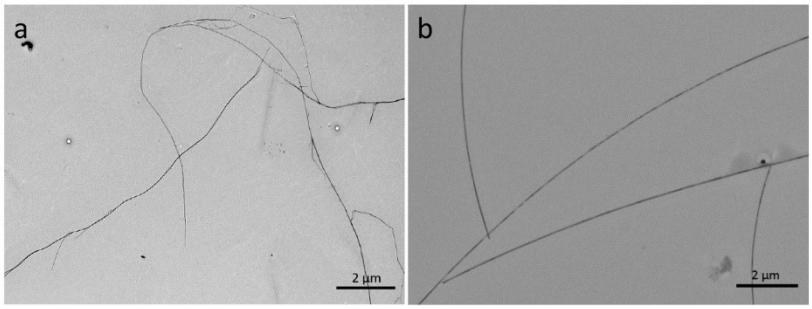

Figure 4-3. TEM images of **(a)** TOBC nanofibers and **(b)** Ag nanowires.

The TOBC/AgNW conductive fibers were fabricated by spinning the TOBC/AgNW dispersion into an acetone coagulation bath from a syringe. More detailed fabrication process can be found in **section 4.2.3** and **4.2.4**. The water inside the extruded fibers exchange with acetone when the fibers are immersed in the coagulation bath. Since acetone is a nonsolvent for TOBC/AgNW dispersion, the extruded fibers become metastable and demixing happens with further exchange of water and acetone.[12] After drying, the spun TOBC/AgNW fibers were further strengthened through multivalent metal cations (Ca^{2+}) crosslinking by immersing the fibers in a 0.1 M calcium dichloride solution for 12 hrs. The interaction between TOBC nanofibers and AgNWs was enhanced by metal-carboxylated/hydroxyl bonds.[10] Both cross-section and surface Energy-dispersive X-ray spectroscopy (EDS) mappings show the uniform spatial distribution of Ag and Ca elements in the conductive fiber, revealing that the AgNWs and Ca^{2+} are well distributed inside the AgNW/TOBC conductive fiber (**Figure 4-4**).

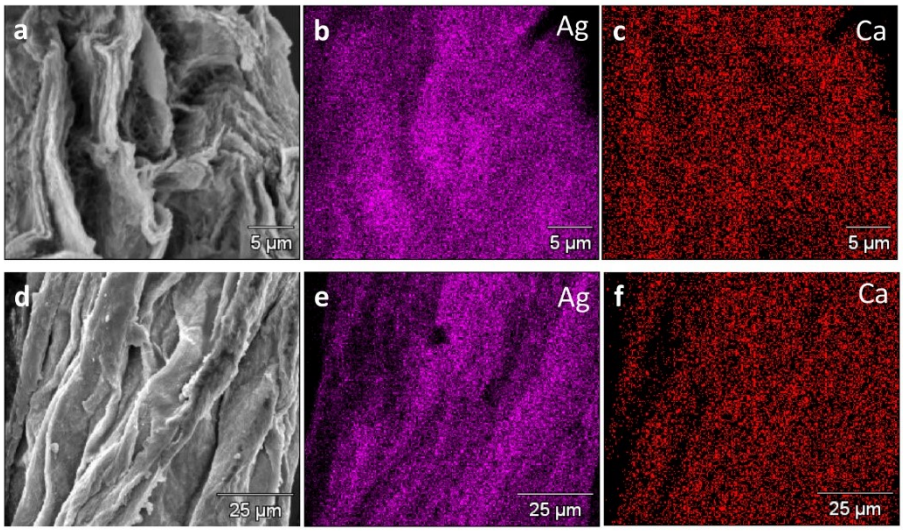

Figure 4-4. Cross-sectional and surficial SEM images and the corresponding EDS mapping images of TOBC/AgNW fiber. (a)(d) Cross-sectional and surficial SEM images. EDS mappings showing the spatial distribution of Ag element on the **(b)** cross-section and **(e)** surface of TOBC/AgNW fiber. Ca element mapping on the **(b)** cross-section and **(e)** surface of TOBC/AgNW fiber.

The final TOBC/AgNW conductive fiber has a hierarchical structure as shown in SEM images (**Figure 4-5**). **Figure 4-5(a)(b)** exhibit the cross-section of TOBC/AgNW fiber, indicating the loose and porous structure shaped during the rapid coagulation in acetone in the process of wet-spinning. **Figure 4-5(c)(d)** demonstrate the surface of the TOBC/AgNW fiber. AgNW and TOBC interlaced together forming conductive lamellar structures thanks to the mutual connection between AgNW and TOBC by hydrogen bonding. **Figure 4-5(d)** indicates the alignment of AgNW and TOBC nanofibers induced by the concentric shear force during extrusion. The diameter of the crosslinked TOBC/AgNW fibers were measured using SEM images. **Figure 4-6** shows a spun fiber with a uniform diameter of 53.15 ± 2.26 μm, which is comparable to the diameters of commercial synthetic fibers (~100 μm). These ultrathin

TOBC/AgNW conductive fibers can be easily woven into or hide inside a piece of cloth as threads without impeding the fashionable requirement for clothes.

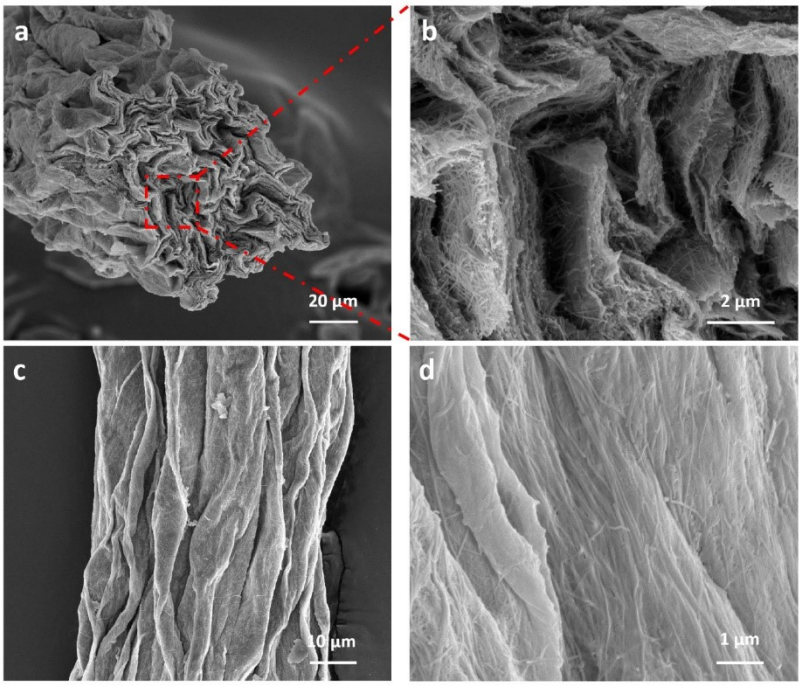

Figure 4-5. SEM images of TOBC/AgNW fiber. (a)(b) Cross-sectional SEM images of TOBC/AgNW fiber. TOBC/AgNW fiber has a loose and porous structure. **(c)(d)** Surficial SEM images of TOBC/AgNW fiber.

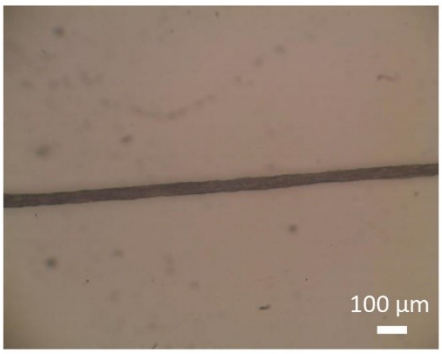

Figure 4-6. Optical microscope image of crosslinked TOBC/AgNW fiber.

To realize a truly wearable device, besides the size of TOBC/AgNW fibers, their strength also rivals the strength of commercial threads. The tensile stress-strain curves were compared for non-crosslinked and crosslinked TOBC/AgNW fibers as shown in **Figure 4-7(a)**. The tensile strength of the non-crosslinked TOBC/AgNW fiber is 148.2 MPa. And after crosslinking, the tensile strength of the fiber increased 33.8% and reached 198.4 MPa. This strength is comparable with Nylon 6, a synthetic fiber whose tensile strength ranges from 50 MPa to 90 MPa. The elongation at fracture of the TOBC/AgNW fiber remained almost the same before and after crosslinking. The good mechanical strength of TOBC/AgNW fibers facilitates their implementations in practical devices. As a promising wearable fiber, the long and flexible cross-linked TOBC/AgNW fibers could be knit into a circle with a diameter of less than 2 mm (**Figure 4-7(c)**) and are able to be threaded into a thin needle and impale cloth with stitch length of 3 mm (**Figure 4-7(b)**).

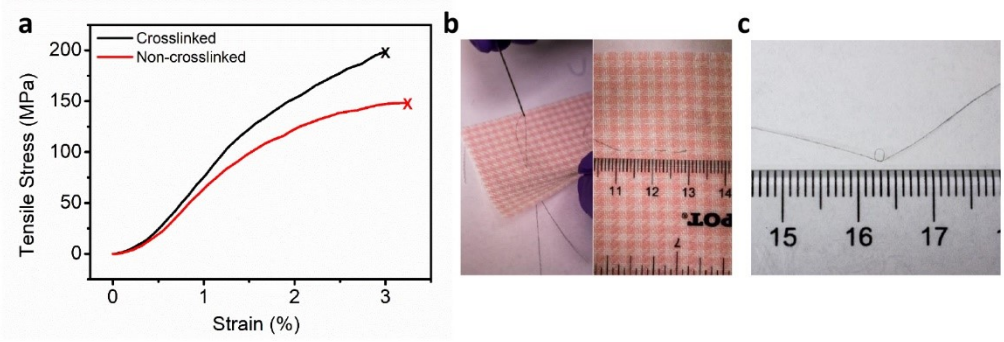

Figure 4-7. Mechanical property of TOBC/AgNW fiber. (a) Tensile stress-strain curves for crosslinked and non-crosslinked fibers. **(b**) A thin needle is threaded by a long flexible TOBC/AgNW fiber and impales cloth. The length of stitches is 3 mm. **(c)** Knitted flexible TOBC/AgNW fiber into a circle with a diameter of less than 2 mm.

Beyond mechanical strength, electrical conductivity of the TOBC/AgNW fiber is another key factor to evaluate the fiber's performance since it determines the sensitivity of the fiber-based capacitive pressure sensor. After crosslinking, the conductivity of the TOBC/AgNW fiber increases from 7.6×10^3 S cm^{-1} to 1.3×10^4 S cm^{-1} which is likely due to AgNWs contact more closely and effectively thanks to Cl^- ions removing the capping agent PVP on the surface of the AgNWs and triggering their coalescence.[13] Moreover, the TOBC/AgNW conductive fibers were tested with a bending-unbending experiment with a curvature radius of 1.5 mm (**Figure 4-8(b)**). Its conductivity remained stable and constant for over 1200 cycles (**Figure 4-8(a)**) and could still light a LED bulb afterwards (**Figure 4-8(c)**).

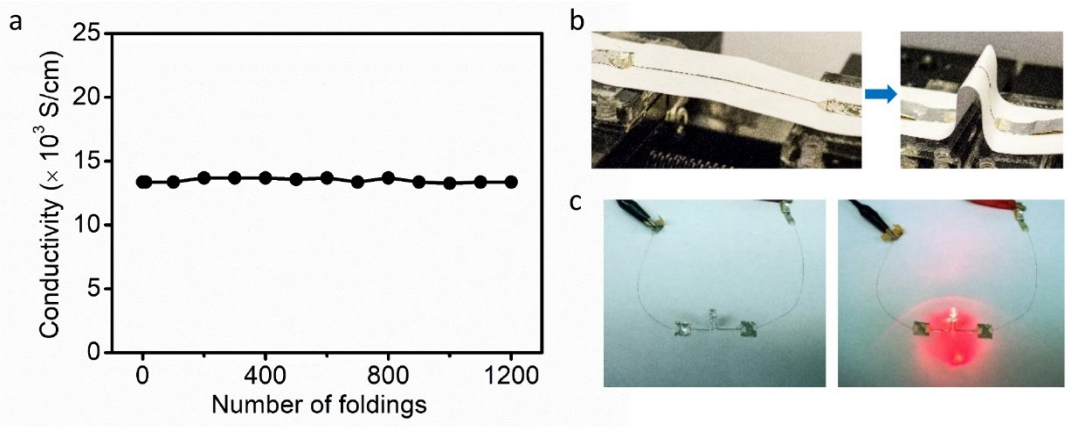

Figure 4-8. Electrical property of TOBC/AgNW fiber. (a) Conductivity change with bending-unbending cycles. **(b)** Setup for bending-unbending experiment. Bending radius is 1.5 mm. **(c)** Two TOBC/AgNW fibers lighting a LED bulb with a voltage of 2 V.

4.3.2 Preparation and Evaluation of TOBC/AgNW/PDMS Fiber-Based Capacitive Pressure Sensor

For capacitive pressure sensors, dielectric layers are indispensable. PDMS was chosen for its high elasticity and low Young's modulus (600 kPa).[14] A thin layer of PDMS was coated on the TOBC/AgNW fiber surface to fabricate the sensor. As shown in **Figure 4-9(a)**, the diameter of TOBC/AgNW/PDMS fiber increased from 53.15 ± 2.26 μm to 63 ± 1.25 μm after the coverage of PDMS. The cross-sectional SEM image shows that only the surface of the fiber was covered by PDMS with little intrusion underneath the surface. The core of TOBC/AgNW/PDMS fiber possesses a similar hierarchical structure with the TOBC/AgNW fiber. The surface SEM image (**Figure 4-9(b)**) demonstrates a smoother surface of TOBC/AgNW/PDMS fiber after the PDMS coating, indicating full coverage of PDMS. Fourier-transform infrared spectrum (**Figure 4-10**) also shows the successful attachment of PDMS and its interaction with the TOBC/AgNW fiber. New absorbing peaks appear in the curve of the obtained TOBC/AgNW/PDMS fiber compared with that of TOBC/AgNW fiber, including peaks of the Si-CH_3 stretching vibration (1262 cm^{-1}) and Si-O stretching vibration (1026 cm^{-1}) deriving from PDMS. The O-H stretching vibration peak shifts from 3416 cm^{-1} to 3430 cm^{-1} for TOBC/AgNW/PDMS fiber due to the interaction between TOBC/AgNW fiber and PDMS.

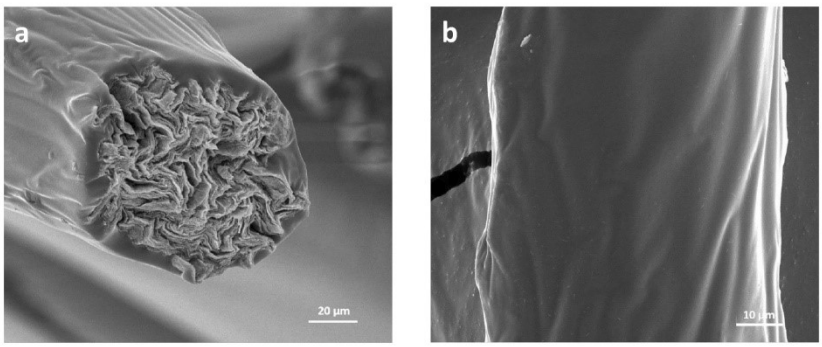

Figure 4-9. SEM images of TOBC/AgNW/PDMS fiber. (a) Cross-sectional image. **(b)** Surficial image. PDMS covers the TOBC/AgNW fiber leading to a smooth surface.

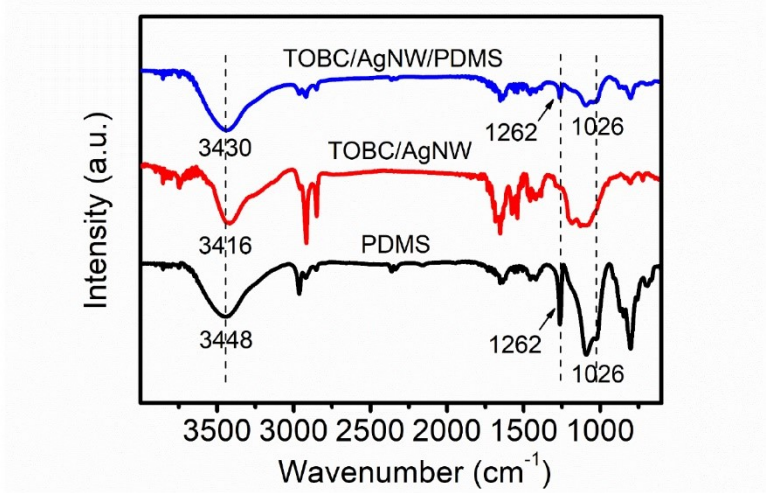

Figure 4-10. FTIR spectrum for pure PDMS, TOBC/AgNW fiber and TOBC/AgNW/PDMS fiber.

The fiber-based pressure sensor was assembled by crossing two TOBC/AgNW/PDMS fibers perpendicularly with each other. Two pieces of aluminum foil were attached at the end of TOBC/AgNW/PDMS fibers with silver paste for electrical contacts. The intersection of the two fibers form one sensing point composed of a plate capacitor with TOBC/AgNW fibers as the electrode plates and surface PDMS layer as the dielectric layer. With applied pressure **(Figure 4-11)**, the thickness of PDMS would decrease leading to the increase of capacitance according to **equation 4-1**:

$$\mathrm{C} = \frac{\varepsilon_0 \varepsilon_r A}{d} \qquad (4-1),$$

where ε_0 is permittivity of air, ε_r is dielectric constant of the dielectric film, A is the area of the electrode and d is the average thickness of the dielectric film.

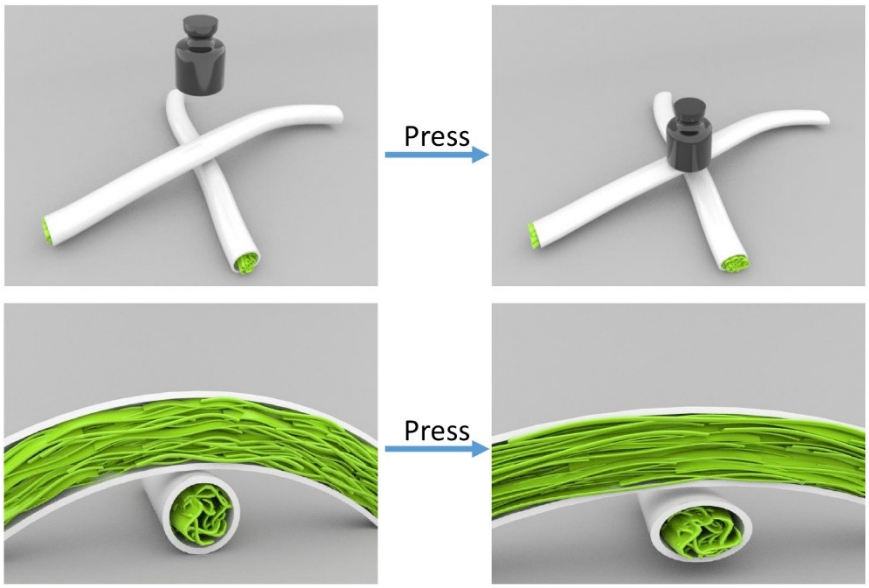

Figure 4-11. Schematic illustration of TOBC/AgNW/PDMS fiber-based sensor and its working mechanism.

To test whether the fiber-based pressure sensor can sense different levels of pressure, three different forces, 0.05 N, 0.1 N and 0.5 N were repeatedly loaded on the sensing point 5 times (**Figure 4-12(a)**). Different capacitance values representing various loads were successfully measured with low noise and good repeatability. The pressure response performance of the sensor was evaluated by pressing the sensor with progressively increasing pressures in the range of 5.4×10^{-3}~134 MPa (**Figure 4-12(b)**). The continuously increasing capacitance curve indicates that the detection limitation of the sensor is beyond 134 MPa. The pressures of the loads are calculated by dividing the forces of the loads with the area of the sensing point. The diameters of the two TOBC/AgNW/PDMS fibers at the sensing point were measured through light microscope images, and then were used to compute the overlapping area of the two fibers. The sensing area of the sensor were calculated to be 3.63×10^{3} μm^2. Due to the ultrathin diameter

of the fibers, only partial weights of the loads were applied to the sensing point since the surface area of the loads are much larger than the area of sensing point. In this work, the entire weights of the loads were used for the convenience of calculation, but the precise sensing range of the sensor might be different. The pressure sensing curve of the pressure sensor at low pressure ranges is enlarged in **Figure 4-12(c)**. The capacitive response shows a linear relationship with the increasing pressures. The sensitivity of the sensor is defined as:

$$S = \frac{\delta(\frac{\Delta C}{C_0})}{\delta P} \qquad (4-2),$$

where C_0 is the baseline capacitance of the sensor without applied pressure, ΔC is the difference between the current capacitance and the baseline capacitance, and P is the applied pressure. Therefore, the sensitivity of the sensor, 101×10^{-4} kPa^{-1}, can be obtained as the slope of the curve in **Figure 4-12(c)**. The pressure response performance of a pressure sensor with a steel fiber as the electrode core was compared with the performance of the TOBC/AgNW/PDMS sensor. The diameter of the steel fiber is 50 μm, which is approximately the same as the diameter of TOBC/AgNW fiber. PDMS was coated on the surface of the steel fiber using the same procedure as for the TOBC/AgNW fiber. As shown in **Figure 4-13**, the sensitivity of the two sensors follow a similar trend, but the capacitive response of the TOBC/AgNW/PDMS sensor in the high-pressure range is nearly double that of the steel/PDMS sensor. This phenomenon can be explained that at the lower pressure range, PDMS deforms first due to its low modulus and high modulus of TOBC. The two sensors possess similar sensitivity owing to the similar PDMS layers' thickness. However, with increased pressure, the air gaps within the hierarchical structures of TOBC/AgNW fibers gradually close, causing the increase in the effective dielectric constant of the dielectric layer. Based on **equation 4-1**, the increasing of the effective dielectric

constant corresponds to a larger capacitance response. This behavior is justified through the solid steel/PDMS sensor having a lower capacitive response with increasing pressures. A negligible hysteresis at different applied pressures (**Figure 4-12(d)**) was also observed for the TOBC/AgNW/PDMS sensor which enables a reversible sensing performance. The response time of the sensor was measured from just before the capacitance increased upon the application of the load and the point in time when the sensor signals stabilized. **Figure 4-12(e)** exhibits the rapid capacitive signal change with an applied pressure. Due to the limitation of the measuring frequency of our readout circuit, the response time of this sensor should actually be shorter than the time between two measuring points. Therefore, the sensor's response time was found to be less than 75 ms. Moreover, repetitive loading–unloading cycling tests were conducted to demonstrate the good durability and stability of the TOBC/AgNW/PDMS sensor. The output signals of the pressure sensor remained stable without any obvious degradation for over 500 cycles (**Figure 4-12(f)**).

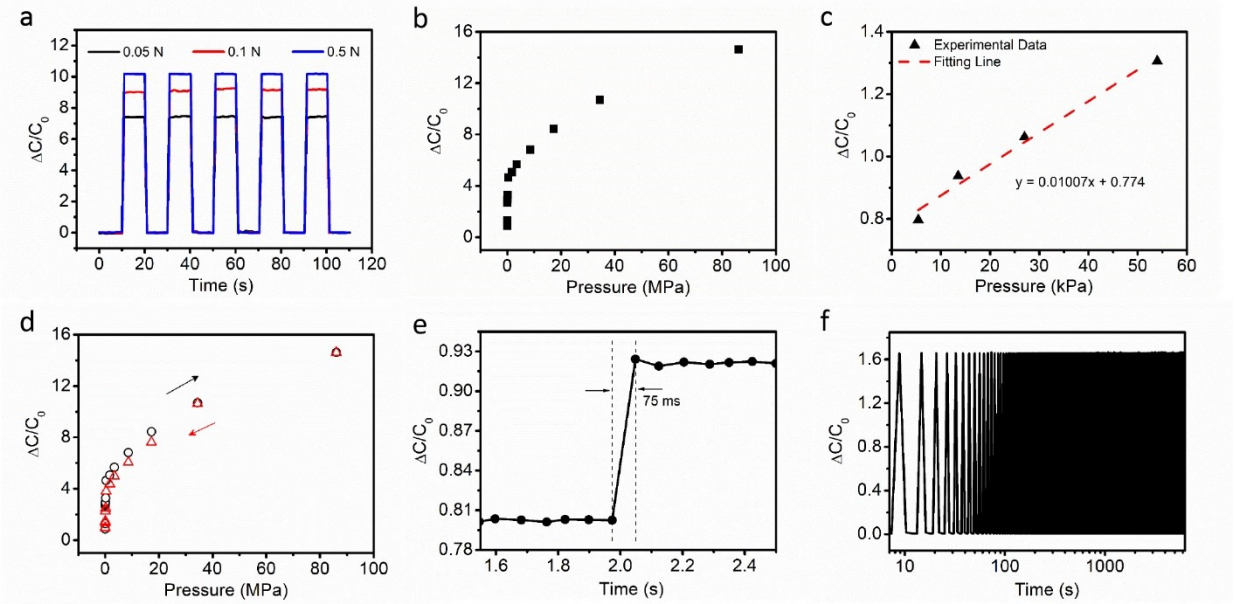

Figure 4-12. Sensing performance of TOBC/AgNW/PDMS sensors. (a) Capacitive response of the pressure sensor in five cycles for the different applied loads of 0.05 N, 0.1 N, and 0.5 N. **(b)** Relative capacitance changes with respect to progressively increasing pressures. **(c)** Relative capacitance changes at low pressure range showing a sensitivity of 101×10^{-1} kPa^{-1}. **(d)** Hysteresis characteristics of the pressure sensor in response to different levels of pressure. **(e)** Response time of the TOBC/AgNW/PDMS sensor. **(f)** Stability of the pressure sensor over 500 cycles of a repeated loading-unloading test.

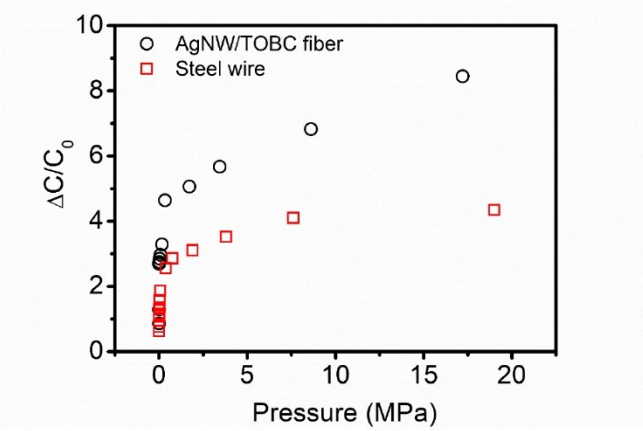

Figure 4-13. Capacitive response performance comparison between TOBC/AgNW/PDMS sensor and Steel/PDMS sensor.

The TOBC/AgNW/PDMS sensors were tested with continuous bending and pressing trials which were designed to evaluate their performance in real-world applications. Under bending, the sensor's capacitive responses were stable for repeated bending cycles (**Figure 4-14(a)**), which exhibit their use in curved configurations. Under direct contact by a finger as shown in **Figure 4-14(b)**, the TOBC/AgNW/PDMS sensor could sense the touch of human fingers at different pressure levels. The ultrathin and flexible TOBC/AgNW/PDMS sensors are

not only simple to fabricate but are also scalable. A 5×5 pixelated sensor array was assembled to detect spatial pressure information with 10 TOBC/AgNW/PDMS fibers (**Figure 4-14(c)**). The total area of the sensor array with 25 pixels is 9 cm^2, and the area of a single pixel is approximately 3.6×10^3 μm^2. Two different weights were placed on the sensor array. The larger weight (5 g) affects two TOBC/AgNW/PDMS sensors due to its large surface area, whereas the smaller weight (2g) was only placed on one single sensing point. Based on the 3D histogram showed in **Figure 4-14(d)**, the pixelated pressure sensor array succeeded in measuring the spatial distribution of external loads. The resolution for this sensing array was limited by the separation between TOBC/AgNW/PDMS fibers. When woven into clothes, the TOBC/AgNW/PDMS fibers can be placed much closer based on the density of the fabric. By replacing the fibers in the cloth, these ultrathin TOBC/AgNW/PDMS fiber-based sensors are capable of reaching a resolution that is under a direct weave.

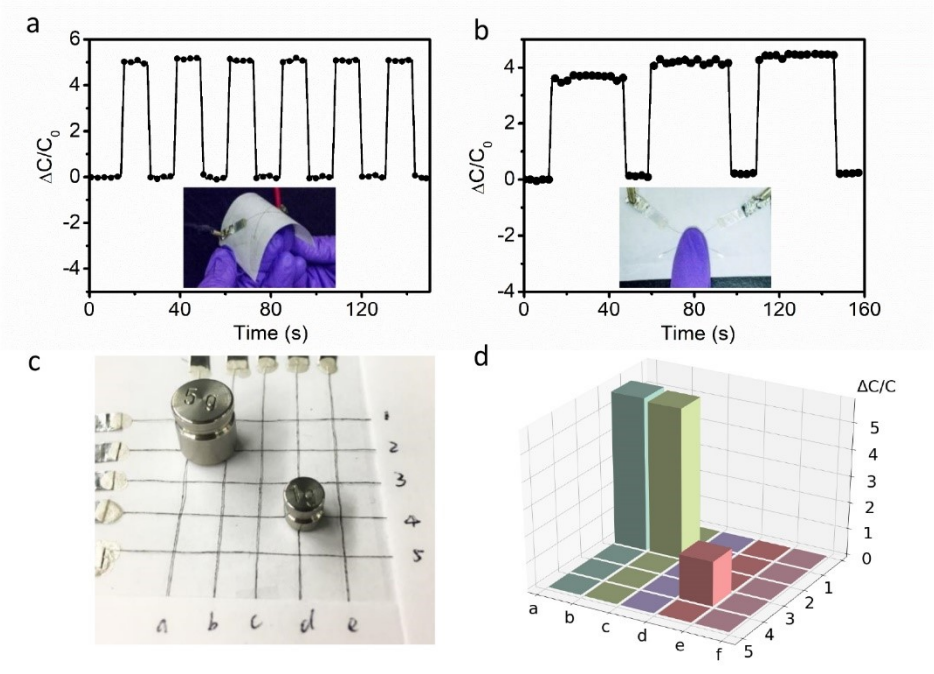

Figure 4-14. Sensing performance of TOBC/AgNW/PDMS sensors. (a) Capacitive response of dynamic bending signals. **(b)** Capacitive response of placing and removal of a human finger. **(c)** Pixelated pressure sensor array to detect the spatial distribution of pressures applied by two different weights. **(d)** 3D histogram of the weights placed on the sensor array.

4.3.3 Applications for Wearable TOBC/AgNW/PDMS Fiber-Based Capacitive Pressure Sensor

To realize the potential of the sensitive TOBC/AgNW/PDMS sensors for wearable devices, the sensors were adhered to a human wrist or throat to detect small physiological signals. A wearable real-time human wrist pulse sensor is demonstrated in **Figure 4-15** where the sensor was attached to a shape memory polymer (SMP) that has a transition temperature around human body temperature. The SMP was rigid and robust at room temperature, but softened rapidly and became elastic once in contact with human skin allowing for good adhesion. As shown in the inset of **Figure 4-15(a)**, the TOBC/AgNW/PDMS sensor was mounted intimately to a human wrist. The real-time wrist pulse signals were clearly detected by our sensor. By enlarging one sensed signal, the typical radial artery pulse waveform was obtained with a distinguishable percussion (P) wave, a tidal wave (T) and a diastolic (D) wave (**Figure 4-15(b)**). The percussion wave is caused by left ventricle ejection, tidal wave is the reflected wave from the small artery and diastolic wave occurs when the blood crash into aortic valve by blood pressure of aorta.[15] The artery pulse waveform can be used to study arterial stiffness, which is a powerful indicator for potential heart failure, renal complications, arteriosclerosis and other health problems. Our TOBC/AgNW/PDMS fiber-based pressure sensor can identify the subtle

variations in artery pulses which demonstrate its potential as a wearable diagnostic device to monitor human health in real-time.

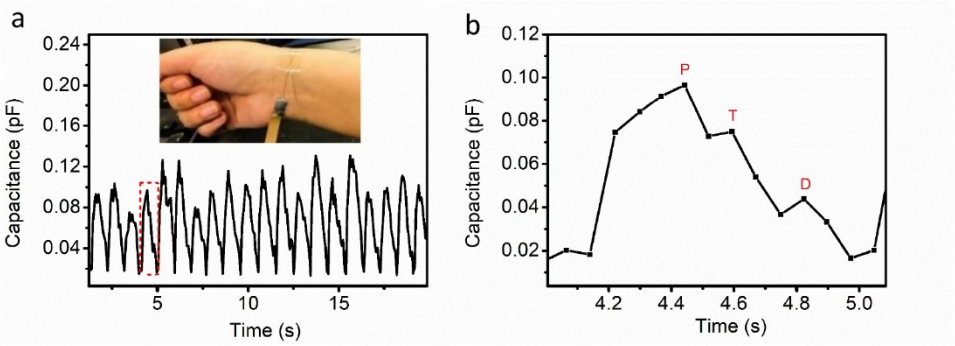

Figure 4-15. Wrist pulse measurements with TOBC/AgNW/PDMS sensor. (a) Capacitive responses of the sensor on a human wrist. **(b)** A typical wrist pulse waveform, indicating percussion (P) wave, tidal (T) wave and diastolic (D) wave.

Besides wrist pulse signal monitoring, accurate speech recognition is another key function for modern smart devices, which is especially important for the people who are hard of hearing or speaking. Modern smart medical devices typically have to not only be practical in application, but also must be attractive to the user. Following suit, we fabricated a fashionable "choker" sensor (**Figure 4-16(a)**) which would lighten the psychological burden for patients who need to wear special assistive equipment. After being mounted on the human throat, our TOBC/AgNW/PDMS fiber-based sensor detected four periodic pronunciations of the word "melody" as shown in **Figure 4-16(b)**. The recitation of a Chinese poem was also recognized by this fiber-based pressure sensor. The six peaks represent the pronunciation of the six words in a line from the poem, respectively (**Figure 4-16(c)**). The mutual transformation between the pronounced words and their digital signals can be very helpful to aid in the communication for

people who have hearing or speaking disabilities. The precise transformation requires high sensing repeatability and accuracy for the sensor to consistently perform well. To demonstrate the excellent phonation detection of our TOBC/AgNW/PDMS fiber-based sensor, the test subject was asked to speak digits 1-10 ten times for each number. The digital signals for each number were collected at a frequency of 10 Hz and then processed. The waveforms for each number display their own traits as shown in **Figure 4-17**. The features for each number's phonation waveform time series were extracted, and then the whole feature dataset was fed into a random forest machine learning model with 6-fold cross validation. The purpose for this machine learning model is to recognize the corresponding number of a vocal waveform based on the feature database. The whole feature dataset was randomly separated into six groups with at least one data entry for each number. For each run of the cross validation, five groups of the feature data were used to train the model, and the remaining group was employed for testing the model's classification accuracy. The prediction accuracy of this random forest classification model was calculated by averaging the accuracy results from the 6-fold cross validation. More detailed data-processing and the grid search procedure can be found in **section 4.2.7**. After finding the optimal prediction model through grid search, the average predicting accuracy for the phonation dataset is 90.73%. This means given an unknown speech waveform of a number that is measured by our TOBC/AgNW/PDMS sensor, this machine learning model can label a number to this waveform with an accuracy of more than 90%. This high accuracy shows the potential for our TOBC/AgNW/PDMS fiber-based pressure sensor to be applied in voice detection devices to help hearing-deficient people connect with the real world.

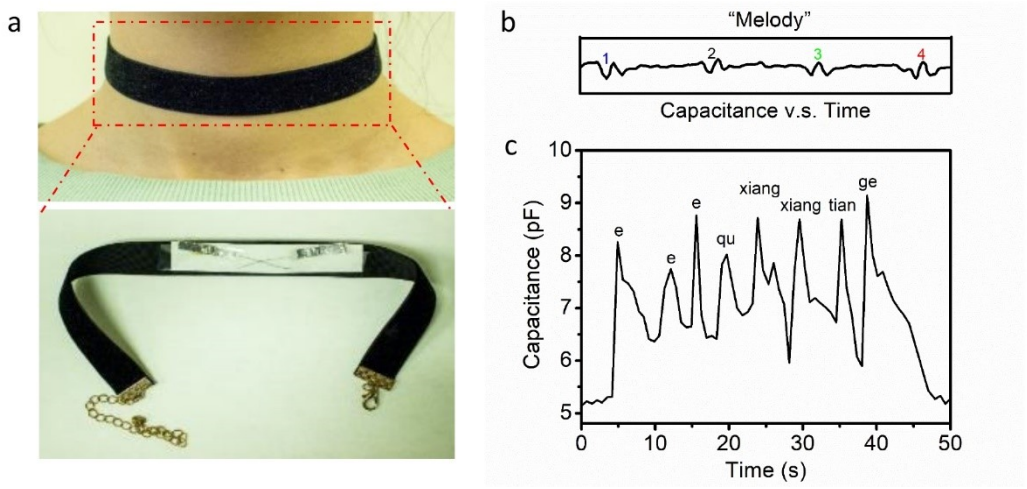

Figure 4-16. Human phonation measurements with TOBC/AgNW/PDMS sensor. (a) The pressure sensor setup on a fashionable choker. **(b)** Capacitance variation of the flexible pressure sensor in response to the pronunciation of "melody". **(c)** Capacitance variation in response to the pronunciation of a line of a Chinese poem.

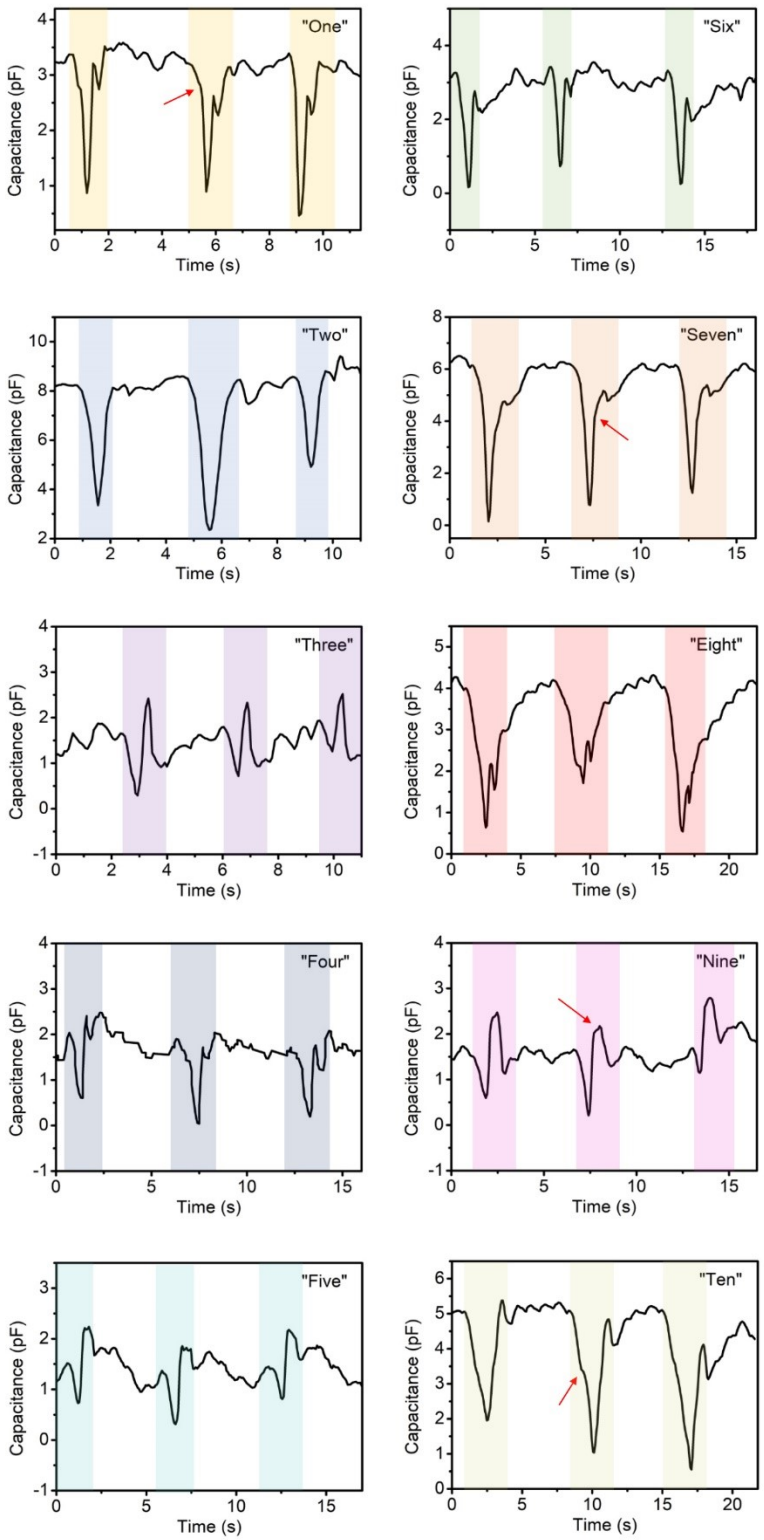

Figure 4-17. Voice detection of digit 1-10 with the TOBC/AgNW/PDMS sensor.

4.4 Conclusion

In summary, we have developed a sensitive TOBC/AgNW/PDMS fiber-based wearable capacitive sensor through a simple and efficient approach. The conductive TOBC/AgNW fiber was fabricated by wet-spinning AgNWs with TOBC nanofibers. After being coated with a dielectric layer of PDMS, two resultant ultrathin, flexible and robust TOBC/AgNW/PDMS fibers can be stacked perpendicularly with each other to obtain a fiber-based capacitive pressure sensor. The TOBC/AgNW/PDMS fiber-based sensor can detect human contact, such as finger pressing, and is sensitive to weak pressures like wrist pulses and vocal vibrations due to the unique hierarchical structure of TOBC/AgNW fibers. Based on a machine learning model, the classification accuracy for the speech waveforms of numbers 1-10 that are detected by our TOBC/AgNW/PDMS pressure sensors reached > 90%. Therefore, this TOBC/AgNW/PDMS fiber-based pressure sensor holds great potential in wearable medical attachments. In addition to their potential in the medical field, their ultrathin diameter is promising to achieve high sensing resolution when sewn into clothing or replacing the thread in fabric, which could meet both function and fashion requirements for modern smart devices.

4.5 Reference

[1] J. An, T.-S. D. Le, Y. Huang, Z. Zhan, Y. Li, L. Zheng, W. Huang, G. Sun, Y.-J. Kim, *ACS applied materials & interfaces* **2017**, 9, 44593.

[2] W. A. D. M. Jayathilaka, K. Qi, Y. Qin, A. Chinnappan, W. Serrano-García, C. Baskar, H. Wang, J. He, S. Cui, S. W. Thomas, *Advanced Materials* **2019**, 31, 1805921.

[3] J. Lee, H. Kwon, J. Seo, S. Shin, J. H. Koo, C. Pang, S. Son, J. H. Kim, Y. H. Jang, D. E. Kim, *Advanced materials* **2015**, 27, 2433.

[4] O. Atalay, A. Atalay, J. Gafford, C. Walsh, *Advanced Materials Technologies* **2018**, 3, 1700237.

[5] J. J. Park, W. J. Hyun, S. C. Mun, Y. T. Park, O. O. Park, *ACS applied materials & interfaces* **2015**, 7, 6317.

[6] a) S. Han, M. K. Kim, B. Wang, D. S. Wie, S. Wang, C. H. Lee, *Advanced Materials* **2016**, 28, 10257; b) B. Zhu, H. Wang, Y. Liu, D. Qi, Z. Liu, H. Wang, J. Yu, M. Sherburne, Z. Wang, X. Chen, *Advanced Materials* **2016**, 28, 1559; c) J. Park, Y. Lee, J. Hong, Y. Lee, M. Ha, Y. Jung, H. Lim, S. Y. Kim, H. Ko, *ACS nano* **2014**, 8, 12020.

[7] D. Kwon, T.-I. Lee, J. Shim, S. Ryu, M. S. Kim, S. Kim, T.-S. Kim, I. Park, *ACS applied materials & interfaces* **2016**, 8, 16922.

[8] X. Shuai, P. Zhu, W. Zeng, Y. Hu, X. Liang, Y. Zhang, R. Sun, C.-p. Wong, *ACS applied materials & interfaces* **2017**, 9, 26314.

[9] Z. He, W. Chen, B. Liang, C. Liu, L. Yang, D. Lu, Z. Mo, H. Zhu, Z. Tang, X. Gui, *ACS applied materials & interfaces* **2018**, 10, 12816.

[10] J. Yao, S. Chen, Y. Chen, B. Wang, Q. Pei, H. Wang, *ACS applied materials & interfaces* **2017**, 9, 20330.

[11] M. Iguchi, S. Yamanaka, A. Budhiono, *Journal of materials science* **2000**, 35, 261.

[12] A. Figoli, T. Marino, F. Galiano, in *Membrane Technologies for Biorefining*, DOI: https://doi.org/10.1016/B978-0-08-100451-7.00002-5 (Eds: A. Figoli, A. Cassano, A. Basile), Woodhead Publishing **2016**, p. 29.

[13] Y. Jin, L. Li, Y. Cheng, L. Kong, Q. Pei, F. Xiao, *Advanced Functional Materials* **2015**, 25, 1581.

[14] Z. Lou, L. Li, L. Wang, G. Shen, *Small* **2017**, 13, 1701791.

[15] S. Rajagopal, *The Art and Science of Cardiac Physical Examination*, JP Medical Ltd, **2015**.

Chapter 5

Conclusion and Future Work

This dissertation investigates dielectric, electroactive and phase transition properties of bistable electroactive polymer. Each aspect of BSEP was examined and adapted for innovative devices fabrication, including rewritable photonic paper, smart windows with whole solar spectrum modulation and wearable pressure sensors.

Rewritable paper with an environmentally conscious manufacturing process, an uncomplicated erasing method, and a long reusability lifetime has attracted wide interest among researchers in recent years. However, reported paper substitutes are either unable to store data for an extended amount of time or reliant on liquid-based writing/erasing processes that degrade the paper over time. By combining the shape memory and electroactive properties of BSEP with photonic crystal, here we report an ink-free rewritable nanocomposite that may pave the way for a true paper replacement. The rewritable nanocomposite is comprised of a ferroferric oxide-carbon core-shell (Fe3O4@C) nanoparticle (NP) based photonic crystal embedded in a bistable electroactive polymer (BSEP). This nanocomposite switches colors in an all-dry process, where electric fields and heat are used to write and erase the colors respectively. Electrical actuation

induces large deformation in the z-axis of the nanocomposite, creating distinct color contract in the actuated area. The shape memory property of the polymer allows it to store images for more than a year, and those images can be written free-form, without the need for stamps. The nanocomposite can sustain more than 500 cycles of writing and erasing, and high-resolution images are possible. But right now, the color switching on a single photonic paper is limited to a small bandwidth around 130 nm. For future improvement, larger z-directional deformation of BSEP/photonic crystal composite should be achieved to accommodate full color switching of the photonic paper. For the configuration of the photonic paper designed in this dissertation, opal structure was utilized for the arrangement of photonic crystals. By tuning the lattice constant of photonic crystals, the reflected color of the photonic paper varies too. The issue for the current design is when deforming the z-direction of the photonic paper to a certain extent, Fe_3O_4@C NPs will press against each other and stop further tuning of the reflected color. To resolve this problem, inverse opal structure of photonic crystals should be introduced since the porous structure leaves more room in the photonic paper for deformation.

When only focusing on the phase transition property of BSEP, its reversible amorphous-to-semicrystalline transition is intriguing for ingenious application. BSEP can switch between transparent and opaque states when heated above or below its melting temperature due to the crystallization. In this dissertation, this opacity switch function was carried into a smart window application for temperature modulation and privacy protection purposes. The formula of BSEP was edited to import micro-scale phase separation, which is beneficial for the whole solar spectrum modulation due to Mie scattering. The micro-scale phase separation is because of the large hydrophobicity difference of the two constituent polymers in BSEP. Acetone was used as a co-solvent for the two components to confine the phase separation into desired sizes. The

resulted smart window has a large solar transmittance modulation of 70.2% and excellent luminous transmittance modulation of 80.4%. At transparent state, the luminous transmittance of this smart window can be as high as 95.3%; whereas at opaque state, the luminous transmittance drops to only 14.9%, which rivals the highest privacy level for commercial privacy glasses. Even though this smart window has promising solar and visible light modulation, one downside is it requires external joule heating to keep the smart window staying at transparent state. A passive opaque state of the smart window is preferable to preserve the cold or warm air within building rooms during summer or winter. But a passive transparent state is also desirable for energy conservation aspect. The required heater working power density for keeping the smart window at transparent state is less than 0.1 W cm^{-2} for the current heating design. To reduce the power consumption, a new design of the heating element or fabricating a bistable phase transition film are needed.

As for the dielectric properties that come from the insulating nature of polymers, a fibrous pressure sensor was demonstrated based on this facet. TOBC/AgNW fibers were used as the conducting layer, the outside PDMS shell serves as insulating layer. Thanks to the hierarchical structure, ultrathin diameter and high conductivity of TOBC/AgNW fibers, the TOBC/AgNW/PDMS sensor has good sensitivity (101×10^{-4} kPa^{-1}), resolution and wide working range (from human pulse pressure to > 134 MPa), which can be applied as human pulse or voice detector. With a trained random forest classification model, the voice detector based on this fibrous sensor can recognize human's voice waveform for digit 1-10 with a test accuracy of 90%. The diameter of the ultrathin and flexible TOBC/AgNW/PDMS fibers (53 μm) is comparable with commercial sewing thread, making it promise for wearable devices that meet both comfort and fashion requirements. One improvement that can be made for future

implementation is to increase the strength of TOBC/AgNW/PDMS fibers to sustain machine washing and normal wear. PDMS can also be replaced with a BSEP that has a transition temperature near human's body temperature. This way sensor will only be activated when attached to human body and ignore the noise signals for invalid usage.